

TESI DI DOTTORATO

UNIVERSITÀ DEGLI STUDI DI NAPOLI “FEDERICO II”

DIPARTIMENTO DI INGEGNERIA ELETTRONICA  
E DELLE TELECOMUNICAZIONI

DOTTORATO DI RICERCA IN  
INGEGNERIA ELETTRONICA E DELLE TELECOMUNICAZIONI

---

**ADAPTIVE RADAR DETECTION  
IN PRESENCE OF MISMATCHES**

---

**LUCIANO LANDI**

Il Coordinatore del Corso di Dottorato

Ch.mo Prof. Giovanni POGGI

I Tutori

Ch.mo Prof. Ernesto CONTE

Ch.mo Prof. Antonio DE MAIO

A. A. 2006–2007



# Contents

<b>Acknowledgments</b>	<b>iii</b>
<b>List of Figures</b>	<b>v</b>
<b>List of Tables</b>	<b>ix</b>
<b>Introduction</b>	<b>xi</b>
<b>1 Adaptive Radar Detection</b>	<b>1</b>
1.1 System model . . . . .	3
1.1.1 Target model . . . . .	7
1.1.2 Interference Sources . . . . .	13
1.1.3 Space Time Adaptive Processing . . . . .	19
1.2 Conventional Receivers . . . . .	26
1.2.1 Generalized Likelihood Ratio Test . . . . .	29
1.2.2 Adaptive Matched Filter . . . . .	32
<b>2 Bistatic Radars</b>	<b>35</b>
2.1 Bistatic radar range equation . . . . .	39
2.2 Ovals of Cassini . . . . .	41
2.3 Bistatic plane and range cells . . . . .	44
2.4 Target location . . . . .	47
2.5 STAP for bistatic radars . . . . .	50
<b>3 Detection with Uniform Linear Arrays</b>	<b>55</b>
3.1 Mutual coupling and near-field effects . . . . .	58
3.1.1 Modelling Near Field Effects . . . . .	58
3.1.2 Modelling Mutual Coupling . . . . .	60
3.1.3 Problem Formulation and Design Issues . . . . .	62

---

3.1.4	Performance Analysis . . . . .	69
3.2	Partially-Homogeneous Environment . . . . .	72
3.2.1	Problem Formulation and Design issues . . . . .	74
3.2.2	Performance Analysis . . . . .	78
<b>4</b>	<b>Distributed Aperture Radars</b>	<b>81</b>
4.1	System Model . . . . .	83
4.1.1	Signal model . . . . .	85
4.1.2	Interference model . . . . .	88
4.1.3	STAP implementation . . . . .	90
4.2	Clutter non-stationarity . . . . .	91
4.2.1	JDL algorithm for distributed aperture radars . . . . .	93
4.3	CFAR behavior . . . . .	98
4.4	Numerical simulations . . . . .	100
4.4.1	Need for waveform diversity . . . . .	101
4.4.2	Need for JDL algorithm . . . . .	102
	<b>Conclusions</b>	<b>107</b>
	<b>Bibliography</b>	<b>111</b>

# List of Figures

1	Different types of radar. . . . .	xii
2	The Over-The-Horizon radar. It exploits the ionosphere reflection to increase the radar horizon. . . . .	xiii
3	The multistatic radar. It is composed by one transmitter and two or more receivers in different sites. . . . .	xiii
1.1	Linear array configuration. The antenna elements, denoted by the black circles, are displaced along one line. . . . .	2
1.2	Planar array configuration. The antenna elements, denoted by the black circles, are displaced upon a plane. . . . .	3
1.3	Spatial array configuration. The antenna elements, denoted by the black circles, are displaced along three dimensions. . . . .	4
1.4	Pulses burst with some features emphasized. . . . .	4
1.5	Processing for each array element channel. . . . .	5
1.6	The radar CPI datacube. . . . .	6
1.7	Radar-cross-section polar plot. . . . .	8
1.8	Radar geometry: the vector $\mathbf{r}_n$ locates the $n^{th}$ element of the array and $\hat{\mathbf{k}}(\varphi_t, \theta_t)$ is the wave propagation unit vector from the target. . . . .	10
1.9	A ring of ground clutter for a fixed range. . . . .	18
1.10	A general block diagram for a space-time processor. T denotes the time repetition interval. . . . .	21
1.11	Data-domain view of space-time adaptive processing. . . . .	22
1.12	Fully adaptive space-time processor. . . . .	27
2.1	Bistatic radar North-referenced coordinate system in two dimensions. . . . .	36
2.2	Concentric isorange contours: transmitter and receiver are the common foci of the ellipses. . . . .	38

2.3	Geometry for converting North-referenced coordinates into polar coordinates $(r_p, \theta_p)$ . . . . .	42
2.4	Contours of a constant SNR - ovals of Cassini, with $K = 30L^2$ . . . . .	42
2.5	Maximum and minimum bistatic range cells. . . . .	45
2.6	Geometry for bistatic range cell separation. . . . .	46
2.7	Timing diagram for direct (DM) and indirect (IM) method of calculating range sum $R_T + R_R$ . . . . .	48
3.1	Uniform linear array with $N = 5$ elements. $d$ is the interelement spacing; $n = 0$ characterizes the reference. . . . .	56
3.2	Spherical wave-front model with the source signal arriving broadside to the array. $d$ is the interelement spacing and $\Delta(n)$ is the path delay across the array at element position $n$ ; $\theta$ is the direction of arrival measured from the array broadside; $R$ is the curvature radius of the wave-front. . . . .	59
3.3	Antenna array as a linear bilateral $N + 1$ port network . . . . .	61
3.4	Block diagram of the NF-MC-1S-GLRT . . . . .	66
3.5	$P_D$ versus SINR for $P_{FA} = 10^{-4}$ , $N = 84$ , $K = 170$ , $P = 15$ , and $\bar{R} = 700$ m. . . . .	71
3.6	$P_D$ versus SINR for $P_{FA} = 10^{-4}$ , $N = 84$ , $K = 170$ , $P = 15$ , and $\bar{R} = 1100$ m. . . . .	72
3.7	$P_D$ versus SINR for $P_{FA} = 10^{-4}$ , $N = 84$ , $K = 170$ , $P = 15$ , and $\bar{R} = 4000$ m. . . . .	73
4.1	Time orthogonal signals with different pulse duration and common PRI. . . . .	84
4.2	Total trip delays involving the target (solid line) and the artifact (dashed line). . . . .	89
4.3	Geometry of bistatic ground radar. . . . .	93
4.4	Bistatic plane with bistatic ellipse. . . . .	94
4.5	Clutter Doppler frequency plotted for different range cells. It is evident the non-stationarity of this feature of the clutter. . . . .	94
4.6	Localized processing region in angle-Doppler domain for $\eta_h = \eta_d = 3$ . . . . .	96
4.7	Block diagram of the JDL transformation for the $r^{th}$ transmission. Only the primary data are considered. . . . .	99
4.8	Matched filter processing along the radial Z-direction. Includes interference. . . . .	102

---

4.9	Matched filter processing along the transverse X-direction. Includes interference. . . . .	103
4.10	MSMI statistic along the radial Z-direction. Includes interference. . . . .	104
4.11	MSMI statistic along the transverse X-direction. Includes interference. . . . .	105
4.12	Probability of detection versus the SNR. The solid line represents the F-MSMI; the star-marked the W-MSMI; the dashed one the JW-MSMI. . . . .	105



# List of Tables

2.1	Parameters in the bistatic radar range equation. . . . .	39
3.1	Detection rules and corresponding acronyms. . . . .	70
4.1	Common parameters for the simulations. . . . .	101



# Introduction

The problem of detecting a radar signal, known up to a scaling factor, in the presence of disturbance with unknown spectral properties, has gained more and more attention during the last two decades, and, over the years, several solutions have been proposed. The detection is often performed in overland or littoral environment where the ground clutter can be quite severe and in the presence of hostile electronic countermeasures, or jamming. The radar needs to possess the capability to suppress both clutter and jamming to near or below the noise level. In this way the sensitivity of the radar is fully used in signal environments containing unwanted interference. The detection is based on the analysis of the echo of some transmitted signals. Fig. 1 shows the possible configurations of a radar system [1, 2, 3]. A *monostatic radar* refers to a radar system which has the transmitter and the receiver located at the same site. It has been the most widely used radar since it was developed in the late 1930s, primarily because it is easier to operate and usually - but not always - performs better than bistatic radar [4]. Airborne early warning (AEW) radar is an example of an airborne monostatic radar. Although monostatic means stationary, in airborne radar engineering it is used to address an individual radar system. The *bistatic radar* is a radar operating with separated transmitting and receiving antennas. This configuration presents some advantages respect to the monostatic one. First of all, the airborne bistatic radar, based on two airborne antennas, one used as transmitter and the other as receiver, allows the exploration of a enemy zone in “safe” mode; in fact, the receiving antenna, that operates in passive mode, doesn’t send any electromagnetic signal and thus it is not detectable. Being in passive mode, the receiving antenna is also more immune to the jammers [5]. Another advantage, evident for the Over-The-Horizon (OTH) radar, is the improvement of the radar horizon. The electromagnetic wave tends to travel in straight line. This limits the radar horizon due to the Earth curvature. Using separated sites for transmitter and receiver and exploiting the ionosphere reflection, it follows that the radar

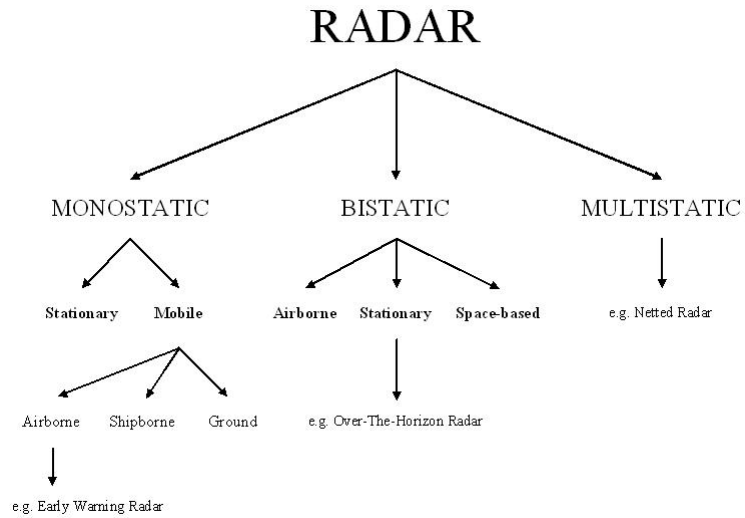


**Figure 1:** Different types of radar.

horizon is bigger than that of a monostatic radar, as depicted in Fig. 2. When two or more receiving sites with common (or overlapping) spatial coverage are employed and data from targets in the common coverage area are combined at a central location, the system is called *multistatic radar*, as shown in Fig. 3. Multistatic radars can provide improved performance against stealth targets, protection against attack through the use of stand-off transmitters and improved performance against electronic countermeasures [6]. A multistatic radar is a special case of *radar net*; both process target data from multiple sites at a central location. A radar net typically consists of a set of monostatic radars, with target data processed noncoherently at the central location. The net can be configured in two different ways, depending on site separation. When the sites are widely spaced, the net can join the target data from each site so that an extended target track is established over the coverage of the net, thereby expanding the spatial coverage. This coverage is the union of each site's coverage area. When the sites are closely spaced, the net can combine target data from sites having common spatial coverage to improve the quality of target state estimates. Obviously, the common coverage area increases as the site separations decrease. A multistatic radar is also configured to combine target data within the common coverage area to improve the quality of target state estimates. If the multistatic radar combines the data coherently, quality

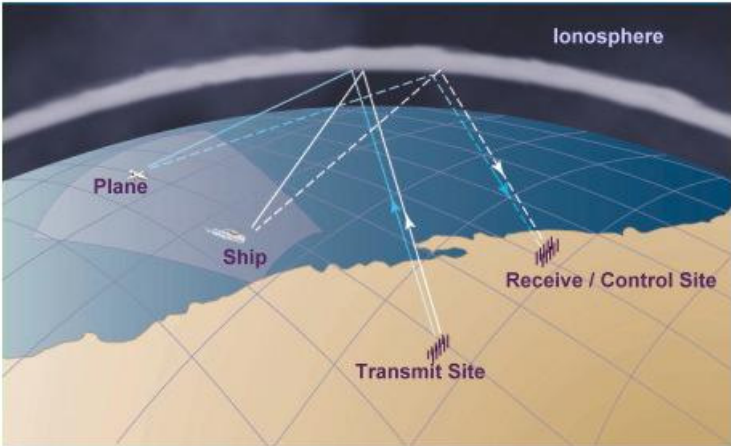


**Figure 2:** The Over-The-Horizon radar. It exploits the ionosphere reflection to increase the radar horizon.



**Figure 3:** The multistatic radar. It is composed by one transmitter and two or more receivers in different sites.

can be further improved [4]. There are also some other configurations, like *hybrid radars* and *pseudomonostatic radars*; the treatment of them lies outside the aims of this work and we refer the interested reader to the literature.

The suppression of the interference is an important issue in radar design. It is well known that the use of adaptive techniques can ensure a good rejection to the jamming and clutter. During the last 40 years, the research on the adaptive beamforming has been grown up, driving to good performances in the target detection. A very powerful instrument is based on the Space-Time Adaptive Processing (STAP), which is based on the *simultaneous* processing of signals received on multiple antennas (space domain) and from multiple pulse repetition periods (time domain) of a coherent processing interval (CPI). STAP offers the potential to improve radar performance in several areas. First, it can improve low-velocity target detection through better mainlobe clutter suppression. Second, STAP can permit detection of small targets that might otherwise be obscured by sidelobe clutter. Third, STAP provides detection in combined clutter and jamming environments. Finally, STAP adds robustness to system errors and a capability to handle non-stationarity interference [7].

Many solutions assume the existence of training (secondary) data, namely returns free of useful signal and which share the same covariance matrix of the data under test (primary data), in order to form an estimate of the disturbance covariance matrix. Furthermore, these approaches consider the environment ideal in some sense. For example, the target and the interference sources are considered in the far-field of the antenna array. In particular, starting from the lack of a Uniformly Most Powerful (UMP) test for the quoted problem, in [8], the author devises and assesses the Generalized Likelihood Ratio Test (GLRT) which interestingly ensures the Constant False Alarm Rate (CFAR) property with respect to the disturbance covariance matrix. However, for the case at hand, the GLRT detector is not a UMP-Invariant one and, actually, a UMP-Invariant test does not exist as shown in [9, 10]. It has been thus reasonable to investigate different detection strategies which may ensure better performance than the GLRT or reduce its computational complexity. To this end, in [11], another receiver, the Adaptive Matched Filter (AMF) is proposed and assessed resorting to a two-step GLRT design procedure: first derive the GLRT for the case that the covariance matrix of the primary data is known. Then, the sample covariance matrix, based upon secondary data, is substituted, in place of the true covariance matrix, into the test. The resulting receiver, which still ensures the CFAR property with respect to the disturbance spectral properties, is less time-consuming and may even achieve better detection performance

than Kelly's GLRT.

The principal aim of this work is the analysis of some conditions of mismatch from the ideality. In particular, we focus on four different effects:

1. mutual coupling,
2. near-field condition,
3. limitation in the size of the sample support,
4. non-stationarity,

that are present in many practical situations. First, the mutual coupling is an inherent characteristic of the antenna arrays. In fact, part of the incident field is reflected and so re-irradiated from each antenna element, which couples to its neighbors, as do currents that propagate along the surface of the array. As a consequence, mutual coupling arises, namely the primary voltage of each array element is the sum of the voltage due to the incident radiation plus all the contributions from the various coupling sources from each of its neighbors. Second, the wave-front arriving at the array cannot always be assumed planar. In fact specular reflections from the aircraft body are near-field sources which originate non-planar wave-front impinging on the array. Additionally the distance of the cell under test from the radar might not be significantly greater than the far-field distance. Third, the STAP needs a high number of secondary data for the processing, but in some practical cases collecting the required sample support is not possible. A way to circumvent this limitation relies on the exploitation of the inherent characteristics of the covariance matrix. Finally, when the detection is based on bistatic or multistatic radars, the environment is not stationary due to the relative motion between antenna elements and interference sources; resorting to techniques able to counteract the non-stationarity of the environment is very useful. The detection is analyzed using two different types of antenna arrays:

1. uniform linear arrays,
2. distributed aperture arrays,

which strongly differentiate on the dimension of the array. The *uniform linear arrays* (ULA) are composed by antenna placed on one spatial dimension with the same distance between each element. The antennas of a *distributed aperture arrays* are placed thousands of wavelengths apart from each other. The mismatching conditions reported above are taken in account for the quoted

arrays. In particular, the uniform linear arrays are strongly affected by the mutual coupling and there are some practical cases where the far-field conditions are not applicable. More, the effect of limited sample support is analyzed for these arrays and the structure of the interference covariance matrix is exploited for this case of interest. For the distributed aperture radars the near-field effect is more important than in the previous case; furthermore, due to the relative motion between the antenna elements and the interference sources, the environment is non-stationary and an adaptive algorithm to counteract this non-ideality is introduced. The performance of the developed receivers are analyzed in terms of probability of detection versus the Signal to Noise plus Interference Ratio (SINR). The results show that the STAP techniques are strongly affected by the mismatches from the ideal conditions and that it is very useful to account for them in the development stage.

The thesis is organized as follows. In Chapter 1 the adaptive radar detection is introduced. The detection is based on Space-Time Adaptive Processing (STAP) techniques. Two existing receivers, GLRT and AMF, both based on the ML estimation of the unknown parameters of the transmission, are presented. Chapter 2 introduces to the bistatic radar configuration. In Chapter 3 the uniform linear arrays in presence of mutual coupling and near-field effects are analyzed; two receivers, GLRT and AMF, are derived under these conditions. Their performances are compared with that of the corresponding classical ones. Furthermore, the structure of the interference covariance matrix is exploited to circumvent the limited sample support size. In the case of uniform linear arrays this matrix is persymmetric and the GLRT, based on this particular structure of the interference covariance matrix, is developed; the performance of this receiver are compared with that achievable using the conventional GLRT, considering different amount of secondary data. In Chapter 4 the detection is based on distributed aperture radars. A time-orthogonal receiver based on waveform diversity is developed. The relative motion between interference sources and antennas leads to the non-stationarity of the environment; in fact, the Doppler frequency of the clutter is non-stationary with the range cells. The Joint Domain Localized (JDL) algorithm is introduced in the processing scheme to improve the achievable performance. The performance of the new receivers are analyzed versus the SINR. Finally, in the last chapter we report the conclusions about this work; the experimental results reported in the previous chapters show the improvement achievable when mismatches from the ideality conditions are taken in account.

# Chapter 1

## Adaptive Radar Detection

The radar detection purpose is the identification of target in presence of disturbance. The signal always contains a component due to noise and may contain components due to both desired target and undesired interference. Interference means jamming, clutter or both.

The radar system under consideration is based on multiple signals sent by a transmitter and on an array of antennas; the array is used to filter the signals in the space-time field to exploiting their spatial characteristic [60]. This filtering may be expressed in terms of a dependence upon angle or wavenumber. Viewed in the frequency domain this filtering is done by combining the outputs of the array sensors with complex gains that enhance or reject signals according to their spatial dependence. Usually, the idea is to spatially filter the field in order to enhance a signal from a particular angle, or a set of angles, by a constructive combination and to reject the disturbance from other angles by destructive interference. Two aspects are very important and determine the performance of a spatial filter. First, the geometry establishes basic constraints upon the operations of the filter; for example, a linear array can resolve only one angular component, that leads to a cone of uncertainty and right/left ambiguity. The second aspect is the design of the complex weightings of the data at each sensor output; the choice of these weightings determines the spatial filtering characteristics of the array for a given geometry.

The spatial array configurations are differentiated upon the placement of the elements. The possible configurations are

**linear arrays** : the elements are placed upon one line, thus along one dimension; Fig. 1.1 shows a linear array with generic interelement spacing;

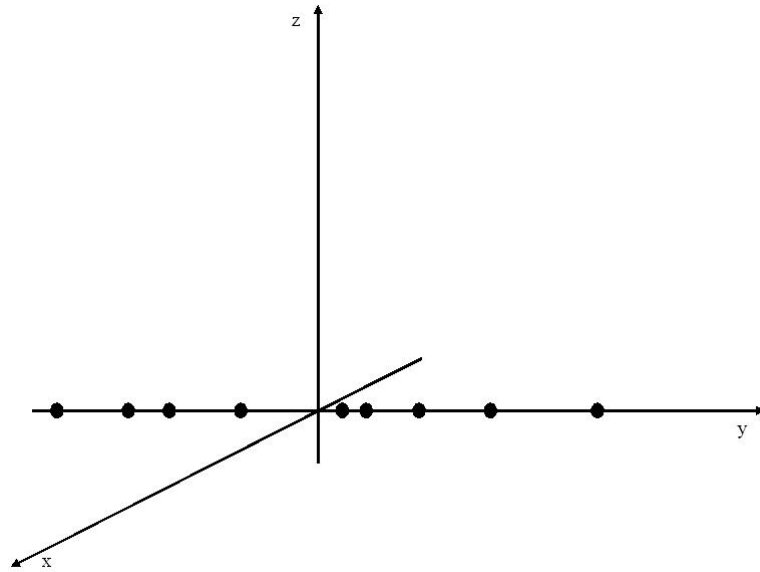


**Figure 1.1:** Linear array configuration. The antenna elements, denoted by the black circles, are displaced along one line.

**planar arrays** : the elements are displaced upon one plane, thus along two dimensions; Fig. 1.2 shows a generic planar array;

**spatial arrays** : the elements are displaced in the space, along three dimensions; Fig. 1.3 shows a generic spatial array.

The spatial configurations of interest for the aims of this work are two:

1. *uniform linear array (ULA)*,
2. *distributed aperture radar*.

*Uniform Linear Arrays* are a particular kind of linear arrays; the interelement spacing is the same between each element and thus it is very easy to locate each element; in fact, the only important characteristic is the number of the antenna respect to one chosen as reference. *Distributed Aperture Radars* are, in general, spatial arrays, where the interelement spacing is very high respect to the wavelength. In the next chapters these configurations will be considered and analyzed.

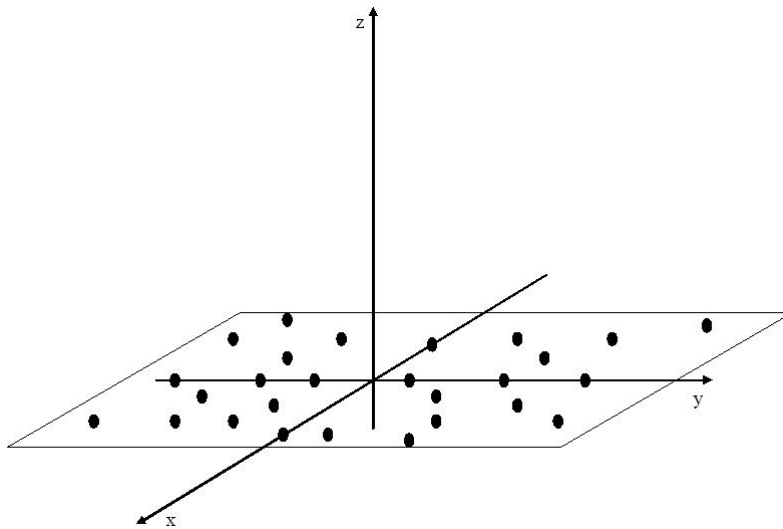


**Figure 1.2:** Planar array configuration. The antenna elements, denoted by the black circles, are displaced upon a plane.

The chapter is organized as follows. In Section 1.1 the system is modeled and analyzed; first, it is introduced the signaling scheme and then the target model and the interference model are derived; finally, the STAP techniques are presented. In Section 1.2 the classical detection theory is presented and two conventional receivers, the Generalized Likelihood Ratio test and the Adaptive Matched Filter, are introduced; both of them are derived under the ideal conditions of absence of mutual coupling, far-field conditions, sufficient number of secondary data for covariance estimate and stationarity of the environment.

## 1.1 System model

The radar transmits a coherent burst of  $M$  pulses at a constant *pulse repetition frequency (PRF)*  $f_r = 1/T_r$ , where  $T_r$  is the *pulse repetition interval (PRI)*. The transmitter carrier frequency is  $f_0 = c/\lambda_0$ , where  $c$  is the propagation velocity. The time interval over which the waveform returns are collected is commonly referred to as the *coherent processing interval (CPI)*. The CPI length is equal to  $MT_r$ . A pulse waveform of duration  $T_p$  and bandwidth  $B$  is assumed. In Fig. 1.4 the burst and some of these features are depicted. On

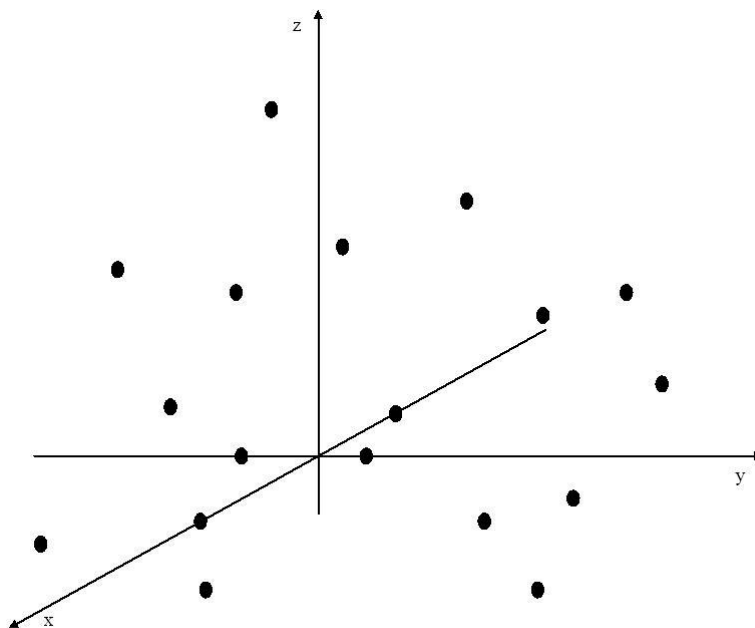


**Figure 1.3:** Spatial array configuration. The antenna elements, denoted by the black circles, are displaced along three dimensions.

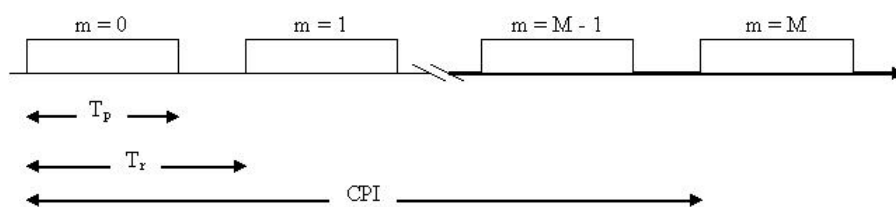


**Figure 1.4:** Pulses burst with some features emphasized.

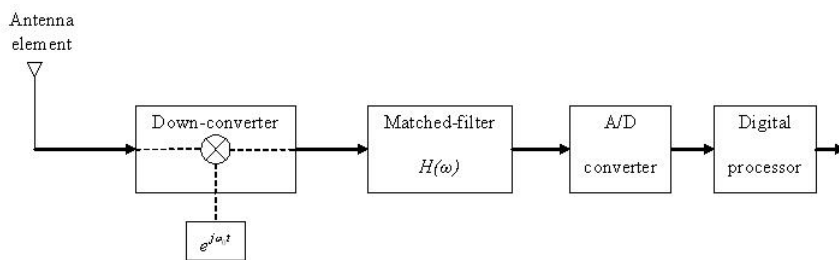


**Figure 1.5:** Processing for each array element channel.

receive, each element of the array has its own down-converter, matched filter receiver and A/D converter, as shown in Fig. 1.5. Since each receiver is a matched filter, the receiver bandwidth  $B$  is taken equal to that of the transmitted pulse. Matched filter is done separately on the returns from each pulse, after which the signals are sampled by the A/D converter and sent to a digital processor. The digital processor performs all subsequent radar signal and data processing. For each PRI,  $G$  time (range) samples are collected to cover the range interval. With  $M$  pulses and  $N$  receiver channels, the received data for one CPI comprises  $GMN$  complex baseband samples. This multidimensional data set is often visualized as the  $G \times M \times N$  cube of complex samples shown in Fig. 1.6.

Let  $y_{nmg}$  be the complex sample from the  $n^{\text{th}}$  element, the  $m^{\text{th}}$  pulse and the  $g^{\text{th}}$  range gate. The spatial snapshot, i.e. the  $N \times 1$  vector of antenna element outputs, relative to the  $g^{\text{th}}$  range gate and the  $m^{\text{th}}$  pulse is  $y_{mg}$ . The  $N \times M$  matrix  $\mathbf{Y}_g$  consists of the spatial snapshots for all pulses at the range of interest

$$\mathbf{Y}_g = [y_{0g}, y_{1g}, \dots, y_{(M-1)g}]. \quad (1.1)$$

This matrix is represented by the shaded slice of the datacube in Fig.1.6. The rows of  $\mathbf{Y}_g$  represent the temporal (pulse-by-pulse) samples for each antenna element. Beamforming is an operation that combines the rows of  $\mathbf{Y}_g$ , while combining the columns is a temporal, or Doppler, filtering operation. The data for a single range gate, termed the *space-time snapshot*, is the  $MN \times 1$  vector made stacking the columns of  $\mathbf{Y}_g$

$$\mathbf{y}_g = \text{vec}(\mathbf{Y}_g) = [y_{0g}y_{1g} \dots y_{(M-1)g}]^T. \quad (1.2)$$

where  $(\cdot)^T$  denotes the transpose operation. The aim of this work is the detection at a fixed range gate. For this reason, the subscript  $g$  is not important and

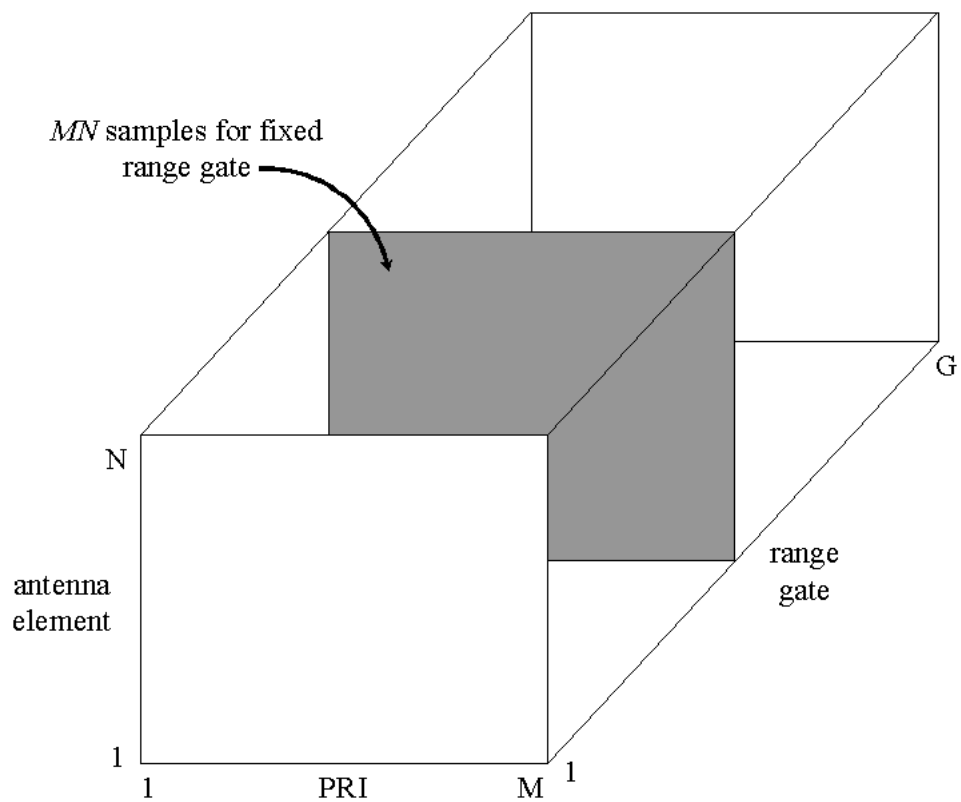


**Figure 1.6:** The radar CPI datacube.

it will drop in the rest of the work. The space-time snapshot at the range gate of interest will be denoted as  $\mathbf{y}$ , while  $\mathbf{y}_m$  denotes the spatial snapshot for the  $m^{\text{th}}$  PRI at this range.

The surveillance radar is to ascertain whether targets are present in the data. The detection is based on a binary hypothesis test; given a space-time snapshot the signal processor must make a decision as to which of the two hypotheses is true

$$\begin{cases} H_0 : \mathbf{y} = \mathbf{y}_u \\ H_1 : \mathbf{y} = \alpha_t \mathbf{s}_t + \mathbf{y}_u \end{cases} \quad (1.3)$$

where  $H_0$  denotes the hypothesis of target absent and  $H_1$  the hypothesis of target present. The vector  $\mathbf{s}_t$  is the known response of the system to a unit amplitude target, termed as *steering vector*, and  $\alpha_t$  is the unknown target amplitude. The component  $\mathbf{y}_u$  encompasses any interference or noise component of the data. Three components of undesired signals are considered: thermal noise, jamming and clutter; in the section 1.1.2 they are analyzed and modeled.

### 1.1.1 Target model

A target is defined as a moving point scatterer that is to be detected. The component of the space-time snapshot at the range gate corresponding to the target range  $R_t$  will be derived. The target is also described by its azimuth  $\varphi_t$ , elevation  $\theta_t$ , relative velocity with respect to the radar  $v_t$  and *radar-cross-section* (RCS)  $\sigma_t$ ; the radar-cross-section describes the extent to which an object reflects an incident electromagnetic wave. It is a measure of a target's ability to reflect radar signals in the direction of the radar receiver, i.e. it measures the ratio of the backscattered power in the direction of the radar (from the target) to the power density that is intercepted by the target. The conceptual definition of the RCS includes the fact that not all of the radiated energy falls on the target. The RCS depends on the object's size, reflectivity of its surface and directivity of the radar reflection caused by the object's geometric shape; the reflectivity is defined by the percent of the intercepted power reradiated by the target, while the directivity represents the ratio of the power scattered back in the radar's direction to the power that would have been backscattered had the scattering been uniform in all directions, i.e. isotropic [14]. It is defined as

$$\sigma_t = \text{Geometric Cross Section} \times \text{Reflectivity} \times \text{Directivity} \quad (1.4)$$

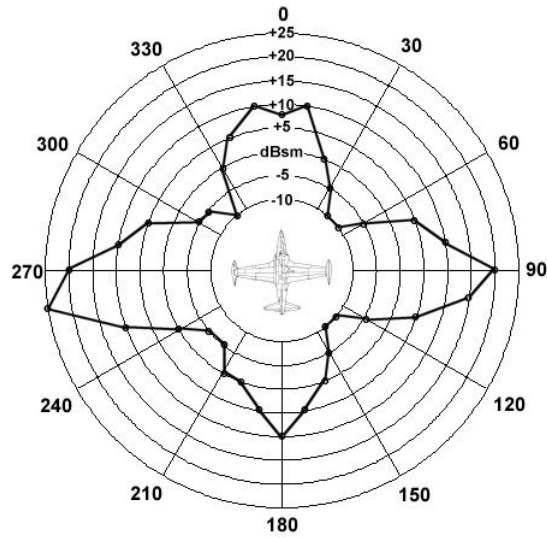


Figure 1.7: Radar-cross-section polar plot.

and can also be represented as the ratio between the power of the backscattered wave and the power of the incident wave

$$\sigma_t = 4\pi \frac{P_b}{P_i}, \quad (1.5)$$

where  $P_b$  is the power reflected toward the radar and  $P_i$  is the power intercepted by the object. While it is dependent also on the shape of the object, the RCS is a function of the portion of the object illuminated. Fig. 1.7 shows the plot of a measured RCS for a T-33 jet. This plot allows us to better see the trends in RCS behavior around the aircraft. The largest radar returns can be seen from the sides of the plane, where the large vertical tail and fuel tanks produce strong reflections. Both the forward and aft aspects also produce relatively large peaks in RCS that are probably due to reflections off the blades of the jet engines. The smallest RCS measurements tend to come from the corners of the aspect envelope where there are no surfaces perpendicular to the radar source and the engines are shielded from view. While the magnitudes of RCS values for other planes will vary significantly from those shown for the T-33, the trends illustrated here are probably representative of most other aircraft.

The full array transmits a coherent burst of pulses

$$x(t) = a_t u(t) e^{j(\omega_0 t + \psi)} \quad (1.6)$$

where

$$u(t) = \sum_{m=0}^{M-1} u_p(t - mT_r) \quad (1.7)$$

is the signal's complex envelope and  $u_p(t)$  is the complex envelope of a single pulse. The transmit signal amplitude is  $a_t$  and a random phase  $\psi$ , uniformly distributed in  $[0, 2\pi)$ , is also included. The pulse waveform of duration  $T_p$  is assumed having unit energy

$$\int_0^{T_p} |u_p(t)|^2 dt = 1. \quad (1.8)$$

where  $|\cdot|$  is the modulus of a complex number.

The target echo is received by each of the  $N$  elements. Ignoring relativistic effects, the target signal at the  $n^{\text{th}}$  antenna element,  $\tilde{x}_n(t)$  is given by [13]

$$\tilde{x}_n(t) = \alpha_r u(t - \tau_n) e^{j2\pi(f_0 + f_t)(t - \tau_n) + j\psi} \quad (1.9)$$

where  $\alpha_r$  is the echo amplitude and

$$f_t = \frac{2v_t}{\lambda_0} \quad (1.10)$$

is the target Doppler frequency. The *normalized Doppler* is defined as

$$\varpi_t = f_t T_r = \frac{f_t}{f_r}. \quad (1.11)$$

The target delay  $\tau_n$  to the  $n^{\text{th}}$  element consists of two components

$$\tau_n = \tau_t + \tau_n^l \quad (1.12)$$

where  $\tau_t = 2R_t/c$  is the round trip delay and

$$\tau_n^l = -\frac{\hat{\mathbf{k}}(\varphi_t, \theta_t) \cdot \mathbf{r}_n}{c} \quad (1.13)$$

is the relative delay measured from the phase reference to the  $n^{\text{th}}$  element;  $\hat{\mathbf{k}}(\varphi_t, \theta_t)$  is the propagation unit vector of the wave and  $\mathbf{r}_n$  is the position vector of the  $n^{\text{th}}$  element. In Fig. 1.8 these vectors are shown. The transmitted waveform is typically assumed narrowband and thus the relative delay term  $\tau_n^l$

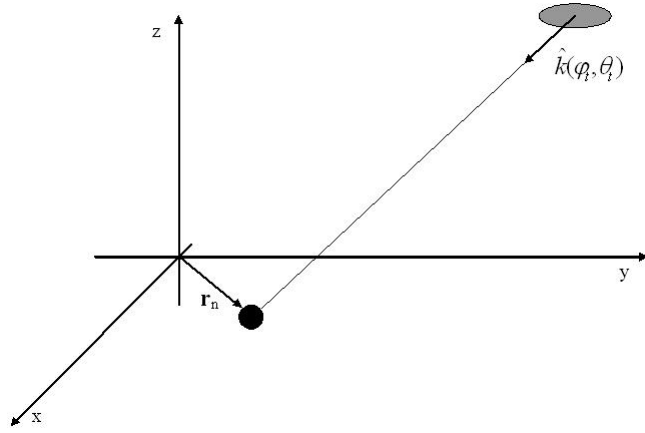


**Figure 1.8:** Radar geometry: the vector  $\mathbf{r}_n$  locates the  $n^{\text{th}}$  element of the array and  $\hat{\mathbf{k}}(\varphi_t, \theta_t)$  is the wave propagation unit vector from the target.

is insignificant within the complex envelope term of equation (1.9) [7]. Thus, the received signal becomes

$$\tilde{x}_n(t) = \alpha_r u(t - \tau_t) e^{j2\pi(f_0 + f_t)(t - \tau_n) + j\psi} \quad (1.14)$$

which becomes, including into the random phase term  $\psi$  several of the fixed phase terms,

$$\tilde{x}_n(t) = \alpha_r e^{j\psi} u(t - \tau_t) e^{j2\pi f_0 t} e^{j2\pi f_t t} e^{-j2\pi f_0 \tau_n'} \quad (1.15)$$

The signal is first down-converted; each pulse of the baseband signal is matched filter with the receiver filter

$$h(t) = u_p^*(-t) \quad (1.16)$$

where  $(\cdot)^*$  denotes the complex conjugate and thus the signal becomes

$$y_n(t) = \alpha_r e^{j\psi} e^{-j2\pi f_0 \tau_n'} \sum_{m=0}^{M-1} e^{j2\pi m f_t T_r} \chi(t - \tau_t - mT_r, f_t) \quad (1.17)$$

where  $\chi(\tau, f)$  is the *waveform ambiguity function* [20]

$$\chi(\tau, f) = \int_{-\infty}^{+\infty} u_p(\beta) u_p^*(\beta - \tau) e^{j2\pi f \beta} d\beta \quad (1.18)$$

which results when the expression for the complex envelope of the linear time-invariant (LTI) filter output due to a discrete scatterer is written as a function of the scatterer's delay and Doppler shift [21]. The ambiguity function, originally put forward for radar applications by Woodward [22], describes the response of a particular range-velocity resolution cell of a radar to a point target, as the target range and velocity vary. Radar performance in terms of capability to resolve target and clutter scatterers in range and velocity dimensions can be assessed by direct examination of the ambiguity function surface in the range-velocity ambiguity plane. Target signal-to-clutter power ratio can be calculated for specified radar and target geometries by integrating the product of ambiguity function and the clutter and power target distributions over all ranges and velocities where target or clutter are present [23]. Thus, it is a useful tool for studying the interaction of a pulse Doppler radar with its target and clutter environment. Using the ambiguity function, the effects of varying diverse design parameters can be quantified directly in terms of their effect on the target signal-to-clutter ratio [21].

Going back to the treatment, the pulse waveform normalization (1.8) implies

$$\chi(0, 0) = 1. \quad (1.19)$$

Consider only the target range gate and let  $t_m = \tau_t + mT_r$ ,  $m = 0, \dots, M-1$ , be the sample times for each PRI at this range gate. The target samples are thus given by

$$y_{nm} = y_n(t_m) = \alpha_r e^{j\psi} \chi(0, f_t) e^{-j2\pi f_0 \tau_n'} e^{j2\pi m \varpi t}. \quad (1.20)$$

The pulse waveform time-bandwidth product and the expected range of Doppler frequencies are assumed such that the waveform is insensitive to target Doppler shift, i.e.

$$\chi(0, f) \simeq 1. \quad (1.21)$$

Grouping the random phase term and the received amplitude in one term  $\alpha_t = \alpha_r e^{j\psi}$ , the final expression for the sample relative to the  $n^{\text{th}}$  element and  $m^{\text{th}}$  PRI is

$$y_{nm} = \alpha_t e^{-j2\pi f_0 \tau_n'} e^{j2\pi m \varpi t}, \quad \begin{array}{l} n = 0, \dots, N-1 \\ m = 0, \dots, M-1 \end{array}. \quad (1.22)$$

Let  $\xi_t$  be the *single-pulse* Signal-to-Noise Ratio (SNR) for the *single antenna element* on receive; the target power is thus

$$\mathbb{E}\{|\alpha_t|^2\} = \sigma^2 \xi_t, \quad (1.23)$$

where  $\sigma^2$  is the thermal noise power per element,  $\mathbb{E}\{\cdot\}$  is the statistical expectation value. The target amplitude is thus

$$\alpha_t = \sqrt{\sigma^2 \xi_t}. \quad (1.24)$$

This model is easily generalized to random amplitudes as well.

Equation (1.22) shows that one exponential term depends on the spatial index  $n$  and the other exponential term on the temporal index  $m$ . The *spatial snapshot* for the  $m^{\text{th}}$  PRI can be written as

$$\mathbf{y}_m = [y_{0m}, y_{1m}, \dots, y_{(N-1)m}]^T = \alpha_t e^{j2\pi m \varpi_t} \mathbf{a}(\mathbf{\Upsilon}_t), \quad (1.25)$$

and the  $N \times 1$  *spatial steering vector*  $\mathbf{a}(\mathbf{\Upsilon}_t)$  is defined as

$$\mathbf{a}(\mathbf{\Upsilon}_t) = [e^{-j2\pi f_0 \tau'_0}, e^{j2\pi f_0 \tau'_1}, \dots, e^{j2\pi f_0 \tau'_{N-1}}]^T \quad (1.26)$$

and  $\mathbf{\Upsilon}_t$  is the *relative delays vector*

$$\mathbf{\Upsilon}_t = [\tau'_0, \tau'_1, \dots, \tau'_{(N-1)}]^T. \quad (1.27)$$

In the same way, the  $M \times 1$  *temporal steering vector* is introduced

$$\mathbf{b}(\varpi_t) = [1, e^{j2\pi \varpi_t}, \dots, e^{j2\pi(M-1)\varpi_t}]^T \quad (1.28)$$

that assumes a Vandermonde form because the waveform is a uniform PRF and the target velocity is constant. Using equations (1.26) and (1.28), the target data can be assembled in the *space-time snapshot*

$$\begin{aligned} \mathbf{y}_t &= \alpha_t \left[ \mathbf{a}(\mathbf{\Upsilon}_t), e^{j2\pi \varpi_t} \mathbf{a}(\mathbf{\Upsilon}_t), \dots, e^{j2\pi(M-1)\varpi_t} \mathbf{a}(\mathbf{\Upsilon}_t) \right]^T = \\ &= \alpha_t \mathbf{b}(\varpi_t) \otimes \mathbf{a}(\mathbf{\Upsilon}_t) \end{aligned} \quad (1.29)$$

where “ $\otimes$ ” denotes the Kronecker product. Finally, the  $MN \times 1$  *space-time steering vector*

$$\mathbf{s}(\mathbf{\Upsilon}, \varpi) = \mathbf{b}(\varpi) \otimes \mathbf{a}(\mathbf{\Upsilon}) \quad (1.30)$$

is, in general, the response of the target with relative delays  $\mathbf{\Upsilon}$  and normalized Doppler  $\varpi$ . If a target is in the data, it contributes a term

$$\mathbf{y}_t = \alpha_t \mathbf{s}_t \quad (1.31)$$

where  $\mathbf{s}_t = \mathbf{s}(\mathbf{\Upsilon}_t, \varpi_t)$  may also be called the *target steering vector*. It contains the modeled variation of the signal amplitude and phase among the array inputs as well as a pulse-to-pulse variations, such as those relating to a particular target Doppler velocity.

### 1.1.2 Interference Sources

The interference is composed by all the sources that make difficult the detection. As reported above, the potential useful signal is immersed in the disturbance. The interesting disturbance sources for the radar detection are three: thermal noise, jamming and clutter. They are mutually uncorrelated; thus, the interference covariance matrix is the sum of three parts

$$\mathbf{M} = \mathbf{M}_{no} + \mathbf{M}_j + \mathbf{M}_c \quad (1.32)$$

where  $\mathbf{M}_{no}$  is relative to the thermal noise,  $\mathbf{M}_j$  to the jamming and  $\mathbf{M}_c$  to the clutter. In the rest of this section, these sources are analyzed.

#### Thermal Noise

The first undesired signal that a potential target must contend is the *noise*. Assume that the only noise source is internally generated receiver noise, which is always present on each channel. Each element has its own receiver and thus the noise processes are mutually uncorrelated. Assume that the instantaneous bandwidth is large compared with the PRF [7]. Therefore, the noise samples on a single element taken at time instants separated by a nonzero multiple of the PRI are temporally uncorrelated. Let  $y_{nm}$  be the noise sample on the  $n^{\text{th}}$  element for the  $m^{\text{th}}$  PRI. The first assumption above is a statement of a spatial noise correlation

$$\mathbb{E}\{y_{n_1 m} y_{n_2 m}^*\} = \sigma^2 \delta_{n_1 - n_2} \quad (1.33)$$

where

$$\delta_m = \begin{cases} 1 & , \quad m = 0 \\ 0 & , \quad m \neq 0 \end{cases} \quad (1.34)$$

is the Kronecker delta and  $\sigma^2$  is the noise power per element. The second assumption above leads to the temporal noise correlation

$$\mathbb{E}\{y_{nm_1} y_{nm_2}^*\} = \sigma^2 \delta_{m_1 - m_2}. \quad (1.35)$$

Equations (1.33) and (1.35) lead to the noise component of the space-time covariance matrix being the scaled identity matrix

$$\mathbf{M}_{no} = \mathbb{E}\left\{\mathbf{y}_{no} \mathbf{y}_{no}^\dagger\right\} = \sigma^2 \mathbf{I}_M \otimes \mathbf{I}_N = \sigma^2 \mathbf{I}_{MN} \quad (1.36)$$

where  $(\cdot)^\dagger$  is the conjugate transpose of a vector. In terms of the radar system parameters, the noise power is  $\sigma^2 = N_0 B$ .

This analysis holds only if the dominant source of noise is internally generated by each receiver. In some cases, for example when the sky noise contribution is considerable, the hypothesis of uncorelation is no more valid. In that cases, the noise covariance matrix can not more be expressed in terms of a Kronecker product between identity matrices, showing non zero terms outside of the principal diagonal.

### **Jamming**

In this section the jamming contribution to a space-time snapshot is analyzed and its covariance matrix is derived. The jamming is an intentional signal used toward a radar to make hard the detection. There are three types of jamming: spot, sweep and barrage:

**Spot jamming** occurs when a jammer focuses all of its power on a single frequency. While this would severely degrade the ability to track on the jammed frequency, a frequency agile radar would hardly be affected because the jammer can only jam one frequency. While multiple jammers could possibly jam a range of frequencies, this would consume a great deal of resources to have any effect on a frequency-agile radar, and would probably still be ineffective.

**Sweep jamming** is when a jammer's full power is shifted from one frequency to another. While this has the advantage of being able to jam multiple frequencies in quick succession, it does not affect them all at the same time, and thus limits the effectiveness of this type of jamming. Although, depending on the error checking in the devices this can render a wide range of devices effectively useless.

**Barrage jamming** is the jamming of multiple frequencies at once by a single jammer. The advantage is that multiple frequencies can be jammed simultaneously; however, the jamming effect can be limited because this requires the jammer to spread its full power between these frequencies. So the more frequencies being jammed, the less effectively each is jammed. It is accomplished by transmitting a band of frequencies that is large with respect to the bandwidth of a single emitter. Barrage jamming may be accomplished by presetting multiple jammers on adjacent frequencies, by using a single wideband transmitter, or by using a transmitter capable of frequency sweep fast enough to appear radiating simultaneously over wide band.

In this analysis only the barrage noise jamming that originates from land-based or airborne platforms at long range from the radar will be considered. As in [7], the jamming energy is assumed to fill the radar's instantaneous bandwidth. It is considered that the signal's propagation time across the array is small relative to  $1/B$ , i.e. that is no signal decorrelation across the array. The radar PRF is assumed significant less than the instantaneous bandwidth; thus, the jamming decorrelates over the pulses. It follows that the jamming is spatially correlated from element to element and temporally uncorrelated from pulse to pulse. Thus, the jamming looks like thermal noise temporally and like target, or clutter source, spatially.

We start our analysis considering a single jammer at elevation  $\theta_j$ , azimuth  $\varphi_j$  and range  $R_j$ . Let  $J_0$  the jammer power spectral density received by one array element [12]. The received Jammer-to-Noise Ratio (JNR) at the element is given by

$$\xi_j = \frac{J_0}{N_0}, \quad (1.37)$$

where  $N_0$  is the received noise power spectral density. The jamming component of the spatial snapshot for the  $m^{\text{th}}$  PRI is then

$$\mathbf{y}_m = \alpha_m \mathbf{a}_j \quad (1.38)$$

where  $\alpha_m$  is the jammer amplitude for the  $m^{\text{th}}$  PRI and  $\mathbf{a}_j = \mathbf{a}(\varphi_j, \theta_j)$  is the jammer steering vector. The jammer space-time snapshot may be written as

$$\mathbf{y}_j = \alpha_j \otimes \mathbf{a}_j \quad (1.39)$$

where  $\alpha_j = [\alpha_0 \ \alpha_1 \ \dots \ \alpha_{M-1}]^T$  is a random vector that contains the jammer amplitudes. Assume for simplicity that the jammer signal (aspect and power spectral density) is stationary over a CPI. Thus, it is simple to find the temporal correlation between two generic contributes

$$\mathbb{E}\{\alpha_{m_1} \alpha_{m_2}^*\} = \sigma^2 \xi_j \delta_{m_1 - m_2} \quad (1.40)$$

and in vector form for all the contributes

$$\mathbb{E}\{\alpha_j \alpha_j^\dagger\} = \sigma^2 \xi_j \mathbf{I}_M. \quad (1.41)$$

Using equation (1.41) it is possible to find the space-time covariance matrix

$$\begin{aligned} \mathbf{M}_j &= \mathbb{E}\{\mathbf{y}_j \mathbf{y}_j^\dagger\} = \sigma^2 \xi_j \mathbf{I}_M \otimes \mathbf{a}_j \mathbf{a}_j^\dagger \\ &= \mathbf{I}_M \otimes \mathbf{\Phi}_j \end{aligned} \quad (1.42)$$

where  $\Phi_j$  is the jammer spatial covariance matrix

$$\Phi_j = \mathbb{E} \left\{ \mathbf{s}_m \mathbf{s}_m^\dagger \right\} = \sigma^2 \xi_j \mathbf{a}_j \mathbf{a}_j^\dagger. \quad (1.43)$$

The extension to multiple jamming signals is straightforward. Consider  $J$  jamming sources and let  $\varphi_k$ ,  $\theta_k$  and  $\xi_k$  be respectively the azimuth angle, the elevation angle and the JNR for the  $k^{\text{th}}$  source, with  $k = 0, \dots, J - 1$ . The equation (1.42) is still valid, with the only difference in the jammer spatial covariance matrix

$$\Phi_j = \mathbf{A}_j \Xi_j \mathbf{A}_j^H \quad (1.44)$$

where

$$\mathbf{A}_j = [\mathbf{a}(\varphi_1, \theta_1), \mathbf{a}(\varphi_2, \theta_2), \dots, \mathbf{a}(\varphi_{J-1}, \theta_{J-1})] \quad (1.45)$$

is the  $N \times J$  matrix of the jammer spatial steering vectors,  $\Xi_j$  is the  $J \times J$  jammer source covariance matrix and  $(\cdot)^H$  is the Hermitian of a matrix. Due to the assumption of uncorrelation among the jamming samples from different PRIs, the space-time covariance matrix (1.42) is block diagonal and off-diagonal  $N \times N$  blocks are zero. The stationary assumption results in the blocks along the diagonal being all equal to a single spatial covariance matrix.

### Clutter

Radar clutter is generally defined as the echoes from any scatterers deemed to be not of tactical significance [7]. Clutter plays an important role in determining radar systems performance in many applications [16]; for example, in maritime environments sea clutter may limit the detection performance of radars when searching small targets, such as periscopes [17], as well as large targets [18]. Of the various interference sources, clutter is the most complicated because it is distributed both in angle and range and is spread in Doppler frequency due to the relative motion between antenna elements and clutter sources. Thus, it is important, in the design of a detection algorithm, to have a good knowledge of the clutter statistics. There are more than one kind of clutter types; in particular, as reported in [15], possible types are for example

**Fixed ground clutter** : fixed objects on the ground produce undesired radar reflections.

**Second-time-around effect** : returns are being received due to illumination of clutter beyond the non-ambiguous range by the next-to-last pulse

transmitted. These returns are prevalent where conditions for anomalous propagation exist such that the radar waves are bent back downward with the range and intercept the ground at great distances (greater than that corresponding to the interpulse period). This effect is also prevalent in regions where mountains exist beyond the non-ambiguous range.

**Precipitation clutter** : this is due to precipitation, like for example the rain.

**Angels clutter** : the so-called ‘‘angels clutter’’ refers to all returns which cannot be explained as being ground or precipitation clutter or targets. The possible sources are, for example, birds, single or flocks of birds, and swarms of insects.

**Surface vehicles** : the surface vehicles have a cross section in the same range as aircrafts.

Ground clutter is one of the most significant clutter type and in the rest of the section we will refer to it. Following the analysis reported in [7], a model is developed for the ground clutter component of a space-time snapshot for a given range and the properties of the clutter space-time covariance matrix are considered.

The return from a discrete ground clutter source has the form as a target echo. Unlike a target, ground clutter is distributed in range; it exists over a region extending from the platform to the radar horizon. Ground clutter also exists over all azimuths and a region in elevation angle bounded by the horizon elevation. Considering the radar being at an altitude of  $h_a$  and assuming a spherical earth with the effective earth radius  $a_e$  [19], the *radar range horizon* can be approximated by

$$R_h \approx \sqrt{2a_e h_a}. \quad (1.46)$$

Let  $R_u = c/(2f_r)$  be the *radar’s unambiguous range*. Consider the clutter return from the  $l^{\text{th}}$  range gate, which corresponds to the true range  $R_c$ , where  $0 < R_c < R_u$ . If the unambiguous range is greater than the horizon range, i.e.  $R_u > R_h$ , the clutter is said to be unambiguous in range. In this case the clutter component of the space-time snapshot consists of clutter from at most one range. If the radar horizon is larger than the unambiguous range, some or all the range gates will have clutter contributions from multiple ranges. In this case the clutter is said to be ambiguous in range. Let  $R_i = R_c + (i - 1)R_u$  be the  $i^{\text{th}}$  ambiguous range corresponding to the range of interest. The clutter component consists of the superposition of the returns from all the ambiguous

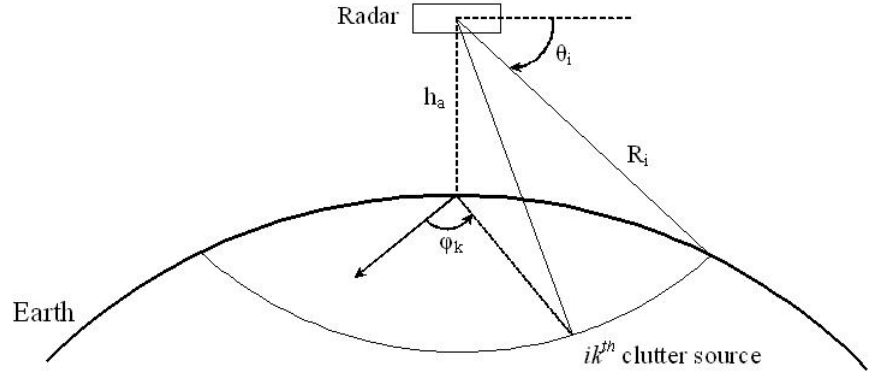


**Figure 1.9:** A ring of ground clutter for a fixed range.

ranges within the radar horizon. Denote the number of range ambiguities by  $N_r$ .

As an approximation to a continuous field of clutter, the clutter return from each ambiguous range will be modeled as the superposition of a large number  $N_c$  of independent clutter sources that are evenly distributed in azimuth about the radar. The location of the  $i k^{\text{th}}$  source is described by its azimuth angle  $\varphi_k$  and ambiguous range  $R_i$ , which corresponds to an elevation angle  $\theta_i$ . In Fig. 1.9 the clutter ring is depicted; it is the locus of clutter sources with the same range  $R_i$ , or the same elevation angle  $\theta_i$ , and different azimuth angle  $\varphi_k$ . The corresponding wavenumber is

$$\psi_{ik} = \hat{\mathbf{k}}(\varphi_k, \theta_i) \cdot \mathbf{r} \quad (1.47)$$

where  $\mathbf{r}$  is the position vector of the antenna. The normalized Doppler frequency of the  $i k^{\text{th}}$  patch will be denoted by  $\varpi_{ik}$ . The clutter component of the space-time snapshot is then given by

$$\mathbf{y}_c = \sum_{i=1}^{N_r} \sum_{k=1}^{N_c} \alpha_{ik} \mathbf{v}(\psi_{ik}, \varpi_{ik}) \quad (1.48)$$

where  $\alpha_{ik}$  is the random amplitude from the  $i k^{\text{th}}$  clutter patch.

Using the same notation of the previous subsection, denote the Clutter-to-Noise ratio (CNR) for the  $i k^{\text{th}}$  clutter source as  $\xi_{ik}$ ; the clutter amplitudes satisfy  $\mathbb{E}\{|\alpha_{ik}|^2\} = \sigma^2 \xi_{ik}$ . Assume that returns from different clutter patches are uncorrelated

$$\mathbb{E}\{\alpha_{ik} \alpha_{jl}^*\} = \sigma^2 \xi_{ik} \delta_{i-j} \delta_{k-l}. \quad (1.49)$$

The clutter space-time covariance matrix follows directly from equations (1.48) and (1.49)

$$\mathbf{M}_c = \mathbb{E} \left\{ \mathbf{y}_c \mathbf{y}_c^\dagger \right\} = \sigma^2 \sum_{i=1}^{N_r} \sum_{k=1}^{N_c} \xi_{ik} \mathbf{v}_{ik} \mathbf{v}_{ik}^\dagger \quad (1.50)$$

where  $\mathbf{v}_{ik} = \mathbf{v}(\psi_{ik}, \varpi_{ik})$ . Alternatively, the last equation can be expressed as

$$\mathbf{M}_c = \sigma^2 \sum_{i=1}^{N_r} \sum_{k=1}^{N_c} \xi_{ik} \left( \mathbf{b}_{ik} \mathbf{b}_{ik}^\dagger \right) \otimes \left( \mathbf{a}_{ik} \mathbf{a}_{ik}^\dagger \right), \quad (1.51)$$

where  $\mathbf{b}_{ik} = \mathbf{b}(\varpi_{ik})$  and  $\mathbf{a}_{ik} = \mathbf{a}(\psi_{ik})$ . Each scatterer contributes a term that is the Kronecker product of the temporal covariance matrix and the spatial covariance matrix. These two components are coupled because the clutter Doppler is a function of the angle. The matrix  $\mathbf{M}_c$  is an  $M \times M$  block matrix, where each block is an  $N \times N$  cross-covariance of the spatial snapshots from the PRIs. In [7], it has been shown that in the case of uniform linear arrays the clutter covariance matrix  $\mathbf{M}_c$  is Toeplitz-block-Toeplitz.

The expression above apply to the general case of the range-ambiguous clutter. The range-unambiguous clutter covariance matrix can be derived by the equation (1.51) dropping the  $i$  subscript, and thus the relative summation, that denotes the ambiguous range. The clutter covariance matrix can also be expressed compactly as

$$\mathbf{M}_c = \mathbf{V}_c \mathbf{\Xi}_c \mathbf{V}_c^H \quad (1.52)$$

where

$$\mathbf{V}_c = [\mathbf{v}_1, \mathbf{v}_2, \dots, \mathbf{v}_{N_c}] \quad (1.53)$$

is an  $MN \times N_c$  matrix of clutter space-time steering vectors and

$$\mathbf{\Xi}_c = \sigma^2 \text{diag}([\xi_1, \dots, \xi_{N_c}]) \quad (1.54)$$

contains the clutter power distribution.

### 1.1.3 Space Time Adaptive Processing

A *space-time* processor is defined as a linear combiner that sums the spatial samples from the elements of an antenna array and the temporal samples from the multiple pulses of a coherent waveform. The interest in the *Space-Time Adaptive Processing* (STAP) is due to its capability of maximization of the

Signal-to-Interference-plus-Noise Ratio (SINR), that is a characterization of the noise-limited performance of the radar against a target with radar cross section  $\sigma_t$  at range  $R_t$ . The probability of detection  $P_D = P\{H_1|H_1\}$  is a function of both the SINR and the probability of false alarm  $P_{FA} = P\{H_1|H_0\}$ . By maximizing SINR, the processor maximizes the probability of detection for a fixed probability of false alarm. A way to improve the detection of target with diminishing radar-cross-section at farther range is increasing the product power-aperture; system constraints and cost limit this solution, making more practicable and interesting the STAP solution. Spatial and temporal signal diversity, or degrees of freedom (DoF), greatly enhances radar detection in presence of certain types of interference. Specifically, the appropriate application of space-time DoFs efficiently maximizes SINR when the target competes with clutter and noise jamming. Space-time adaptive processing involves adaptively (or dynamically) adjusting the two-dimensional space-time filter response in an attempt at maximizing output SINR and consequently improving radar detection performance [24].

The function of a surveillance radar is to search a specified volume of space for potential targets. Within a single coherent processing interval, the search is confined in angle to the sector covered by the transmit beam for that CPI, but otherwise it covers all ranges. Consider a fixed range gate which is to be tested for target presence. The data available to the radar signal processor consists of the  $M$  pulses on each of the  $N$  elements. A space-time processor combines all the samples from the range gate of interest to produce the scalar output. In Fig. 1.10 a general block diagram for a space-time processor is depicted. The tapped delay line on each element represents the multiple pulses of a CPI, with the time delay between taps equal to the PRI. Thus, a space-time processor utilizes the spatial samples from the elements of an array antenna and the temporal samples provided by the successive pulses of a multiple-pulse waveform. The space-time processor can be represented by an  $MN$  - dimensional weight vector  $\mathbf{w}$ . Its output  $\mathbf{z}$  can be represented as the inner product of the weight vector and the snapshot of interest

$$\mathbf{z} = \mathbf{w}^\dagger \mathbf{y}. \quad (1.55)$$

One way to view a space-time weight vector is as a combined receive antenna beamformer and target Doppler filter. Ideally, the space-time processor provides coherent gain on target while forming angle and Doppler response nulls to suppress clutter and jamming. As the clutter and jamming scenario is not known in advance, the weight vector must be determined in a data-adaptive

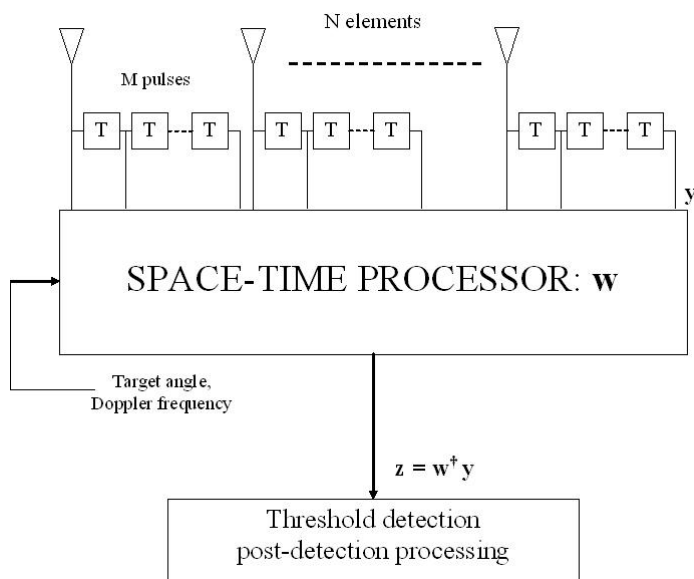


**Figure 1.10:** A general block diagram for a space-time processor.  $T$  denotes the time repetition interval.

way from the radar returns. A single weight vector is optimized for a specific angle and Doppler. Since the target angle and velocity are not known a priori, a space-time processor typically computes multiple weight vectors that form a filter bank to cover all potential target angles and Doppler frequencies.

A more complete picture of a space-time processor is shown in Fig. 1.11. The full CPI datacube is shown, with the shaded slice of data, labeled “target data” representing the data at the range of interest. This shaded portion is exactly the data represented by the tapped delay line at each element in Fig. 1.10. The space-time processor consists of three major components. First, a set of rules called the *training strategy* is applied to the data. This block derives from the CPI data a set of *training data* that will be used to estimate the interference. The training data are applied to the second block, the *weight computation*. Based on the training data, the adaptive weight vector is computed. Typically, weight computation requires the solution of linear system of equations. This block is therefore a very computation-intensive portion of space-time processor. New weight computations are performed with each set of training data. Finally, given a weight vector, the process of *weight application* refers to the

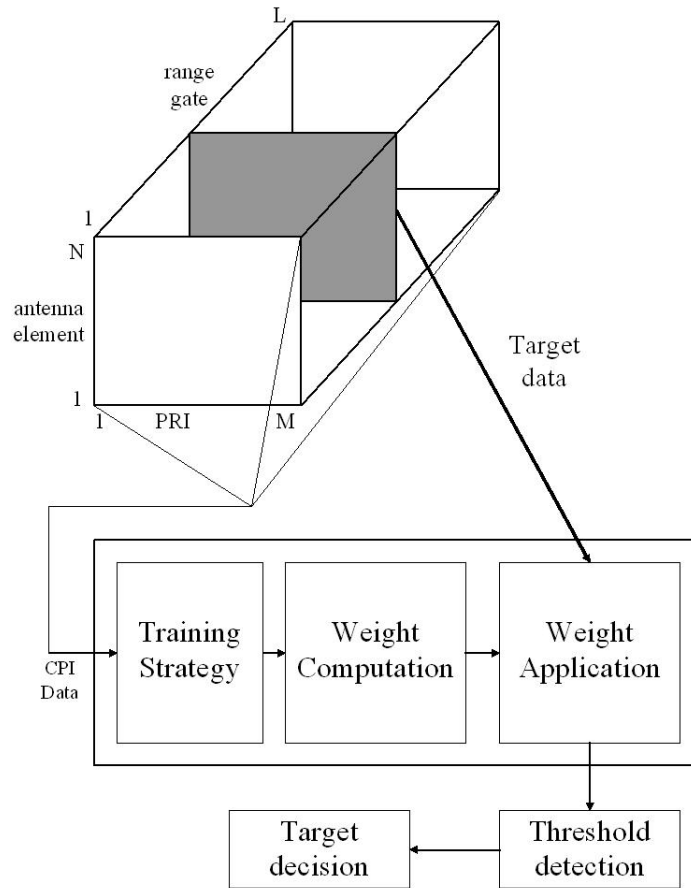


**Figure 1.11:** Data-domain view of space-time adaptive processing.

computing of the scalar output or test statistic. Weight application is a digital beamforming operation. The scalar output is then compared to a threshold to determine if a target is present at the specified angle and Doppler

$$\mathbf{z} \begin{matrix} H_1 \\ > \\ < \\ H_0 \end{matrix} \gamma. \quad (1.56)$$

where  $\gamma$  is the chosen threshold. The output of the processor is a separated scalar (or decision) for each range, angle and velocity at which the target presence is to be queried.

Because the interference is unknown a priori, it must be estimated data-adaptively from the finite amount of data comprising the CPI. The processor accepts the CPI data and implements a set of training rules to derive a *secondary data set*, called the *training data*, to be used for weight computation; the data from the range gate under test are called *primary data* and are the data analyzed to detect the possible target. The goal of the training strategy is to obtain the best estimate of the interference that exists at the range gate under test. Typically, the data from several range gates near the one of interest are used; the training data cover a range interval surrounding the range gate of interest, but not including it. A training strategy is defined by a number of factors in mind. First, the number of range gates in the training set must be sufficient to guarantee an interference estimate good enough for effective nulling. In a stationary environment, the required number of samples is well understood. Secondly, the training set must be updated or changed in accordance with the non-stationarity of the interference. The training strategy and the weight computation requirements are coupled, because for each change in the training set a new weight vector must be computed. Since the number of range gates and the CPI data is dependent on the PRI and on the instantaneous bandwidth, training strategies are most strongly affected by these two radar parameters. Given a training data set, weight computation strategies fall loosely in three categories. The first category is called *sample matrix inversion* (SMI) [25]. The SMI computation refers to all approaches that effectively compute the weight vector from the inverse of the sample covariance matrix of the training data. This class refers to algorithms that are numerically stable, whereby the weight vector is computed by a QR-decomposition of the matrix of the training data. The way in which this decomposition is computed differs the members of the class. The second class is called *subspace projection*; first the subspace spanned by the interference is estimated by performing an eigenanalysis of the sample covariance matrix or a singular value decomposition

(SVD) of the matrix of training data; then, the weight vector is computed by projecting the desired response into the subspace orthogonal to the interference subspace. Thus, the weight vector is forced to null the interference. The third class is called *subspace SMI* and combines the attributes from the other two classes. The data are first projected into a lower dimension space using some transformation and then a small SMI problem is solved with the projected data (and steering vector) in the lower dimension space. The transform may be either fixed or data-adaptive. In contrast to the subspace projections, subspace SMI preserves SINR optimality in the ideal case and computational and training requirements are lessened due to the reduced size of the SMI problem. The data collected for the training strategy are assumed to be composed only by the interference, i.e. the target is sought only in the range gate under test. Typically, the target return from range gates different by the one under test are included in the interference and classified as clutter. Including the training data in the hypothesis test leads to

$$\begin{cases} H_0 : & \begin{cases} \mathbf{y} &= \mathbf{y}_u \\ \mathbf{y}_k &= \mathbf{y}_{uk}, \quad k = 0, \dots, K-1 \end{cases} \\ H_1 : & \begin{cases} \mathbf{y} &= \alpha_t \mathbf{s}_t + \mathbf{y}_u \\ \mathbf{y}_k &= \mathbf{y}_{uk}, \quad k = 0, \dots, K-1 \end{cases} \end{cases} \quad (1.57)$$

where  $\mathbf{y}_k$  are the data from the  $k^{\text{th}}$  range gate used for collecting the training data and  $K$  is the size of the sample support needed for estimate the interference matrix. In the SMI techniques, the number of the secondary data required has to comply with

$$K \geq N + 1,$$

otherwise the sample matrix is singular. The chosen number of secondary data  $K$  must exceed  $N$  by a significant factor to prevent a serious loss in performance which may arise if the choice is not adequate. The requirements on the number of secondary data can be extremely large [8], making difficult a good estimate of the matrix. The chief reason for the requirement of many secondaries is in the presence of the interference; this implies the possibility of arbitrary correlation between interference inputs from pulse returns widely spaced in time, although it might be realistic to assume independence (but not statistical identity) of the interference inputs accompanying distinct pulse returns. Typically, the matrix is estimated via the Maximum Likelihood (ML) estimation based on the secondary data

$$\hat{\mathbf{M}} = \frac{1}{K} \sum_{k=0}^{K-1} \mathbf{y}_{uk} \mathbf{y}_{uk}^\dagger. \quad (1.58)$$

When the number of antenna elements  $N$  is high, this method limits the goodness of the approach, while collecting the required data is difficult and time expensive; it also makes computational expensive the detection.

Weight application is the formation of the processor output given the computed weight vector. In practice, a single weight vector may be applied to data comprising many range gates. The design of the weight application regions is usually coupled with the training set design, with each application region corresponding to a single training set. Weight application is an inner product, or matrix-vector product, operation. The computational load of this portion of the space-time processor scales linearly with the weight vector dimension and the number of range gates. The number of the range gates in turn depends on the radar PRF and its instantaneous bandwidth.

The processor output scalar is compared to a threshold to determine if target is present at each range-Doppler cell. Typically, a background noise estimate is provided to the detector so that it provides constant-false-alarm rate (CFAR). The selection of a training region resembles the choice of a CFAR stencil; the training set or application region data may be used to set the CFAR constant. It has been shown that with appropriate normalization of an SMI weight vector, a CFAR property can be embedded into weight computation. Different normalizations lead to the Adaptive Matched Filter detector [11] or to the Generalized Likelihood Ratio detector [8]. Their performance are similar at high SINR, but subtle differences in performance at low target SINR and with respect to sidelobe targets have been documented [79, 27, 26].

A space-time processor that computes and applies a separate weight vector to every element and pulse is said to be *fully adaptive*. The size of the weight vector of the fully adaptive processor is  $MN$ . Fully adaptive space-time processing for airborne radar was first proposed by Brennan et al. [28] and is natural extension of adaptive antenna processing to a two dimensional space-time problem [29, 30].

The data snapshot of interest, using equation (1.2), is

$$\mathbf{y} = \alpha_t \mathbf{s}_t + \mathbf{y}_u$$

where the space-time steering vector, from equation (1.30),  $\mathbf{s}_t = \mathbf{b}(\varpi_t) \otimes \mathbf{a}(\Upsilon_t)$ , is function of the relative delays vector and the normalized Doppler and  $\mathbf{y}_u$  denotes the overall interference. The optimum space-time filter [85] is given by

$$\mathbf{w} = \mathbf{M}^{-1} \mathbf{s}_t \tag{1.59}$$

where

$$\mathbf{M} = \mathbb{E} \left\{ \mathbf{y}_u \mathbf{y}_u^\dagger \right\} \quad (1.60)$$

is the interference plus noise covariance matrix. The so computed weight vector (1.59) is optimum under several criteria [31]. It maximizes the SINR, maximizes the probability of detection for a given false alarm probability and with the proper choice of a scale factor minimizes output power subject to a unity gain constraint in the target direction. The optimum processor response has high sidelobes in both angle and Doppler, because of the implied windowing of the data. These high sidelobes make the optimum processor susceptible to the detection of sidelobe targets. A block diagram of fully adaptive STAP is given in Fig. 1.12. The size of the linear system grows linearly with the size of the array or the length of the coherent processing interval. For many radar systems, the product  $MN$  is likely to range from several hundred to several thousand. The implementation of a fully adaptive approach is beyond current capabilities in real-time computing.

The fully adaptive STAP described above assumes that the interference covariance matrix is known. In many practical situations this matrix is unknown and it is estimated through the ML estimation reported in equation (1.58). The SMI weight vector is defined as in equation (1.59) substituting the matrix  $\mathbf{M}$  with its estimate

$$\hat{\mathbf{w}} = \hat{\mathbf{M}}^{-1} \mathbf{s}_t \quad (1.61)$$

and it is a suboptimum vector. This degrades the performance achievable with the fully adaptive STAP. Another loss in the performance may occur due to mismatches between the nominal steering vector  $\mathbf{s}_t$  used for the weight computation and the actual one by design (because of tapering) or by imperfect knowledge of the target direction (angle and Doppler) or both [32, 33].

## 1.2 Conventional Receivers

According to the Neyman-Pearson criterion, in order to maximize the probability of detection  $P_D$  with a constraint on the probability of false alarm  $P_{FA}$ , starting from the hypothesis test (1.3) the optimum detector is derived by the ratio of the conditional probability density functions in the two hypotheses, i.e.

$$\frac{f(\mathbf{y}|H_1)}{f(\mathbf{y}|H_0)} \underset{H_0}{\overset{H_1}{>}} \gamma \quad (1.62)$$

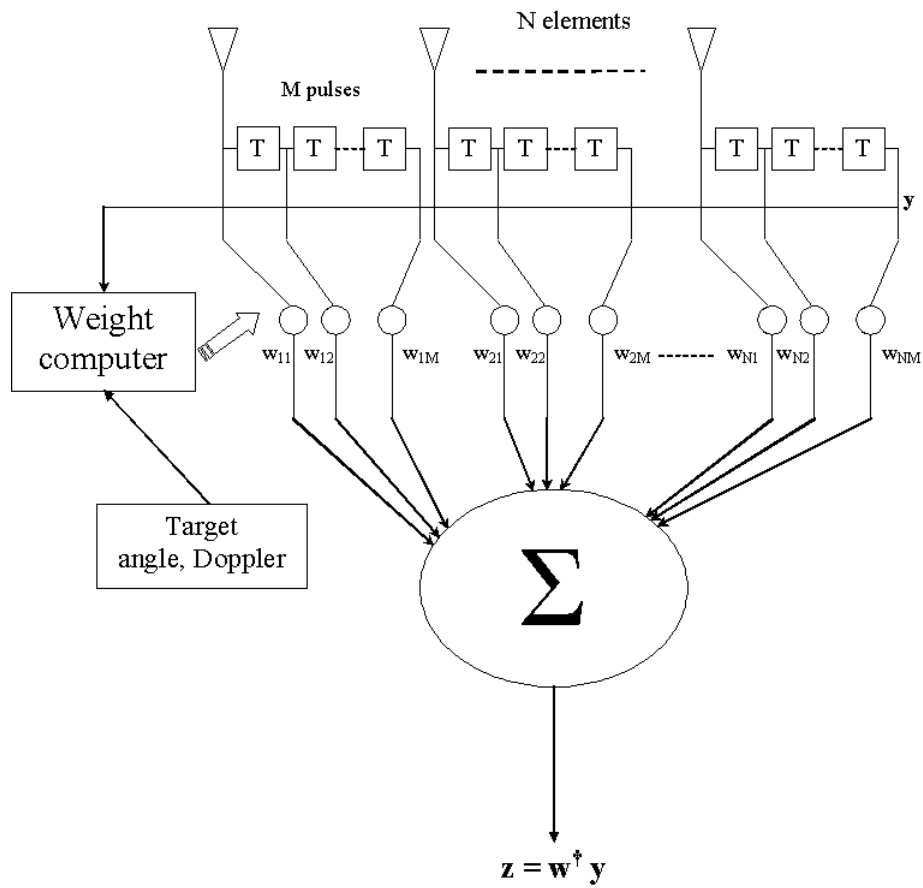


Figure 1.12: Fully adaptive space-time processor.

where  $f(\mathbf{y}|H_1)$  is the probability density function of the data under hypothesis  $H_1$  and  $f(\mathbf{y}|H_0)$  is the probability density function under hypothesis  $H_0$  and  $\gamma$  is the chosen threshold. This criterion ensures the test is *Uniformly Most Powerful*. This criterion is difficult to be applied since it needs the perfect knowledge of all the parameters involved; typically the amplitude of the target return and the interference covariance matrix are unknown. The detection of a signal of known form in the presence of interference, assumed to be Gaussian which covariance matrix is totally unknown, was first discussed by Reed, Brennan and Mallett [25]. In this procedure, the weight vector, determined using the interference covariance matrix estimated from the secondary data, is applied to the primary data in the form of a standard colored noise matched filter. The output of this filter is then compared with a threshold for signal detection but no rule is given for the determination of this threshold, whose value controls the probability of false alarm. In fact, no predetermined threshold can be assigned to achieve a given  $P_{FA}$ , since the detector is supposed to operate in an interference environment of unknown form and intensity. The SINR of the filter output is function of the secondary data and thus it is a random variable. Its pdf has the remarkable property of being independent of the actual noise covariance matrix; it is only a function of the dimensional parameters of the problem. The secondary data would be sufficient in quantity to support a good estimate of the noise covariance and the threshold could be presumably determined from this estimate. The final decision statistic is then more complicated than a matched filter output itself and, being a non-linear function of the secondary data, the detection and false alarm properties are not functions of the SINR alone, leaving the actual performance of the procedure undetermined [8].

A way to circumvent the highlighted problems consists in replacing the ad hoc procedure proposed in [25] by a likelihood ratio test, i.e. maximizing two likelihood functions over a set of unknown parameters. The processor in [25] appears as a portion of the likelihood ratio detection statistic. The first test proposed applying this criterion is the *Generalized Likelihood Ratio Test* (GLRT) [8]. This test exhibits the desirable property that its  $P_{FA}$  is independent of the covariance matrix (level and structure) of the actual noise environment. Furthermore, the effect of signal presence depends only on the dimensional parameters of the problem and a parameter which is the same as the SINR of a conventional colored noise matched filter. Its  $P_{FA}$  depends on threshold exactly in the same way as a simple scalar CFAR problem, in which detection is based on one complex sample and the threshold is propor-

tional to the sum of a number of independent noise samples. Another important approach was proposed in [11]. The GLRT was derived maximizing the likelihood functions over, among the others, the interference covariance matrix. In this second approach, a detection algorithm is derived assuming the interference covariance matrix being known. After the test statistic is derived, the maximum likelihood estimate of this matrix, based on the secondary data, is inserted in place of the known matrix. The resulting test statistic has the form of a normalized matched filter and it is also a CFAR detector. This decision statistic is less computationally intensive of the GLRT. Its performance to signals that are aligned with the steering vector exhibit a small loss when compared with the GLRT detector at low Signal-to-Noise Ratios, but its  $P_D$  is higher than that of the GLRT detector for high SNRs.

In the rest of this section both of these two decision statistics are introduced. They were derived under the ideal conditions of absence of mutual coupling, stationarity of the environment, sufficient number of secondary data for covariance estimate and under far-field conditions.

### 1.2.1 Generalized Likelihood Ratio Test

In this section the GLRT processor by [8] is introduced. The data are assumed being composed by both primary and secondary data, where the target is sought to be present only in the primary data. The secondary ones are composed only by interference which has the same statistical properties of the interference that affects the primary data. The interference is assumed composed only by noise, which total components of data vectors are modeled as zero-mean complex Gaussian random vectors; the noise covariance matrix is unknown. The hypotheses test is the one reported in (1.57), composed by both primary and secondary data. The two probability density functions, under the two hypotheses, are

$$f(\mathbf{y}, \mathbf{y}_1, \dots, \mathbf{y}_{K-1} | H_0) = f(\mathbf{y} | H_0) \prod_{k=0}^{K-1} f(\mathbf{y}_k | H_0) \quad (1.63)$$

under hypothesis  $H_0$  and

$$f(\mathbf{y}, \mathbf{y}_1, \dots, \mathbf{y}_{K-1} | H_1) = f(\mathbf{y} | H_1) \prod_{k=0}^{K-1} f(\mathbf{y}_k | H_1) \quad (1.64)$$

under hypothesis  $H_1$ . The joint probability function of primary and all secondary data is the product of the probability density functions because the data

are assumed uncorrelated from each other. These probability density functions are

$$\begin{aligned}
 f(\mathbf{y}|H_0) &= \frac{1}{\pi^N \det(\mathbf{M})} e^{-\mathbf{y}^\dagger \mathbf{M}^{-1} \mathbf{y}} \\
 f(\mathbf{y}_k|H_0) &= \frac{1}{\pi^N \det(\mathbf{M})} e^{-\mathbf{y}_k^\dagger \mathbf{M}^{-1} \mathbf{y}_k} \\
 f(\mathbf{y}|H_1) &= \frac{1}{\pi^N \det(\mathbf{M})} e^{-(\mathbf{y} - \alpha_t \mathbf{s}_t)^\dagger \mathbf{M}^{-1} (\mathbf{y} - \alpha_t \mathbf{s}_t)} \\
 f(\mathbf{y}_k|H_1) &= \frac{1}{\pi^N \det(\mathbf{M})} e^{-\mathbf{y}_k^\dagger \mathbf{M}^{-1} \mathbf{y}_k}
 \end{aligned} \tag{1.65}$$

where  $\det(\cdot)$  is the determinant of a matrix. Assuming unknown only the interference covariance matrix and the amplitude  $\alpha_t$ , the ratio between the maximization of the likelihood functions is

$$\frac{\max_{\alpha_t, \mathbf{M}} f(\mathbf{y}, \mathbf{y}_1, \dots, \mathbf{y}_{K-1}|H_1)}{\max_{\mathbf{M}} f(\mathbf{y}, \mathbf{y}_1, \dots, \mathbf{y}_{K-1}|H_0)} \underset{H_0}{\overset{H_1}{>}} T', \tag{1.66}$$

from which the final decision statistic is

$$\frac{|\mathbf{s}_t^\dagger \hat{\mathbf{M}}^{-1} \mathbf{y}|^2}{\left[1 + \frac{1}{K} (\mathbf{y}^\dagger \hat{\mathbf{M}}^{-1} \mathbf{y})\right] \mathbf{s}_t^\dagger \hat{\mathbf{M}}^{-1} \mathbf{s}_t} \underset{H_0}{\overset{H_1}{>}} T \tag{1.67}$$

where  $T$  is the threshold derived from the initial one  $T'$ . The secondary data enter this test only through the sample covariance matrix  $\hat{\mathbf{M}}$  and thus through the weight vector  $\hat{\mathbf{w}} = \hat{\mathbf{M}}^{-1} \mathbf{s}_t$ . The processor proposed in [25] by the Reed et al. is just

$$\left| \hat{\mathbf{w}}^\dagger \mathbf{y} \right|^2 \underset{H_0}{\overset{H_1}{>}} T \tag{1.68}$$

which has the form of the colored noise matched filter test, with  $\hat{\mathbf{M}}$  replacing the usual known covariance matrix of the noise. Note that it is the numerator of the decision statistic in (1.67). If the target model is generalized, so that the signal vector still contains one or more unknown parameters (such as target Doppler), the likelihood ratio obtained above must next be maximized over these parameters. This maximization generally cannot be carried out explicitly and the standard technique is to approximate it by evaluating the test statistic

for a discrete set of target parameters, forming a filter bank, and declaring target presence if any filter output exceeds the threshold.

The presence of the signal-dependent factor in the denominator of the expression of the decision statistic causes this detection statistic to be unchanged if the signal vector is altered by a scalar factor. Since the normalization of this vector has been left arbitrary, this invariant is highly desirable. The entire decision statistic is also invariant to a common change of scale of all the input data vectors, a minimal CFAR requirement.

In the limit of very large  $K$ , the estimator  $\hat{\mathbf{M}}$  is expected to converge to the true covariance matrix  $\mathbf{M}$  at least in probability. Moreover, it can be shown that the quantity

$$\mathbf{y}^\dagger \mathbf{M}^{-1} \mathbf{y},$$

an inner product utilizing the actual covariance matrix instead of its estimator, obeys the chi-squared distribution, with  $2N$  degrees of freedom, and hence this term, when divided by  $K$ , converges to zero in probability, when  $K$  grows without bound. In this sense the likelihood ratio test passes over into the conventional colored noise matched filter test, as the number of sample vectors in the secondary data set becomes very large. Furthermore, it can be shown [8] that the pdf of the decision statistic depends on the interference covariance matrix only through the meaning of the signal amplitude parameter  $\alpha_t$ . In fact, this pdf can depend only on  $\alpha_t$ ,  $N$  and  $K$  and hence the false alarm probability of the likelihood ratio detector is independent of  $\mathbf{M}$  and this is the generalized CFAR property.

The performance of the likelihood ratio test depends only on the dimensional integers  $N$  and  $K$  and a SINR parameter which is function of the true signal strength and the intensity and character of the actual noise and interference. The ability of a system to function effectively in interference depends principally on the arrangements which have been made in its design to achieve a good colored noise matched filter SINR in its intended environment. These arrangements will usually take the form of diversity of RF inputs in one form or another. The important requirement is the need to have inputs available from which the actual noise characteristics can be estimated implies performance degradation in comparison to a detector which knows the interference covariance matrix in advance; the decay is in term of major SINR to achieve the same  $P_D$  at the same  $P_{FA}$ . This difference is the penalty for having estimate the interference covariance matrix and it vary sharply with the number  $K$  of available secondary data. This penalty has two effects, one due to the CFAR character of the decision rule and the other to the effective SINR loss

factor. The first decreases as the value of  $K$  increases, while the second is function roughly of the ratio of  $K$  to  $N$ . The *SINR loss factor* measures the performance of a detector relative to what can be achieved with an optimum detector for the case of interest. It is defined by

$$L_{SINR} = \frac{SINR_a}{SINR_0} \quad (1.69)$$

where  $SINR_a$  is the Signal-to-Interference-plus-Noise Ratio achievable with the actual detector and  $SINR_0$  the one achievable using the optimum detector. For example, in this case the optimum detector knows exactly the interference covariance matrix and thus the SINR loss factor measures the penalty due to the estimation of that matrix.

### 1.2.2 Adaptive Matched Filter

In a well known paper [11], another detector, that exploits the secondary data to estimate the interference covariance matrix, was derived. It is known as *Adaptive Matched Filter* and is very similar to the GLRT derived in [8]. It is based on the GLRT assuming the covariance matrix is known. After the test is derived, the maximum likelihood estimate of the interference covariance matrix based on the secondary data is inserted in place of the known covariance. The resulting test statistic has the form of a normalized matched filter and it is also a CFAR detector, but it is less computationally intensive than the GLRT.

The signal model is assumed to be the same as the GLRT, thus the probability density functions are those reported in (1.65). The procedure used to derive the test statistic is to assume that the covariance matrix is known and then to write the GLRT maximizing over the unknown amplitude of the target return

$$\frac{\max_{\alpha_t} f(\mathbf{y}, \mathbf{y}_1, \dots, \mathbf{y}_{K-1} | H_1)}{f(\mathbf{y}, \mathbf{y}_1, \dots, \mathbf{y}_{K-1} | H_0)} \underset{H_0}{\overset{H_1}{>}} T'' \quad (1.70)$$

The test statistic developed from this ratio is

$$\frac{|\mathbf{s}_t^\dagger \mathbf{M}^{-1} \mathbf{y}|^2}{\mathbf{s}_t^\dagger \mathbf{M}^{-1} \mathbf{s}_t} \underset{H_0}{\overset{H_1}{>}} \gamma \quad (1.71)$$

where  $\gamma$  is a transformation of the initial threshold  $T''$ . This test statistic is proportional to the squared magnitude of the output of the colored noise linear

matched filter, since the term in the denominator is a constant when the true covariance is known. The covariance matrix in general is unknown and the solution proposed in [11] is to account for not knowing the true covariance by the ad hoc procedure of substituting the maximum likelihood estimate based on secondary data. The test statistic becomes

$$\frac{\left| \mathbf{s}_t^\dagger \hat{\mathbf{M}}^{-1} \mathbf{y} \right|^2}{\mathbf{s}_t^\dagger \hat{\mathbf{M}}^{-1} \mathbf{s}_t} \underset{H_0}{\overset{H_1}{>}} \gamma. \quad (1.72)$$

Its numerator is the test statistic proposed in [25], as well as in the GLRT. The normalization is the same provided by the GLRT for a very large number of secondary data. This normalization provides the CFAR behavior of the statistic. The only difference between the GLRT and the AMF is the term

$$1 + \frac{1}{K} \left( \mathbf{y}^\dagger \hat{\mathbf{M}}^{-1} \mathbf{y} \right)$$

which is present in the normalization term of the GLRT. This term is computationally intensive and thus its absence makes less intensive the AMF than the GLRT. However, the GLRT uses all the data (primary and secondary) in the likelihood maximization under each hypothesis. The AMF test makes no use of the primary data vector to estimate the covariance, therefore poorer detection performance might be expected. The GLRT shows, in general, better performance than the AMF at low SINR, while this advantage decreases at increasing the SINR; furthermore, for signals aligned to the steering vector there is a crossover at high SINR, where the AMF shows better performance than the GLRT [11]. Under mismatched conditions, the behavior is slightly different; in fact, the GLRT shows better performance for very low SINRs and the crossover is seen to occur at lower SINRs than that under matched conditions. For very low SINRs there is no practical difference between the two receivers. This implies a lowering of the  $P_D$  sidelobes of the GLRT detector at high SINR levels compared with the AMF detector. There is a significant difference in sidelobe performance for these two detectors. However, the GLRT detector is superior in rejecting mismatched signals. The performance considered are measured in terms of  $P_D$  versus SINR.

The difference in the  $P_D$  at high SINR levels is explained by analyzing the test statistics [11]. Let  $\cos^2 \vartheta$  be the measure of the mismatch between the nominal steering vector and the actual one; it is  $\cos^2 \vartheta = 1$  under matched conditions and  $\cos^2 \vartheta < 1$  under mismatched conditions. Assuming that the

true interference covariance matrix is the identity matrix  $\mathbf{I}$ , the statistics take respectively the forms

**GLRT :**

$$\frac{|\mathbf{y}|^2}{\left[1 + \frac{1}{K}|\mathbf{y}|^2\right]} \underset{H_0}{\overset{H_1}{>}} \frac{\gamma}{\cos^2 \vartheta} \quad (1.73)$$

**AMF :**

$$|\mathbf{y}|^2 \underset{H_0}{\overset{H_1}{>}} \frac{\gamma}{\cos^2 \vartheta}. \quad (1.74)$$

The left-hand side for the GLRT test approaches an asymptote at high SINRs, while for the AMF test the same quantity is unbounded. The GLRT has then a maximum separation that allows detection at a given threshold, while the AMF test allows large signals that are nearly orthogonal to the steering direction to be detected.

## Chapter 2

# Bistatic Radars

As reported in the introduction, the bistatic radar is composed by transmitter and receiver that are not co-located. A widely used coordinate system is a two-dimensional, North-referenced coordinate system [81]; the choice of this system is because of its convenience in developing equations for bistatic geometry. Fig. 2.1 shows the coordinate system and parameters defining bistatic radar operation in the plane containing the transmitter ( $T_X$ ), the receiver ( $R_X$ ) and the target;  $N_{th}$  denotes the North. It is called the *bistatic plane* [82]. The bistatic triangle lies in the bistatic plane. The distance  $L$  between the transmitter and the receiver is called *baseline range* or simply *baseline*. The extended baseline is defined as continuing beyond either the transmitter or the receiver. The angles  $\theta_T$  and  $\theta_R$  are, respectively, the transmitter and the receiver *look angles*, which are taken as positive when measured clockwise from the North. They are also called *angles of arrival* (AOA) or *lines of sight* (LOS). The bistatic angle  $\beta$  is the angle between the transmitter and the receiver with the vertex at the target. Note that  $\beta = \theta_T - \theta_R$ . When the target lies above the baseline (and the extended baseline), such that  $-90^\circ < \theta_T < +90^\circ$  and  $-90^\circ < \theta_R < +90^\circ$ , it is said to be in the “northern hemisphere”; the “southern hemisphere” is similarly defined for targets lying below the baseline. In general, bistatic radar operation and performance in the northern and southern hemispheres are equivalent for symmetric geometries. Obvious exceptions include limited scan capabilities for the transmitting or receiving antennas, terrain masking and variations in bistatic RCS of a target as it moves from one hemisphere to the other [4].

A bistatic radar usually measures target range as the range sum ( $R_T + R_R$ ), where  $R_T$  is the transmitter-to-target range and  $R_R$  is the receiver-to-target

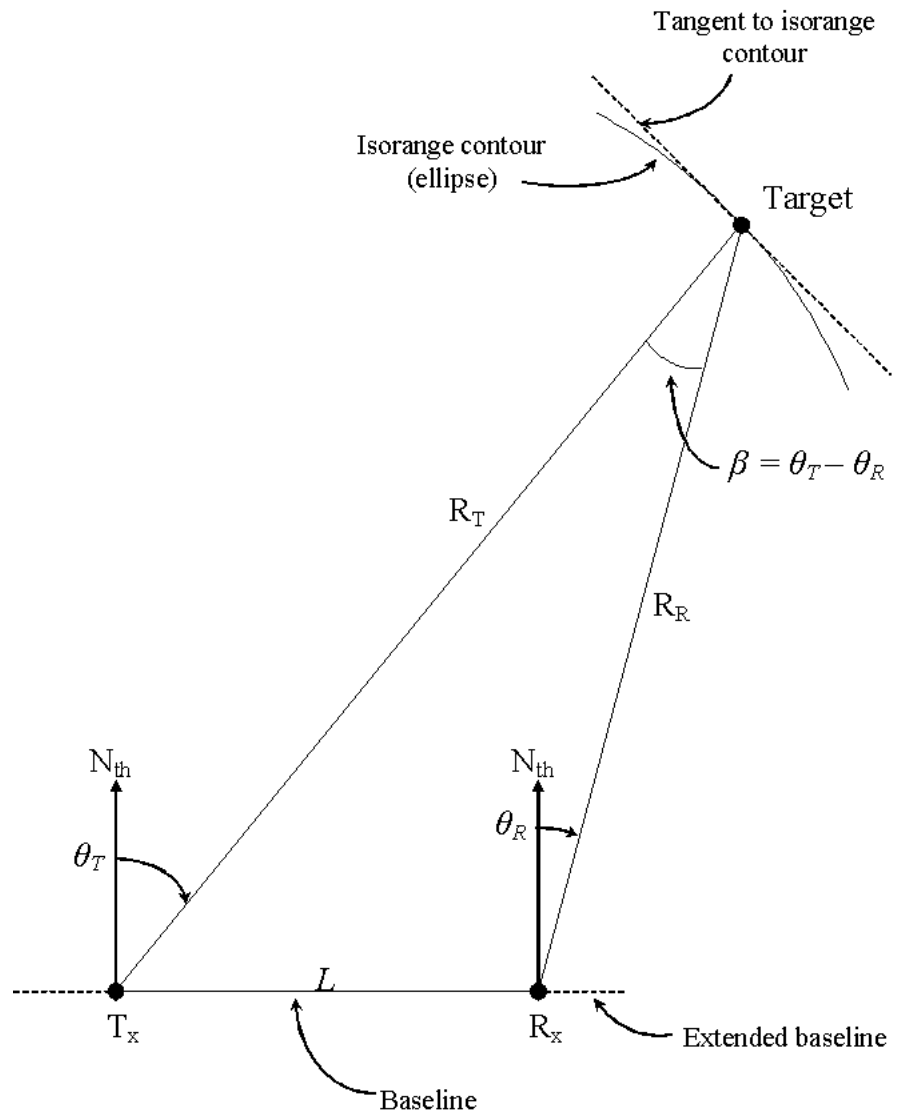


**Figure 2.1:** Bistatic radar North-referenced coordinate system in two dimensions.

range. A contour of constant range sum, or *isorange contour*, is described by an ellipse, which is defined as the locus of points in which the sum of the distances from two fixed points is constant. When the two fixed points are the transmitter and the receiver sites, the isorange contour is

$$R_T + R_R = 2a, \quad (2.1)$$

where  $a$  is the semimajor axis of the ellipse. In the monostatic case, transmitter and receiver are co-located, i.e.  $R_T = R_R$ , and thus its isorange contour is a circle of radius  $a$ , the limiting case for a bistatic isorange contour. The semiminor axis of the isorange contour ellipse is

$$b = \sqrt{a^2 - \frac{L^2}{4}} \quad (2.2)$$

and thus, all ellipses having common transmitting and receiving site foci (i.e. common baseline) are concentric by definition and satisfy the relationship

$$a_i^2 - b_i^2 = \frac{L^2}{4} \quad (2.3)$$

where the subscript  $i$  defines axes for each concentric ellipse. Fig. 2.2 shows some concentric isorange contours. The bisector of the bistatic angle is orthogonal to the tangent of the isorange contour at any point on the bistatic isorange contour. The bistatic angle is maximum when its bisector is also the perpendicular bisector of the baseline. This bisector is also the minor axis of the ellipse. In this case  $\theta_T = \theta_R$  and  $R_T = R_R$  and thus

$$\beta_{\max} = 2 \arcsin\left(\frac{L}{2R_T}\right) = 2 \arcsin\left(\frac{L}{2R_R}\right) \quad (2.4)$$

while in general the bistatic angle is

$$\beta = \arcsin\left(\frac{L \cos \theta_T}{R_T}\right) = \arcsin\left(\frac{L \cos \theta_R}{R_R}\right). \quad (2.5)$$

In geometries where the target is near to the baseline, the maximum bistatic angle  $\beta_{\max}$  can approach  $180^\circ$ , with  $\beta = 180^\circ$  occurring when the target crosses the baseline at any point. Defining the *eccentricity* of the ellipse as

$$e = \frac{L}{R_T + R_R} = \frac{L}{2a} \quad (2.6)$$

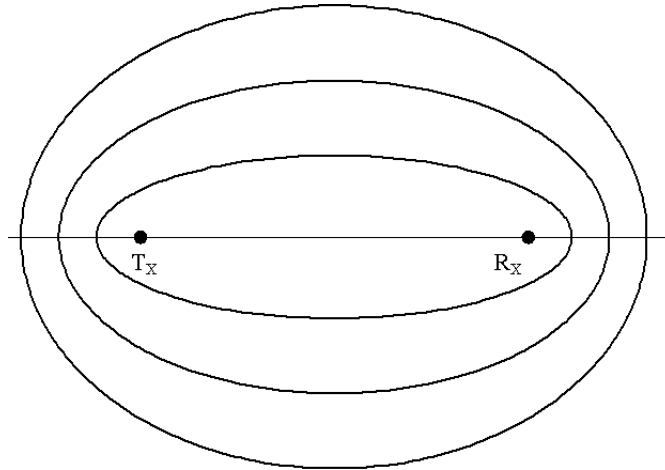


**Figure 2.2:** Concentric isorange contours: transmitter and receiver are the common foci of the ellipses.

which is  $0 \leq e \leq 1$  due to the relation between the baseline and the semimajor axis of the ellipse (i.e.  $L \leq 2a$ ), it can be shown that

$$\beta_{\max} = 2 \arcsin e. \quad (2.7)$$

When  $\beta_{\max} \geq 140^\circ$  and consequently  $e \geq 0.95$ , many approximations used in estimating bistatic radar performance break down, like for example for the approximation about the bistatic range cell

$$\Delta R_B \approx \frac{c\tau}{2} \cos\left(\frac{\beta}{2}\right), \quad (2.8)$$

where  $\tau$  is the compressed pulsewidth.

Geometry often distinguishes bistatic from monostatic operation. In these distinguishing cases, equivalent, or corresponding, monostatic operation is defined when the monostatic radar is positioned on the bisector of the bistatic angle [4]. For this geometry bistatic operation is often related to equivalent monostatic operation by the factor  $\cos(\beta/2)$ . For example, bistatic target Doppler is reduced by  $\cos(\beta/2)$  compared to equivalent monostatic Doppler; the bistatic range cell, along with range, isorange range (synthetic aperture), velocity and angle resolution is increased (i.e. degraded) by  $\cos(\beta/2)$  compared to equivalent monostatic range cell and resolution; the bistatic RCS

of complex target is equal to the monostatic RCS reduced in frequency by  $\cos(\beta/2)$  when  $\beta$  is small. Bistatic operation collapses to monostatic operation by setting  $L = 0$  or  $R_T = R_R$  and  $\beta = 0$  in bistatic equations.

## 2.1 Bistatic radar range equation

The range equation [34, 35, 36] for a bistatic radar is similar to the one for monostatic radar; the *bistatic radar maximum range equation* can be written as

$$(R_T R_R)_{\max} = \sqrt{\frac{P_T G_T G_R \lambda^2 \sigma_B F_T^2 F_R^2}{(4\pi)^3 k T_s B_n (S/N)_{\min} L_T L_R}} \quad (2.9)$$

or equivalently

$$(R_T R_R)_{\max} = R_{MB}. \quad (2.10)$$

The meaning of these symbols is reported in the table 2.1. The interested

Symbol	Meaning
$R_T$	transmitter-to-target range
$R_R$	receiver-to-target range
$P_T$	transmitter power output
$G_T$	transmitting antenna power gain
$G_R$	receiving antenna power gain
$\lambda$	wavelength
$\sigma_B$	bistatic radar target cross section
$F_T$	pattern propagation factor for transmitter-to-target path
$F_R$	pattern propagation factor for target-to-receiver path
$k$	Boltzmann's constant
$T_s$	receiving system noise temperature
$B_n$	noise bandwidth of receiver's predetection filter, sufficient to pass all spectral components of the transmitted signal
$(S/N)_{\min}$	signal-to-noise power ratio required for detection
$L_T$	transmitting system loss ( $> 1$ ) not included in other parameters
$L_R$	receiving system loss ( $> 1$ ) not included in other parameters
$R_{MB}$	bistatic maximum range product

**Table 2.1:** Parameters in the bistatic radar range equation.

reader is referred to the literature for more information about the quoted parameters [19, 37, 38]. Equation (2.9) is simply related to the corresponding

equation for monostatic radars with the following substitutions:

$$\sigma_M = \sigma_B \quad (2.11)$$

$$L_M^2 = L_T L_R \quad (2.12)$$

$$R_M^4 = R_T^2 R_R^2 \quad (2.13)$$

where  $\sigma_M$  is the monostatic radar target cross section,  $L_M$  is the monostatic system loss not included in other parameters and  $R_M$  is the monostatic transmitter-and-receiver-to-target range. Similarly, equation (2.10) is related to the corresponding monostatic maximum range equation by

$$(R_M)_{\max} = \sqrt{R_{MB}} \quad (2.14)$$

where the term  $\sqrt{R_{MB}}$  is sometimes called the *equivalent monostatic range*, which occurs when transmitting and receiving sites are co-located [39].

These simple differences cause significant differences in monostatic and bistatic radar operations. The first major difference is that bistatic thermal noise-limited detection contours are defined by ovals of Cassini, rather than by circles for the simplest monostatic case. These ovals are very useful in defining regions where the bistatic radar can operate. A second difference is that bistatic constant range sum contours, the isorange contours previously defined, are not colinear with the bistatic constant detection contours, defined by the ovals of Cassini, whereas for the monostatic case they are colinear circles. This difference sets operating limits for the bistatic radar, and also causes the target's SNR to vary as a function of its position on a constant range sum contour, unlike the monostatic case. A third difference is that the width of a bistatic range cell changes as a function of the target's position as a constant range sum contour, or ellipse, whereas it is a constant value for the monostatic case. A fourth difference is that the bistatic transmitting and receiving pattern propagation factors,  $F_T$  and  $F_R$  respectively, can be significantly different, whereas they are usually identical for the monostatic case, and only deviate when the monostatic radar employs separate transmitting and receiving antenna patterns or operates in a non-reciprocal propagation medium.

Equation (2.9) applies for all types of waveforms, like amplitude-modulated (AM), frequency-modulated (FM) or pulsed. More specific formulations of the maximum range equation, as give in [19], also apply to the bistatic radar case.

## 2.2 Ovals of Cassini

The formal definition of an oval of Cassini is the locus of the vertex of a triangle when the product of the sides adjacent to the vertex is constant and the length of the opposite side is fixed [40]. When applied to the bistatic triangle of Fig. 2.1, the vertex is at the target site,  $R_T$  and  $R_R$  are the sides adjacent to the vertex and the baseline  $L$  is the length of the fixed, opposite side. Thus, for specific transmitting and receiving sites, which establish  $L$ , and for a constant bistatic maximum range product  $R_{MB}$ , (2.10) is the expression for a bistatic maximum range oval of Cassini. It is instructive to plot ovals of Cassini as a function of available signal-to-noise power ratio ( $S/N$ ), rather than just the ratio required for detection,  $(S/N)_{\min}$ . In this case (2.9) and (2.10) are modified simply dropping the “max” and “min” designation for  $(R_T R_R)$  and  $(S/N)$  respectively and solving for  $(S/N)$

$$(S/N) = \frac{K_B}{R_T^2 R_R^2} \quad (2.15)$$

where  $S/N$  is the signal-to-noise power ratio at range  $R_T$  and  $R_R$  and

$$K_B = \frac{P_T G_T G_R \lambda^2 \sigma_B^2 F_T^2 F_R^2}{(4\pi)^3 k T_s B_n L_T L_R} \quad (2.16)$$

is the *bistatic radar constant*, related to the bistatic maximum range product  $R_{MB}$  as follows

$$K_B = R_{MB}^2 (S/N)_{\min}. \quad (2.17)$$

To plot the ovals of Cassini is useful to use the polar coordinate  $(r_p, \theta_p)$  system, as shown in Fig. 2.3. Converting  $R_T$  and  $R_R$  to polar coordinates yields

$$R_R^2 = \left( r_p^2 + \frac{L^2}{4} \right) - r_p L \cos \theta_p \quad (2.18)$$

$$R_T^2 = \left( r_p^2 + \frac{L^2}{4} \right) + r_p L \cos \theta_p \quad (2.19)$$

$$R_T^2 R_R^2 = \left( r_p^2 + \frac{L^2}{4} \right)^2 - r_p^2 L^2 \cos^2 \theta_p. \quad (2.20)$$

Thus the signal-to-noise power ratio becomes

$$(S/N) = \frac{K_B}{\left( r_p^2 + \frac{L^2}{4} \right)^2 - r_p^2 L^2 \cos^2 \theta_p}. \quad (2.21)$$

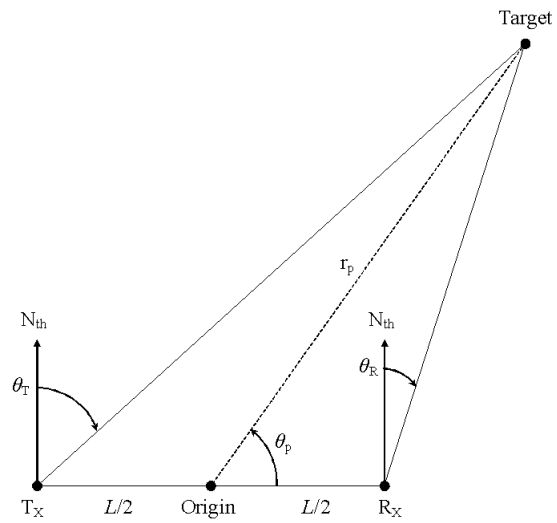


**Figure 2.3:** Geometry for converting North-referenced coordinates into polar coordinates  $(r_p, \theta_p)$ .

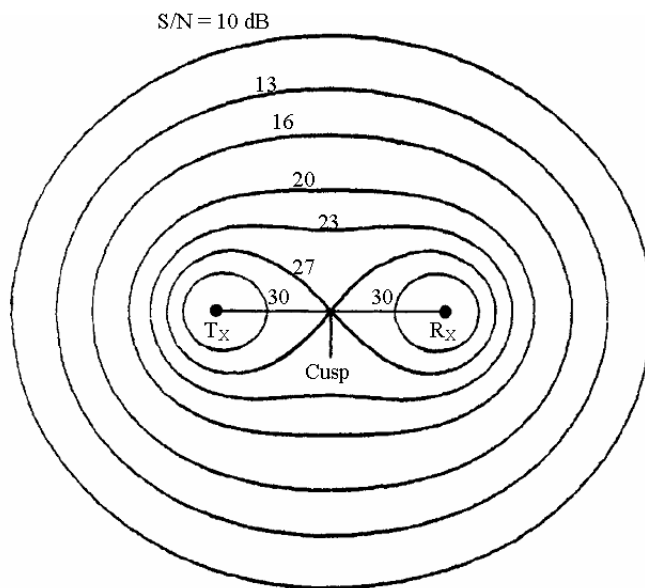


**Figure 2.4:** Contours of a constant SNR - ovals of Cassini, with  $K = 30L^2$ .

Equation (2.21) is plotted in Fig. 2.4 for  $10\text{dB} \leq (S/N) \leq 30\text{dB}$  and  $K_B$  arbitrarily set to  $30L^4$ .

The ovals of Cassini are contours of a constant SNR on a bistatic plane. They assume that an adequate LOS exists on the transmitter-to-target range and receiver-to-target range and that  $\sigma_B$ ,  $F_T$  and  $F_R$  are invariant with  $r_p$  and  $\theta_p$ , which is usually not the case. However, the simplifying assumption is useful in understanding basic relationships and constraints. As  $(S/N)$  increases the ovals shrink, finally collapsing around the transmitting and receiving sites. The point on the baseline where the oval breaks into two parts is called the *cusp*. The oval is called a *lemniscate* (of two parts) at this  $(S/N)$ . At this point,  $r_p = 0$  and from equation (2.21)

$$(S/N) = 16 \frac{K_B}{L^4}. \quad (2.22)$$

Using equation (2.17) in the last one and assuming that  $(S/N) = (S/N)_{\min}$  for this lemniscate, (2.22) yields to

$$L = 2\sqrt{R_{MB}}. \quad (2.23)$$

A maximum range oval of Cassini breaks into two parts when  $L > 2\sqrt{R_{MB}}$ . It remains a single oval for  $L < 2\sqrt{R_{MB}}$  and is a lemniscate for  $L = 2\sqrt{R_{MB}}$ . When  $L = 0$  and  $R_T R_R = r_p^2$ , i.e. in the monostatic case, the ovals become circles of radius  $r_p$ .

The ovals of Cassini define three distinct operating regions for a bistatic radar:

1. *receiver-centered region*: it occurs when  $L > 2\sqrt{R_{MB}}$  and  $R_T \gg R_R$ . Some examples of operating scenarios are (1) air-to-ground operations using a standoff transmitter and a penetrating aircraft with a silent receiver; (2) short-range ground-based air defense or ground surveillance again with a standoff transmitter, sometimes called *over-the-shoulder operation*; (3) obtaining an indication of target activity near to an airborne receiving platform, which is also called *passive situation awareness*.
2. *transmitter-centered region*: it occurs when  $L > 2\sqrt{R_{MB}}$  and  $R_R \gg R_T$ . Some operative scenarios are (1) monitoring of activity near noncooperative transmitter; (2) alerting of a missile launch from hostile platform that illuminates the missile with its own (noncooperative) transmitter; (3) passive situation awareness can also use a noncooperative transmitter.

3. *cosite region*: it occurs when  $L < 2\sqrt{R_{MB}}$ . Example of operating scenarios are (1) medium-range air defense; (2) satellite tracking from ground-based sites; (3) “tripware” forward-scatter fences for detection of ground targets or introducing aircraft.

Critical to the selection of these operating regions is the value of the bistatic radar constant  $K_B$ , that is available in a given scenario. Many of the terms in (2.17) are transmitter-controlled. Three transmitter configurations often control the operating regions:

1. dedicated transmitter, defined as being under both design and operational control of the bistatic radar system;
2. cooperative transmitter, designed for other functions but found suitable to support bistatic operations and can be controlled to do so;
3. noncooperative transmitter, defined as being suitable for bistatic operations, but not under control, when, for example, it is a neutral transmitter.

### 2.3 Bistatic plane and range cells

The transmitter-to-target-to-receiver range measured by a bistatic radar is the sum  $R_T + R_R = 2a$ . This sum locates the target somewhere on the surface of an ellipsoid, the foci of which are the transmitter and the receiver, separated by the baseline  $L$  and with major axis of  $2a$ . The ellipsoid is completely defined by two parameters,  $L$  and  $a$ , and is the *isorange ellipsoid* of constant range sum  $2a$ . A third measure, usually orthogonal AOAs, for example, azimuth and elevation angles, is required to locate a target on the isorange ellipsoid. With the target position established, the *bistatic plane* is defined by the baseline and the target position. The intersection of the bistatic plane with the isorange ellipsoid produces an ellipse of constant range, the previously introduced isorange contour. The isorange contour is coplanar but not colinear with the corresponding oval of Cassini passing through the target position, the  $(S/N)$  changes for different target positions on the isorange contour. In the monostatic case, the isorange ellipsoid corresponds to a sphere of radius  $r_p$ . In this case any plane containing the target position and the antenna location intersects the sphere to produce circles of constant range, the monostatic isorange contour. The analogy is not exact, because an infinite number of isorange contour exist for each target position, whereas only one bistatic isorange contour exists for each target position.

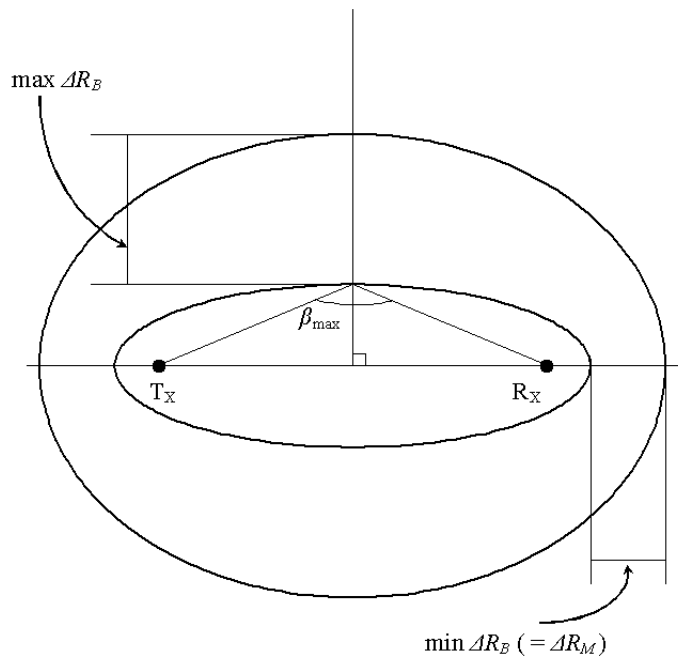


**Figure 2.5:** Maximum and minimum bistatic range cells.

The separation  $\Delta R_M$  between two concentric monostatic isorange contours establishes the width of a monostatic range cell and is

$$\Delta R_M = \frac{c\tau}{2} \quad (2.24)$$

where  $c$  is the speed of light and  $\tau$  the compressed pulsewidth. Similarly, the width of a bistatic range cell is defined as the separation  $\Delta R_B$  between two concentric isorange contours. This separation varies depending on the target position; the minimum separation is on the extended baseline and the maximum separation is on the perpendicular bisector of the baseline, in correspondence of  $\beta_{\max}$ , as shown in Fig. 2.5. Consider two confocal ellipses defined by their semimajor axes

$$R_T + R_R = 2a \quad (2.25)$$

$$R'_T + R'_R = 2a' \quad (2.26)$$

with  $a' > a$ ; both have foci in the transmitting and receiving sites with baseline  $L$ . The separation between these two isorange contours is measured along the

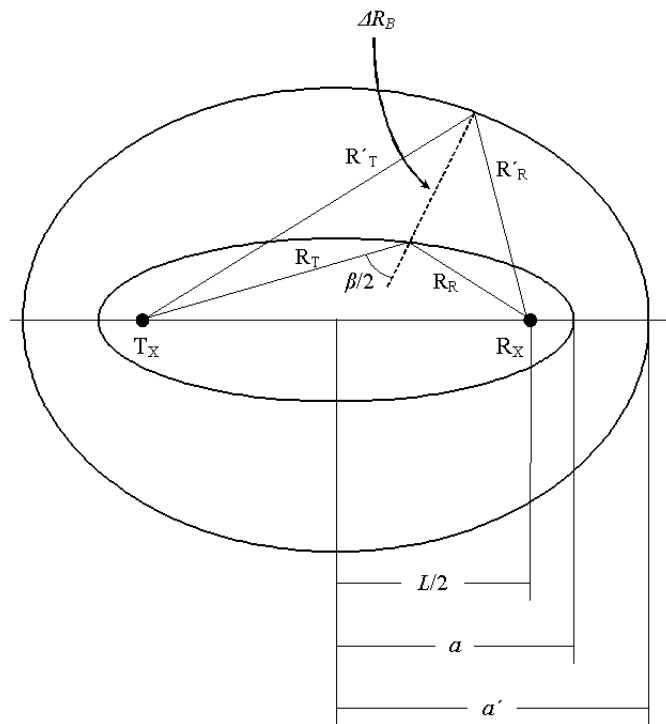


**Figure 2.6:** Geometry for bistatic range cell separation.

bisector of the bistatic angle  $\beta$  on the inner ellipse, as shown in Fig. 2.6. The pseudomonostatic range cell  $\Delta R_M$  is defined as the separation between two concentric circles

$$\Delta R_M = a' - a. \quad (2.27)$$

An approximation to the bistatic range cells separation is

$$\Delta R_B \approx \frac{\Delta R_M}{\cos(\beta/2)} = \frac{c\tau}{2 \cos(\beta/2)}. \quad (2.28)$$

The maximum error due to this approximation is in correspondence of the maximum bistatic angle  $\beta_{\max}$  and is [4]

$$\epsilon_{\max} = \frac{a(a' - a)}{b(b' - b)} - 1 \quad (2.29)$$

where  $b'$  is the semiminor axis of the outer ellipse. It has been shown [4] that the maximum error is positive and thus the approximated separation is greater than the exact one for all  $\beta$ ; it is equal to the exact one on the extended baseline, where  $\beta = 0$ . So, the expression (2.28) is an upper bound to the bistatic range cell.

## 2.4 Target location

Target position from the receiving site is usually required in bistatic radar. The receiver-to-target range  $R_R$  cannot be measured directly, but calculated by the receiver by solving the bistatic triangle of Fig. 2.1. In the monostatic case, as reported in chapter 1, this distance is directly measurable starting from the round trip delay  $R_t = (c\tau_t)/2$ . A typical solution [36] in the North-referenced coordinate system is

$$R_R = \frac{(R_T + R_R)^2 - L^2}{2(R_T + R_R + L \sin \theta_R)} \quad (2.30)$$

that first requires establishing transmitter location with respect to the receiver. Transmitter coordinates can be sent to the receiver by a dedicated or cooperative transmitter. Alternatively, transmitter location can be estimated by an emitter location system, usually co-located with the receiver. The receiver then establishes the transmitter-receiver baseline range  $L$  and establishes the North-referenced coordinate system. The receiver look angle  $\theta_R$  is either measured directly or target azimuth and elevation measurements are converted to  $\theta_R$ .

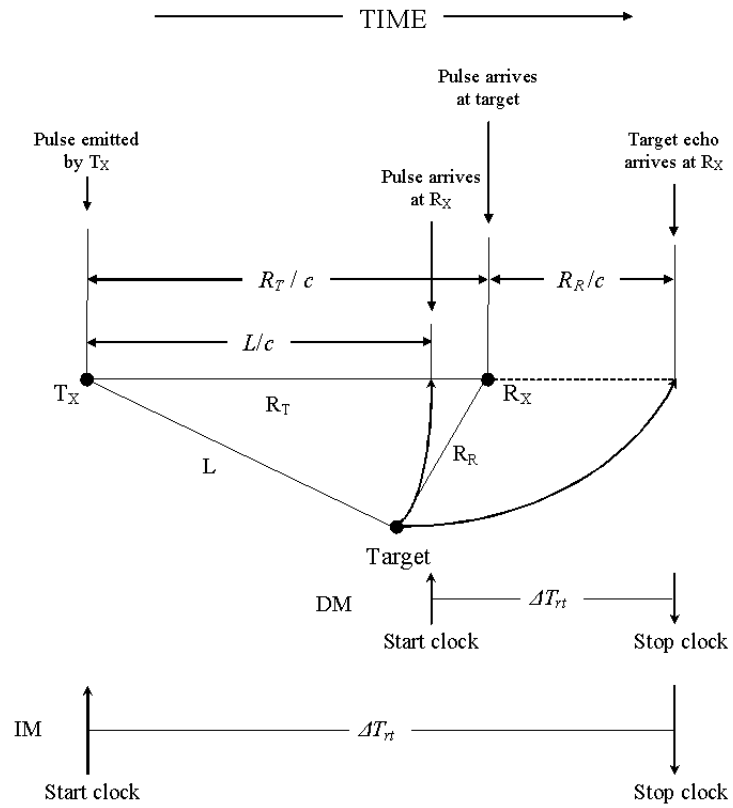


**Figure 2.7:** Timing diagram for direct (DM) and indirect (IM) method of calculating range sum  $R_T + R_R$ .

The range sum ( $R_T + R_R$ ) can be estimated by two methods, using the timing sequence shown in Fig. 2.7. In the *direct method* (DM) the receiver measures the time interval  $\Delta T_{rt}$  between reception of the transmitted pulse and reception of the target echo. The range sum is

$$R_T + R_R = c\Delta T_{rt} + L. \quad (2.31)$$

This method can be used with any transmitter configuration, given an adequate LOS between transmitter and receiver. In the *indirect method* (IM) synchronized stable clocks are used by the receiver and a dedicated transmitter. The receiver measures the time interval  $\Delta T_{rt}$  between transmission of the pulse and reception of the target echo and the range sum is

$$R_T + R_R = c\Delta T_{rt}. \quad (2.32)$$

A transmitter-to-receiver LOS is not required for this measurement. However, a LOS will be required if periodic clock synchronization is implemented over the direct path or the receiver is required to measure the baseline directly.

Equation (2.30), for both the direct and indirect method, is valid for all target locations, except when the target lies on the baseline, between the transmitter and receiver. In this case

$$R_T + R_R = L, \quad \theta_R = -90^\circ \quad (2.33)$$

and  $R_R$  is indeterminate. The transmitted pulse and the target echo arrive simultaneously at the receiver and  $R_R$  cannot be measured [4].

For the special case of bistatic radar using the direct range sum estimation method in which the range sum ( $R_T + R_R$ ) is only slightly greater than the baseline  $L$ , the (2.30) can be approximated as

$$R_R \approx \frac{c\Delta T_{rt}}{1 + \sin \theta_R} \quad (2.34)$$

that does not require the estimation of the baseline  $L$ , but needs the estimation of the transmitter's angular position with respect to the receiver in order to measure  $\theta_R$ . A simple variant of equation (2.30) is based on the use of the bistatic transmitter look angle  $\theta_T$  in place of  $\theta_R$  [41]. In the same way of equation (2.30), using either  $\theta_T$  and  $\theta_R$ , it is possible to calculate the transmitter-to-target range  $R_T$ .

Many other methods are possible to measure the target position [35, 42, 43, 44, 45]; Doppler-only measurements can be used. Because of symmetry,

using only Doppler measurements, a target trajectory cannot be distinguished from its mirror image about a vertical plane that bisects the baseline. In [46] the calculation is based on one transmitter and five receivers; the system operates coherently between each transmitting-receiving pair, but non-coherently between receiving sites.

Finally, a so called “theta-theta” location technique uses the angles  $\theta_T$  and  $\theta_R$  and an estimate of  $L$ , where  $\theta_T$  is typically provided by a monostatic radar, which acts as a cooperative bistatic transmitter, using equation

$$R_R = \frac{L \cos \theta_T}{\sin(\theta_T - \theta_R)}. \quad (2.35)$$

One variant of this technique uses measurements from two receiving sites in a multistatic configuration. A second variant [4] uses the angles  $\theta_T$  and  $\theta_R$  and a measure of  $\Delta T_{rt}$

$$R_R = \frac{c \Delta T_{rt} \cos \theta_T}{\cos \theta_T + \cos \theta_R - \sin(\theta_T - \theta_R)}. \quad (2.36)$$

## 2.5 STAP for bistatic radars

Consider a general case of receiving system with  $Q$  spatial channels. The signal received by each spatial channel could be come from an element, a subarray or a beam. The outputs of all channels are assumed being complex baseband digital signals corresponding to a single range resolution cell (after pulses compression). The output for the  $q^{th}$  channel is

$$y_{mq}, \quad m = 0, \dots, M - 1 \quad (2.37)$$

where  $M$  denotes the number of the pulses in a CPI. The signal received at the  $q^{th}$  channel due to target, jamming, clutter and noise can be expressed as the sum of the corresponding term

$$y_{mq} = \alpha_t s_{tmq} + j_{mq} + c_{mq} + n_{mq}, \quad m = 0, \dots, M - 1. \quad (2.38)$$

Each component is assumed independent from the others. The equation can be expressed in vector form as

$$\mathbf{y} = \alpha_t \mathbf{s}_t + \mathbf{j} + \mathbf{c} + \mathbf{n} \quad (2.39)$$

where

$$\begin{aligned}
 \mathbf{y} = \begin{bmatrix} y_{00} \\ y_{01} \\ \vdots \\ y_{0(Q-1)} \\ y_{10} \\ \vdots \\ y_{(M-1)(Q-1)} \end{bmatrix}, \mathbf{s}_t = \begin{bmatrix} s_{t00} \\ s_{t01} \\ \vdots \\ s_{t0(Q-1)} \\ s_{t10} \\ \vdots \\ s_{t(M-1)(Q-1)} \end{bmatrix}, \mathbf{j} = \begin{bmatrix} j_{00} \\ j_{01} \\ \vdots \\ j_{0(Q-1)} \\ j_{10} \\ \vdots \\ j_{(M-1)(Q-1)} \end{bmatrix}, \\
 \mathbf{c} = \begin{bmatrix} c_{00} \\ c_{01} \\ \vdots \\ c_{0(Q-1)} \\ c_{10} \\ \vdots \\ c_{(M-1)(Q-1)} \end{bmatrix}, \mathbf{n} = \begin{bmatrix} n_{00} \\ n_{01} \\ \vdots \\ n_{0(Q-1)} \\ n_{10} \\ \vdots \\ n_{(M-1)(Q-1)} \end{bmatrix}, \tag{2.40}
 \end{aligned}$$

are the vectors composed by all the contributes for the  $Q$  spatial channels and the  $M$  pulses. Starting from these vectors, the hypothesis test can be written as

$$\left\{ \begin{array}{l} H_0 : \begin{cases} \mathbf{y} = \mathbf{j} + \mathbf{c} + \mathbf{n} \\ \mathbf{y}_k = \mathbf{j}_k + \mathbf{c}_k + \mathbf{n}_k \quad k = 0, \dots, K-1 \end{cases} \\ H_1 : \begin{cases} \mathbf{y} = \alpha_t \mathbf{s}_t + \mathbf{j} + \mathbf{c} + \mathbf{n} \\ \mathbf{y}_k = \mathbf{j}_k + \mathbf{c}_k + \mathbf{n}_k \quad k = 0, \dots, K-1 \end{cases} \end{array} \right. . \tag{2.41}$$

With an analogous analysis to that reported in chapter 1, the optimum weight vector is estimated by

$$\hat{\mathbf{w}} = \hat{\mathbf{M}}^{-1} \mathbf{s}_t \tag{2.42}$$

where  $\hat{\mathbf{M}}$  is the interference covariance matrix estimated from the secondary data.

The interference covariance matrix is defined as

$$\mathbf{M} = \mathbb{E}\{\mathbf{y}\mathbf{y}^\dagger | H_0\} \tag{2.43}$$

and thus

$$\mathbf{M} = \begin{bmatrix} \mathbf{M}(0, 0) & \mathbf{M}(0, 1) & \dots & \mathbf{M}(0, (M-1)) \\ \mathbf{M}(1, 0) & \mathbf{M}(1, 1) & \dots & \mathbf{M}(1, (M-1)) \\ \vdots & \vdots & \ddots & \vdots \\ \mathbf{M}((M-1), 0) & \mathbf{M}((M-1), 1) & \dots & \mathbf{M}((M-1), (M-1)) \end{bmatrix} \quad (2.44)$$

where the spatial correlation matrices

$$\mathbf{M}(i, m) = \mathbb{E}\{\mathbf{y}_i \mathbf{y}_m^\dagger | H_0\}, \quad 0 \leq \{i, m\} \leq M-1 \quad (2.45)$$

are of dimension  $Q \times Q$ . Assuming that all the contributes are temporal stationary, the matrix becomes

$$\mathbf{M}(i, m) = \mathbf{M}(i-m) = \mathbf{M}^H(m-i) \quad (2.46)$$

and thus the covariance matrix becomes

$$\mathbf{M} = \begin{bmatrix} \mathbf{M}(0) & \mathbf{M}^H(1) & \dots & \mathbf{M}^H(M-1) \\ \mathbf{M}(1) & \mathbf{M}(0) & \dots & \mathbf{M}^H(M-2) \\ \vdots & \vdots & \ddots & \vdots \\ \mathbf{M}(M-1) & \mathbf{M}(M-2) & \dots & \mathbf{M}(0) \end{bmatrix} \quad (2.47)$$

which is Hermitian symmetric block-Toeplitz matrix consisting of  $M$  independent spatial correlation matrices.

Furthermore, the spatial correlation matrix can be written as

$$\begin{aligned} \mathbf{M}(m) &= \mathbb{E} \left\{ \begin{bmatrix} y_{0(m+i)} \\ y_{1(m+i)} \\ \vdots \\ y_{(Q-1)(m+i)} \end{bmatrix} \begin{bmatrix} y_{0i}^* & y_{1i}^* & \dots & y_{(Q-1)i}^* \end{bmatrix} | H_0 \right\} \\ &= \begin{bmatrix} \mathbf{m}_{11}(m) & \mathbf{m}_{12}(m) & \dots & \mathbf{m}_{1(Q-1)}(m) \\ \mathbf{m}_{21}(m) & \mathbf{m}_{22}(m) & \dots & \mathbf{m}_{2(Q-1)}(m) \\ \vdots & \vdots & \ddots & \vdots \\ \mathbf{m}_{(Q-1)1}(m) & \mathbf{m}_{(Q-1)2}(m) & \dots & \mathbf{m}_{(Q-1)(Q-1)}(m) \end{bmatrix}, \quad (2.48) \end{aligned}$$

where the variable  $m$  denotes the time interval and is  $0 \leq m \leq M-1$  and

$$\mathbf{m}_{qd}(m) = \mathbb{E}\{\mathbf{y}_{q(m+i)} \mathbf{y}_{di} | H_0\} \quad (2.49)$$

for  $0 \leq \{q, d\} \leq Q - 1$  and  $0 \leq m \leq M - 1$ , is the cross-correlation matrix between the  $q^{\text{th}}$  channel and the  $d^{\text{th}}$  channel. For any value  $m \neq 0$ , the matrix  $\mathbf{M}(m)$  includes  $Q^2$  independent entries and the matrix  $\mathbf{M}(0)$  includes  $Q(Q + 1)/2$  independent entries. The covariance matrix (2.47) for a time-stationary process includes

$$N_i = (M - 1)Q^2 + \frac{Q(Q + 1)}{2} \quad (2.50)$$

independent entries.



## Chapter 3

# Detection with Uniform Linear Arrays

A useful and widely used one-dimensional array is the *Uniform Linear Array* (ULA), which lies along one dimension and its elements are uniformly spaced. Fig. 3.1 shows a uniform linear array composed by  $N = 5$  elements;  $d$  represents the uniform interelement spacing. With this kind of array, it is very easy to locate each element, while it is sufficient the number of the element. In fact, assume that the array lies on the vector  $\mathbf{d}$ , as shown in figure, and as reference the element denoted by  $n = 0$ ; each position along the array is determined by

$$d_n = nd, \quad n = 0, \dots, N - 1 \quad (3.1)$$

where  $d_n$  locates the  $n^{\text{th}}$  element of the array. The position vector  $\mathbf{r}_n$  that locates the  $n^{\text{th}}$  element of the array in the coordinate system and the vector  $\mathbf{d}$  in general are not aligned. There are more than one choice for the reference of the array; it is also widely used to make the central element as reference. In this case the position is expressed as

$$d_n = \left( n - \frac{N - 1}{2} \right) d, \quad n = 0, \dots, N - 1 \quad (3.2)$$

while, in a general case of one-dimensional array with unequal spacing, the position is just expressed by  $d_n$ .

It is useful to particularize the signal relations for the case at hand. With the one-dimension array, the unit propagation vector that points the target can

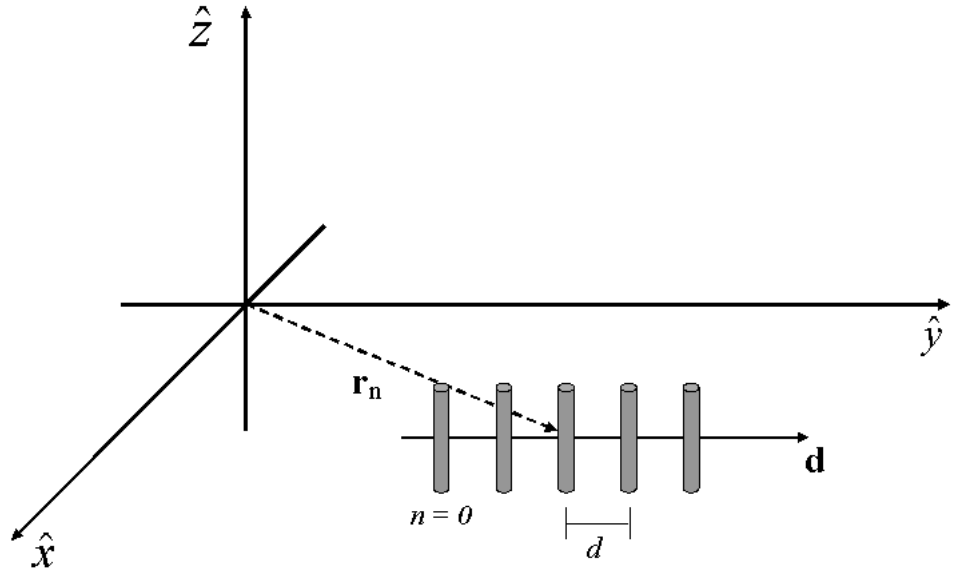


**Figure 3.1:** Uniform linear array with  $N = 5$  elements.  $d$  is the interelement spacing;  $n = 0$  characterizes the reference.

be expressed as

$$\hat{\mathbf{k}}(\varphi_t, \theta_t) = \cos \theta_t \sin \varphi_t \hat{\mathbf{x}} + \cos \theta_t \cos \varphi_t \hat{\mathbf{y}} + \sin \theta_t \hat{\mathbf{z}} \quad (3.3)$$

where  $\hat{\mathbf{x}}$ ,  $\hat{\mathbf{y}}$  and  $\hat{\mathbf{z}}$  are the unit vectors of the Cartesian coordinate system. Typically, the coordinate system is chosen with one axis coinciding with the vector  $\mathbf{d}$ ; in this case the position vector is aligned to the vector  $\mathbf{d}$  and it can be expressed as

$$\mathbf{r}_n = n\mathbf{d}, \quad n = 0, \dots, N - 1. \quad (3.4)$$

Without loss of generality, for the rest of the work let assume that the array lies on the  $x$  axis, thus

$$\mathbf{d} = d\hat{\mathbf{x}}. \quad (3.5)$$

Reporting here for simplicity the expression (1.13) for the relative delay at the  $n^{\text{th}}$  element

$$\tau_n' = -\frac{\hat{\mathbf{k}}(\varphi_t, \theta_t) \cdot \mathbf{r}_n}{c},$$

it is useful to particularize it for the case of interest, developing the product

$$\begin{aligned}\hat{\mathbf{k}}(\varphi_t, \theta_t) \cdot \mathbf{r}_n &= n\hat{\mathbf{k}}(\varphi_t, \theta_t) \cdot \mathbf{d} = \\ &= nd \cos \theta_t \sin \varphi_t\end{aligned}\quad (3.6)$$

from which the  $n^{\text{th}}$  relative delay becomes

$$\tau_n' = -n \frac{d}{c} \cos \theta_t \sin \varphi_t. \quad (3.7)$$

It is useful to define the target *spatial frequency*

$$\vartheta_t = \frac{\hat{\mathbf{k}}(\varphi_t, \theta_t) \cdot \mathbf{d}}{\lambda_0} = \frac{d}{\lambda_0} \cos \theta_t \sin \varphi_t, \quad (3.8)$$

so that the phase delay to the  $n^{\text{th}}$  element may be expressed as

$$-\varpi_0 \tau_n' = 2\pi n \vartheta_t. \quad (3.9)$$

This relation is useful in the expression of the spatial steering vector of the target. In fact, the spatial steering vector (1.26) may be expressed as

$$\mathbf{a}(\boldsymbol{\Upsilon}_t) = \left[ 1, e^{j2\pi\vartheta_t}, \dots, e^{j2(N-1)\pi\vartheta_t} \right] = \mathbf{a}(\vartheta_t) \quad (3.10)$$

where the dependence from the relative delays vector  $\boldsymbol{\Upsilon}_t$  is substituted by the spatial frequency  $\vartheta_t$ . This vector assumes a Vandermonde form due to the uniform spacing among the antenna elements. Thus, the sample relative to the  $n^{\text{th}}$  element and the  $m^{\text{th}}$  PRI is

$$y_{nm} = \alpha_t e^{j2\pi n \vartheta_t} e^{j2\pi m \varpi_t}, \quad \begin{array}{l} n = 0, \dots, N-1 \\ m = 0, \dots, M-1 \end{array}. \quad (3.11)$$

Finally, the space-time snapshot may be written in the same form as (1.29)

$$\mathbf{y}_t = \alpha_t \mathbf{b}(\varpi_t) \otimes \mathbf{a}(\vartheta_t) \quad (3.12)$$

and the target steering vector becomes

$$\mathbf{s}_t = \mathbf{s}(\vartheta_t, \varpi_t) = \mathbf{b}(\varpi_t) \otimes \mathbf{a}(\vartheta_t). \quad (3.13)$$

### 3.1 Mutual coupling and near-field effects

As seen in the previous section, the detection in presence of unknown parameters can be solved using the maximization of a likelihood ratio test. Both the receivers developed in literature and used here as reference have been devised under the ideal assumptions that

1. no mutual coupling between the antenna elements is present [47];
2. the far-field condition holds true, namely absence of near-field effects [48], [49].

Unfortunately in real environments the aforementioned effects cannot be neglected and their presence may determine a severe degradation of the radar detection performance. Indeed reflected radiation from one antenna element couples to its neighbors, as do currents that propagate along the surface of the array. As a consequence, mutual coupling arises, namely the primary voltage of each array element is the sum of the voltage due to the incident radiation plus all the contributions from the various coupling sources from each of its neighbors. On the other hand the wave-front arriving at the array cannot always be assumed planar. In fact specular reflections from the aircraft body are near-field sources which originate non-planar wave-front impinging on the array. Additionally the distance of the cell under test from the radar might not be significantly greater than the far-field distance.

The effects of a finite distance source on the performance of adaptive arrays has been studied in [49], where a rule of thumb is derived to determine the distance between the array center and the signal source at which the degradation of the output Signal to Noise Ratio (SNR) is negligible. The direction of arrival estimation in the presence of mutual coupling has been addressed in [50, 51] and [52], providing also the Cramer-Rao lower bound for the estimation error.

#### 3.1.1 Modelling Near Field Effects

A widely used model in array processing assumes that the signal impinging on the antenna is a far-field plane wave. As a consequence, the steering vector only depends on the angle between the source direction and the array baseline. However there are some practical situations where this model cannot be applied and it's necessary to use a near-field model. For instance, two cases of interest are:

- detection with distributed (or large) array. Given an antenna array, with aperture  $D$ , operating at wavelength  $\lambda$ , the far-field distance  $R$  has to comply with [56]

$$\begin{aligned} R &\gg D, \\ R &\gg \lambda, \\ R &\gg 2D^2/\lambda \end{aligned} \quad (3.14)$$

For a value  $D = 10$  m, if the antenna array works at a wavelength  $\lambda = 0.03$  m, the far-field distance is greater than 6000 m.

- detection in the presence of near-field specular reflections from the body of the aircraft [57];

It follows that in some applications the wave-front can't be assumed planar, but curved as a circle (see Figure 3.2, where the signal impinges on a uniform linear array of  $N + 1$  elements). The aforementioned signal model implies that

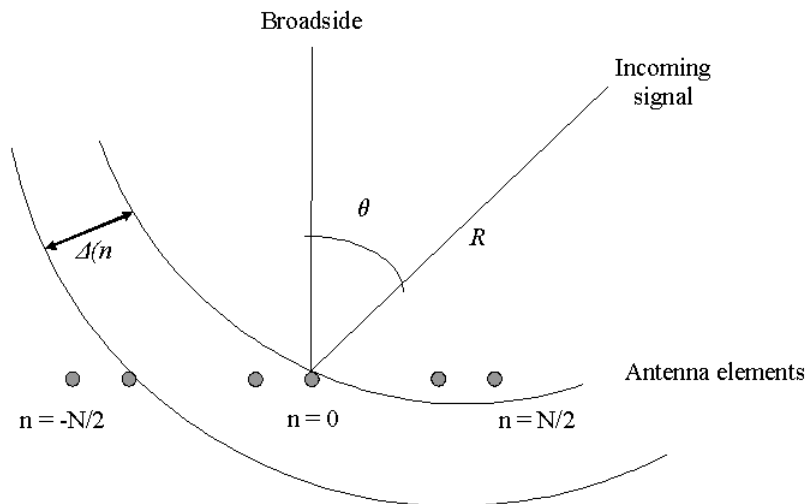


**Figure 3.2:** Spherical wave-front model with the source signal arriving broadside to the array.  $d$  is the interelement spacing and  $\Delta(n)$  is the path delay across the array at element position  $n$ ;  $\theta$  is the direction of arrival measured from the array broadside;  $R$  is the curvature radius of the wave-front.

the steering vector depends not only on the angle  $\theta$ , but also on the curvature radius  $R$ . The path delay  $\Delta(n)$  at the  $n$ -th element relative to the centre is given by

$$\Delta(n) = \sqrt{(R \cos \theta)^2 + (R \sin \theta + nd)^2} - R. \quad (3.15)$$

Defining the inverse of the curvature radius  $r = \frac{1}{R}$  and simplifying Eq. (3.15) using Taylor's expansion, we may write

$$\Delta(n) = nd \sin(\theta) + \frac{1}{2} r n^2 d^2 - \frac{r}{8} (2nd \sin(\theta) + r n^2 d^2)^2 \quad (3.16)$$

where

$$\frac{1}{2} r n^2 d^2$$

is the first order correction and

$$\frac{r}{8} (2nd \sin(\theta) + r n^2 d^2)^2$$

is the second order correction in the Taylor's expansion. As a consequence, the  $(N + 1)$ -dimensional steering vector  $\mathbf{s}_n$  can be written as [57]

$$\mathbf{s}_n = \left( e^{-j2\pi\Delta(N/2)/\lambda}, \dots, e^{-j2\pi\Delta(1)/\lambda}, 1, e^{j2\pi\Delta(1)/\lambda}, \dots, e^{j2\pi\Delta(N/2)/\lambda} \right)^T \quad (3.17)$$

where  $j = \sqrt{-1}$ . We also highlight that  $R = 0$  corresponds to an incoming wave-front in the far-field (i.e. plane wave).

### 3.1.2 Modelling Mutual Coupling

An important electromagnetic phenomenon, quite always present, and which strongly affects the performance of an adaptive antenna array, is the mutual coupling between the array elements. It is well known that ignoring mutual coupling can lead to a significant performance degradation of adaptive array signal processing algorithms. If mutual coupling is properly accounted for, the performance loss can be restored [52], [58]. Practical antenna systems have significant levels of mutual coupling [53, 54, 55].

Most of previous work, in adaptive detection, is based on idealized antenna arrays, i.e. it is assumed that the antenna elements of the receiving array are independent isotropic omnidirectional point sensors that do not re-radiate the incident signals. In a practical case, each array element has some physical size and re-radiates the incident field. The re-radiated fields interact with the other

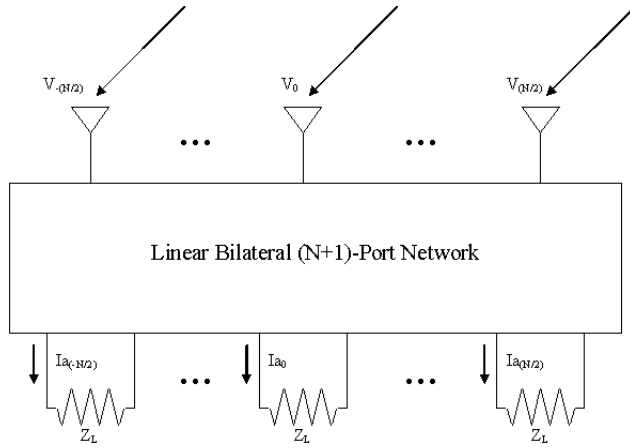


**Figure 3.3:** Antenna array as a linear bilateral  $N + 1$  port network

elements causing the sensors to be mutual coupled [59]. These effects become particularly significant as the interelement spacing decreases and are rather drastic if the interelement spacing drops below half a wavelength. Indeed, ignoring these effects is tantamount to assuming that the antenna elements are each other isolated [47].

In order to model the mutual coupling let us consider the scheme in Figure 3.3 which shows an  $N + 1$  elements array excited by a plane wave and where each element is terminated on a load impedance  $Z_L$ . The vector of voltages without mutual coupling effects included  $\mathbf{V}$  and the vector of induced terminal currents  $\mathbf{I}_a$ , that include mutual coupling, are related through a linear system of equation [47, 52, 58]

$$\mathbf{V} = (\mathbf{Z} + Z_L \mathbf{I}) \mathbf{I}_a, \quad (3.18)$$

where

$$\mathbf{Z} = \begin{pmatrix} Z_{1,1} & Z_{1,2} & \dots & Z_{1,N+1} \\ Z_{2,1} & Z_{2,2} & \dots & Z_{2,N+1} \\ \vdots & \vdots & \ddots & \vdots \\ Z_{N+1,1} & Z_{N+1,2} & \dots & Z_{N+1,N+1} \end{pmatrix} \quad (3.19)$$

is the mutual coupling matrix and  $\mathbf{I}$  denotes the identity matrix. The impedance matrix  $\mathbf{Z} + Z_L \mathbf{I}$  is an inherent characteristic of the antenna array, which depends only on the antenna elements and the array geometry and does not depend upon the angle of arrival of the incident radiation. In particular it is

independent of the signal environment [58]. The symmetry of the problem implies that  $Z_{i,j} = Z_{j,i}$ , namely  $\mathbf{Z} + Z_L \mathbf{I}$  is a symmetric matrix, which is usually known or appreciable [51]. Eq. (3.18) can be also written as

$$\mathbf{V} = \left( \frac{\mathbf{Z}}{Z_L} + \mathbf{I} \right) \mathbf{V}_0, \quad (3.20)$$

where  $\mathbf{V}_0 = Z_L \mathbf{I}_a$  is the vector of actual voltages at antenna terminals that includes the effects of mutual coupling. Solving for the actual voltages, (3.20) becomes

$$\mathbf{V}_0 = (\mathbf{Z} + Z_L \mathbf{I})^{-1} \mathbf{V} = \mathbf{C} \mathbf{V}, \quad (3.21)$$

where  $\mathbf{C} = (\mathbf{Z} + Z_L \mathbf{I})^{-1}$ . It follows that the actual steering vector at the input of the adaptive processor is

$$\mathbf{s}_t = \mathbf{C} \mathbf{s}_n,$$

where  $\mathbf{s}_n$  is, to within a constant, the ideal steering vector in absence of mutual coupling. In general, the matrix  $\mathbf{C}$  has no special structure. However, for the case of a linear array that is well balanced, a banded matrix provides an excellent model [50, 52]. The rationale behind this model is that the mutual coupling coefficients are inversely proportional to the distance between the elements. Hence the mutual coupling between two elements which are far enough each other can often be approximated as zero. Finally, for linear arrays, it is reasonably expected that the matrix  $\mathbf{C}$  follows a banded Toeplitz structure [50, 52].

### 3.1.3 Problem Formulation and Design Issues

Let us assume that data are collected by  $N + 1$  sensors and denote by  $\mathbf{y}$  the complex vector of the samples from the range cell where the presence of the useful target is sought (primary data). As in [8], we also suppose that a secondary data set  $\mathbf{y}_k$ ,  $k = 1, \dots, K$ , is available ( $K \geq N + 1$ ), that each of such snapshots does not contain any useful target echo and exhibits the same covariance matrix as the primary data.

The detection problem to be solved can be formulated in terms of the following binary hypotheses test

$$\left\{ \begin{array}{l} H_0 : \left\{ \begin{array}{l} \mathbf{y} = \mathbf{n} \\ \mathbf{y}_k = \mathbf{n}_k \quad k = 1, \dots, K \end{array} \right. \\ H_1 : \left\{ \begin{array}{l} \mathbf{y} = \alpha_t \mathbf{s}_t + \mathbf{n} \\ \mathbf{y}_k = \mathbf{n}_k \quad k = 1, \dots, K \end{array} \right. \end{array} \right. \quad (3.22)$$

where  $\mathbf{s}_t$  denotes the actual steering vector and  $\alpha_t$  is an unknown complex parameter accounting for the channel propagation effects as well as the target reflectivity. We assume that the disturbance components  $\mathbf{n}$  and  $\mathbf{n}_k$ 's,  $k = 1, \dots, K$ , are independent complex circular Gaussian vectors with zero mean and covariance matrix given by

$$\mathbb{E}[\mathbf{n}\mathbf{n}^\dagger] = \mathbb{E}[\mathbf{n}_k\mathbf{n}_k^\dagger] = \mathbf{M},$$

Exploiting the models of Sections 3.1.1 and 3.1.2, the actual steering vector  $\mathbf{s}_t$  can be written as

$$\mathbf{s}_t = \mathbf{C} \left( e^{-j2\pi\Delta(N/2)/\lambda}, \dots, e^{-j2\pi\Delta(1)/\lambda}, 1, e^{j2\pi\Delta(1)/\lambda}, \dots, e^{j2\pi\Delta(N/2)/\lambda} \right)^T. \quad (3.23)$$

Under the ideal conditions of far-field and absence of mutual coupling the actual steering vector  $\mathbf{s}_t$  can be obtained letting in (3.23)  $r = 0$  and  $\mathbf{C} = \mathbf{I}$ , i.e.

$$\mathbf{s}_t = \mathbf{s} = \left( e^{-j2\pi(N/2)d \sin(\theta)/\lambda}, \dots, e^{-j2\pi d \sin(\theta)/\lambda}, 1, e^{j2\pi d \sin(\theta)/\lambda}, \dots, e^{j2\pi(N/2)d \sin(\theta)/\lambda} \right)^T. \quad (3.24)$$

According to the Neyman-Pearson criterion, a UMP test for the quoted problem does not exist, since the optimum detector requires the knowledge of the parameters  $\mathbf{M}$ ,  $\alpha_t$ , and  $r$ , which, in practical situations, are unknown. A possible way to circumvent this drawback is to exploit GLRT techniques, which are equivalent to replacing the unknown parameters with their maximum likelihood estimates. Following this guideline, we devise both one-step GLRT- and two-step GLRT-based detectors for the quoted problem.

### One-step GLRT detectors

The criterion is equivalent to replace in the likelihood ratio the unknown parameters with their maximum likelihood estimates under each hypotheses, based upon the entirety of data [60]. For present problem the one-step GLRT is given by

$$\frac{\max_{r, \alpha_t, \mathbf{M}} f(\mathbf{y}, \mathbf{y}_1, \dots, \mathbf{y}_K | \alpha_t, \mathbf{M}, r, H_1)}{\max_{\mathbf{M}} f(\mathbf{y}, \mathbf{y}_1, \dots, \mathbf{y}_K | \mathbf{M}, H_0)} \underset{H_0}{\overset{H_1}{>}} T \quad (3.25)$$

where  $f(\mathbf{y}, \mathbf{y}_1, \dots, \mathbf{y}_K | \alpha_t, \mathbf{M}, r, H_1) = f_1$  and  $f(\mathbf{y}, \mathbf{y}_1, \dots, \mathbf{y}_K | \mathbf{M}, H_0) = f_0$  are the complex multivariate probability density functions (pdf's). Previous

assumptions imply that

$$f_1 = \frac{1}{\pi^{N(K+1)} \det^{K+1}(\mathbf{M})} \exp \left\{ -\text{tr} [\mathbf{W}_1 \mathbf{M}^{-1}] \right\} \quad (3.26)$$

$$f_0 = \frac{1}{\pi^{N(K+1)} \det^{K+1}(\mathbf{M})} \exp \left\{ -\text{tr} [\mathbf{W}_0 \mathbf{M}^{-1}] \right\}$$

where  $\text{tr}(\cdot)$  denotes the trace of a square matrix,  $\mathbf{W}_1$  and  $\mathbf{W}_0$  are defined as:

$$\mathbf{W}_1 = (\mathbf{y} - \alpha_t \mathbf{s}_t) (\mathbf{y} - \alpha_t \mathbf{s}_t)^\dagger + \sum_{k=1}^K \mathbf{y}_k \mathbf{y}_k^\dagger \quad (3.27)$$

$$\mathbf{W}_0 = \mathbf{y} \mathbf{y}^\dagger + \sum_{k=1}^K \mathbf{y}_k \mathbf{y}_k^\dagger.$$

Maximizing over  $\mathbf{M}$ , Eq. (3.26) becomes

$$\max_{\mathbf{M}} f_1 = \frac{C}{\det^{K+1}(\mathbf{W}_1)} \quad (3.28)$$

$$\max_{\mathbf{M}} f_0 = \frac{C}{\det^{K+1}(\mathbf{W}_0)}$$

where  $C$  denotes a constant value. Substituting (3.28) in (3.25), after some algebra, we can recast the GLRT as:

$$\frac{\det(\mathbf{W}_0)}{\min_{r, \alpha_t} \det(\mathbf{W}_1)} \underset{H_0}{\overset{H_1}{>}} T \quad (3.29)$$

where  $T$  is a suitable modification of the original threshold. Moreover, exploiting [61, p. 594 Corollary A.3.1], we can re-write (3.29) as

$$\frac{1 + \mathbf{y}^\dagger \widehat{\mathbf{M}}^{-1} \mathbf{y}}{1 + \min_{r, \alpha_t} \left[ (\mathbf{y} - \alpha_t \mathbf{s}_t)^\dagger \widehat{\mathbf{M}}^{-1} (\mathbf{y} - \alpha_t \mathbf{s}_t) \right]} \underset{H_0}{\overset{H_1}{>}} T \quad (3.30)$$

where  $\widehat{\mathbf{M}} = \sum_{k=1}^K \mathbf{y}_k \mathbf{y}_k^\dagger$  is the secondary data sample covariance matrix [8]. The value of  $\alpha_t$  which minimizes the denominator of the Left Hand Side (LHS) of (3.30) is

$$\widehat{\alpha}_t = \frac{\mathbf{s}_t^\dagger \widehat{\mathbf{M}}^{-1} \mathbf{y}}{\mathbf{s}_t^\dagger \widehat{\mathbf{M}}^{-1} \mathbf{s}_t}, \quad (3.31)$$

which substituted in (3.30) yields

$$\frac{1 + \mathbf{y}^\dagger \widehat{\mathbf{M}}^{-1} \mathbf{y}}{1 + \mathbf{y}^\dagger \widehat{\mathbf{M}}^{-1} \mathbf{y} - \max_r \frac{|\mathbf{y}^\dagger \widehat{\mathbf{M}}^{-1} \mathbf{s}_a|^2}{\mathbf{s}_a^\dagger \widehat{\mathbf{M}}^{-1} \mathbf{s}_a}} \begin{matrix} H_1 \\ > \\ < \\ H_0 \end{matrix} T. \quad (3.32)$$

Notice that if we are interested to detect the presence of a possible target at the range distance  $\overline{R}$ , it is reasonable to assume that  $r$  ranges between

$$r_{Min} = \frac{1}{\overline{R} + R_s/2} \quad \text{and} \quad r_{Max} = \frac{1}{\overline{R} - R_s/2} \quad (3.33)$$

where  $R_s$  is the system range resolution. This consideration implies that (3.32) can be recast as

$$\frac{1}{1 + \mathbf{y}^\dagger \widehat{\mathbf{M}}^{-1} \mathbf{y}} \max_{r \in [r_{Min}, r_{Max}]} \frac{|\mathbf{y}^\dagger \widehat{\mathbf{M}}^{-1} \mathbf{C} \mathbf{s}_t|^2}{\mathbf{s}_t^\dagger \mathbf{C}^* \widehat{\mathbf{M}}^{-1} \mathbf{C} \mathbf{s}_t} \begin{matrix} H_1 \\ > \\ < \\ H_0 \end{matrix} T \quad (3.34)$$

where  $T$  is a modification of the threshold in (3.32) and  $\mathbf{s}_t$  is defined in (3.17). Since the maximization in (3.34) cannot be performed analytically we resort to two different approximations:

1. We approximate the maximization through an exhaustive search over a finite grid  $\mathcal{G}$  of  $P + 1$  equally spaced points,

$$r_i = \frac{i(r_{Max} - r_{Min})}{P} + r_{Min} \quad i = 0, \dots, P. \quad (3.35)$$

This approximation implies that (3.34) can be finally written as

$$\frac{1}{1 + \mathbf{y}^\dagger \widehat{\mathbf{M}}^{-1} \mathbf{y}} \max_{r \in \mathcal{G}} \frac{|\mathbf{y}^\dagger \widehat{\mathbf{M}}^{-1} \mathbf{C} \mathbf{s}_t|^2}{\mathbf{s}_t^\dagger \mathbf{C}^* \widehat{\mathbf{M}}^{-1} \mathbf{C} \mathbf{s}_t} \begin{matrix} H_1 \\ > \\ < \\ H_0 \end{matrix} T. \quad (3.36)$$

This detector will be referred to as Near-Field Mutual Coupling 1S-GLRT (NF-MC-1S-GLRT) and its block diagram is illustrated in Figure 3.4, where

$$\Lambda(r_i) = \left. \frac{|\mathbf{y}^\dagger \widehat{\mathbf{M}}^{-1} \mathbf{C} \mathbf{s}_t|^2}{\mathbf{s}_t^\dagger \mathbf{C}^* \widehat{\mathbf{M}}^{-1} \mathbf{C} \mathbf{s}_t} \right|_{r=r_i}$$

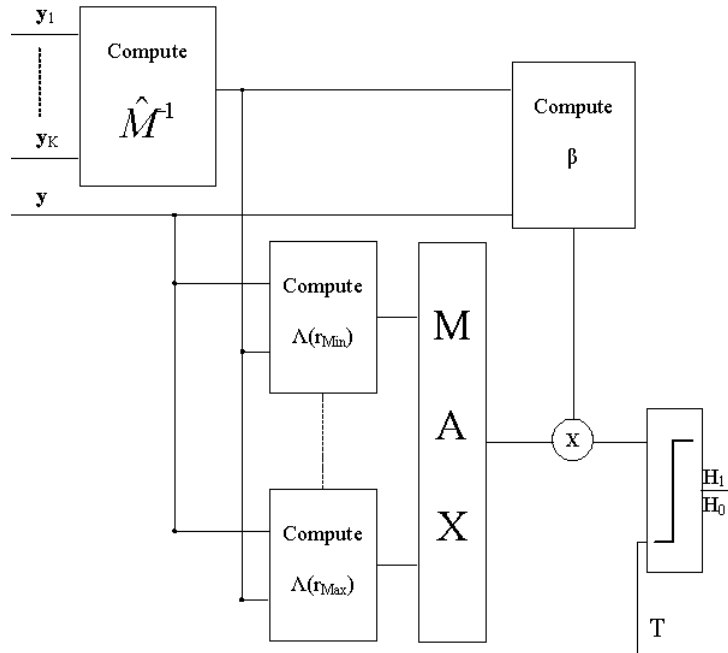


**Figure 3.4:** Block diagram of the NF-MC-1S-GLRT

and

$$\beta = \frac{1}{1 + \mathbf{y}^\dagger \widehat{\mathbf{M}}^{-1} \mathbf{y}}.$$

Notice that the higher the cardinality of the search-grid the higher the computational complexity required for the evaluation of the decision statistic.

2. We avoid to perform the maximization and calculate the function  $\Lambda(r)$  in the center of  $[r_{Min}, r_{Max}]$ , i.e.

$$r_{med} = \frac{r_{Max} + r_{Min}}{2}.$$

With this approximation we come up with the following decision statistic

$$\frac{1}{1 + \mathbf{y}^\dagger \widehat{\mathbf{M}}^{-1} \mathbf{y}} \left| \frac{\mathbf{y}^\dagger \widehat{\mathbf{M}}^{-1} \mathbf{C} \mathbf{s}_t}{\mathbf{s}_t^\dagger \mathbf{C}^* \widehat{\mathbf{M}}^{-1} \mathbf{C} \mathbf{s}_t} \right|_{r=r_{med}} \begin{matrix} > \\ < \\ < \end{matrix} T, \quad \begin{matrix} H_1 \\ > \\ H_0 \end{matrix} \quad (3.37)$$

referred to, in the sequel, as the Medium NF-MC-1S-GLRT (MNF-MC-1S-GLRT).

A comparison can be made between this proposed receivers and the GLRT derived in [8], which assumes far-field conditions and absence of mutual coupling, i.e.

$$\frac{\left| \mathbf{y}^\dagger \widehat{\mathbf{M}}^{-1} \mathbf{s} \right|^2}{\left( 1 + \mathbf{y}^\dagger \widehat{\mathbf{M}}^{-1} \mathbf{y} \right) \mathbf{s}^\dagger \widehat{\mathbf{M}}^{-1} \mathbf{s}} \underset{H_0}{\overset{H_1}{>}} T, \quad (3.38)$$

where  $\mathbf{s}$  is the ideal steering vector (3.24). The only difference between the LHS's of (3.38), (3.34) and (3.37) is that (3.38) exploits the ideal steering vector for matched filtering operations, while (3.34) and (3.37) resort to an estimate of the actual steering vector which compensates the mutual coupling and accounts for the near-field effect. As a consequence the new receivers try to use a projection direction as close as to that of the actual steering vector, thereby reducing the steering mismatch loss which is suffered by the conventional GLRT of Kelly.

### Two-step GLRT detectors

This design procedure is organized in two-steps. First it assumes the knowledge of the disturbance covariance matrix  $\mathbf{M}$  and derives the GLRT maximizing the likelihood ratio over  $\alpha_t$  and  $r$ . Then, after the GLRT is derived, the sample covariance matrix, based upon the secondary data, is inserted, in place of the true value, into the test. This guideline has been followed in [11] assuming ideal conditions of far-field and absence of mutual coupling.

**Step 1.** For the present problem the test at the step 1 can be written as

$$\frac{\max_{r, \alpha_t} f(\mathbf{y} | \alpha_t, \mathbf{M}, r, H_1)}{f(\mathbf{y} | \mathbf{M}, H_0)} \underset{H_0}{\overset{H_1}{>}} T, \quad (3.39)$$

where the  $f(\mathbf{y} | \alpha_t, \mathbf{M}, r, H_1)$  and  $f(\mathbf{y} | \mathbf{M}, H_0)$  denote the primary data complex multivariate Gaussian pdf's under the hypotheses  $H_1$  and  $H_0$  respectively, i.e.

$$f(\mathbf{y} | \alpha_t, \mathbf{M}, r, H_1) = \frac{1}{\pi^N \det(\mathbf{M})} \exp \left\{ -\text{tr} \left[ \mathbf{M}^{-1} (\mathbf{y} - \alpha_t \mathbf{s}_t) (\mathbf{y} - \alpha_t \mathbf{s}_t)^\dagger \right] \right\}$$

$$f(\mathbf{y} | \mathbf{M}, H_0) = \frac{1}{\pi^N \det(\mathbf{M})} \exp \left\{ -\text{tr} \left[ \mathbf{M}^{-1} \mathbf{y} \mathbf{y}^\dagger \right] \right\}. \quad (3.40)$$

Substituting (3.40) in (3.39), after some algebra, the test becomes

$$\max_{r, \alpha_t} \left[ -(\mathbf{y} - \alpha_t \mathbf{s}_t)^\dagger \mathbf{M}^{-1} (\mathbf{y} - \alpha_t \mathbf{s}_t) + \mathbf{y}^\dagger \mathbf{M}^{-1} \mathbf{y} \right] \underset{H_0}{\overset{H_1}{>}} T, \quad (3.41)$$

where  $T$  is a modification of the original threshold. Maximizing (3.41) over  $\alpha_t$  yields

$$\max_{r \in [r_{Min}, r_{Max}]} \frac{|\mathbf{y}^\dagger \mathbf{M}^{-1} \mathbf{C} \mathbf{s}_t|^2}{\mathbf{s}_t^\dagger \mathbf{C}^* \mathbf{M}^{-1} \mathbf{C} \mathbf{s}_t} \underset{H_0}{\overset{H_1}{>}} T. \quad (3.42)$$

Notice that, like in (3.34), the maximization over  $r$  cannot be performed analytically and thus we resort to either an exhaustive search over the finite grid  $\mathcal{G}$ , defined in (3.35), and composed of  $P + 1$  equally spaced points, or evaluate the objective function in  $r_{med}$ .

**Step 2.** The derived tests require the knowledge of the disturbance covariance matrix. In many practical cases, this matrix is unknown and must be on-line estimated. To this end we substitute the sample covariance matrix  $\widehat{\mathbf{M}}$ , based on secondary data, in place of  $\mathbf{M}$ . As a consequence the two-step GLRT-based detectors can be written as

$$\max_{r \in \mathcal{G}} \frac{|\mathbf{y}^\dagger \widehat{\mathbf{M}}^{-1} \mathbf{C} \mathbf{s}_t|^2}{\mathbf{s}_t^\dagger \mathbf{C}^* \widehat{\mathbf{M}}^{-1} \mathbf{C} \mathbf{s}_t} \underset{H_0}{\overset{H_1}{>}} T. \quad (3.43)$$

referred to as NF-MC-2S-GLRT, and

$$\left. \frac{|\mathbf{y}^\dagger \widehat{\mathbf{M}}^{-1} \mathbf{C} \mathbf{s}_t|^2}{\mathbf{s}_t^\dagger \mathbf{C}^* \widehat{\mathbf{M}}^{-1} \mathbf{C} \mathbf{s}_t} \right|_{r=r_{med}} \underset{H_0}{\overset{H_1}{>}} T, \quad (3.44)$$

referred to as MNF-MC-2S-GLRT.

Detectors (3.43) and (3.44) are less computationally intensive than 1S-GLRT-based receivers as they don't require the on-line calculation of  $\beta$ .

A comparison can be made between the new receivers and the AMF [11], i.e.

$$\frac{|\mathbf{s}^\dagger \widehat{\mathbf{M}}^{-1} \mathbf{y}|^2}{\mathbf{s}^\dagger \widehat{\mathbf{M}}^{-1} \mathbf{s}} \underset{H_0}{\overset{H_1}{>}} \gamma. \quad (3.45)$$

The only difference is that the LHS of (3.45) exploits the ideal steering vector, while (3.43) and (3.44) resort to an estimate of the actual one which compensates the mutual coupling and accounts for the near-field effect.

### 3.1.4 Performance Analysis

This section is devoted to the performance analysis of the NF-MC-1S-GLRT, MNF-MC-1S-GLRT, NF-MC-2S-GLRT and MNF-MC-2S-GLRT, proposed in the previous sections, in comparison with the classic Kelly's receiver, the AMF, and the GLRT detectors which only compensate the mutual coupling, i.e.

$$\frac{|\mathbf{y}^\dagger \widehat{\mathbf{M}}^{-1} \mathbf{C}_s|^2}{\mathbf{s}^\dagger \mathbf{C}^* \widehat{\mathbf{M}}^{-1} \mathbf{C}_s (1 + \mathbf{y}^\dagger \widehat{\mathbf{M}}^{-1} \mathbf{y})} \underset{H_0}{\overset{H_1}{>}} T \quad (3.46)$$

and

$$\frac{|\mathbf{y}^\dagger \widehat{\mathbf{M}}^{-1} \mathbf{C}_s|^2}{\mathbf{s}^\dagger \mathbf{C}^* \widehat{\mathbf{M}}^{-1} \mathbf{C}_s} \underset{H_0}{\overset{H_1}{>}} T. \quad (3.47)$$

These last decision rules will be referred to in the sequel as the MC-1S-GLRT and MC-2S-GLRT respectively. In table 1 we report the association between the used acronyms and the corresponding detection rules. Since closed form expressions for the false alarm probability ( $P_{FA}$ ) and the detection probability ( $P_D$ ) are not available we resort to Montecarlo simulations and, in order to limit the computational burden, we set  $P_{FA} = 10^{-4}$ .

We also assume  $N = 84$ ,  $K = 2(N + 1)$ ,  $\theta = 40$  deg, and  $R_s = 50$  m. The matrix  $\mathbf{C}$ , which accounts for the mutual coupling, is modelled as a  $(N + 1) \times (N + 1)$  banded Toeplitz matrix, i.e.

$$\mathbf{C} = \begin{bmatrix} c_1 & c_2 & c_3 & c_4 & \dots & c_{20} & 0 & 0 & 0 & \dots & 0 & 0 \\ c_2 & c_1 & c_2 & c_3 & \dots & c_{19} & c_{20} & 0 & 0 & \dots & 0 & 0 \\ c_3 & c_2 & c_1 & c_2 & \dots & c_{18} & c_{19} & c_{20} & 0 & \dots & 0 & 0 \\ \vdots & \ddots & \vdots & \vdots \\ c_{19} & c_{18} & c_{17} & c_{16} & \dots & c_2 & c_3 & c_4 & c_5 & \dots & 0 & 0 \\ c_{20} & c_{19} & c_{18} & c_{17} & \dots & c_1 & c_2 & c_3 & c_4 & \dots & 0 & 0 \\ \vdots & \ddots & \vdots & \vdots \\ 0 & 0 & 0 & 0 & \dots & 0 & 0 & 0 & 0 & \dots & c_1 & c_2 \\ 0 & 0 & 0 & 0 & \dots & 0 & 0 & 0 & 0 & \dots & c_2 & c_1 \end{bmatrix} \quad (3.48)$$

where

$$c(l) = (1 + j) [1 - (l - 1)0.05], \quad l = 1, \dots, 20. \quad (3.49)$$

Detection rule	Acronym
Classic Kelly Receiver (3.38)	Kelly's GLRT
Classic AMF Receiver (3.45)	AMF
Mutual Coupling 1S-GLRT (3.47)	MC-1S-GLRT
Mutual Coupling 2S-GLRT (3.46)	MC-2S-GLRT
Near-Field and Mutual Coupling 1S-GLRT (3.36)	NF-MC-1S-GLRT
Near-Field and Mutual Coupling 2S-GLRT (3.43)	NF-MC-2S-GLRT
Medium Near-Field and Mutual Coupling 1S-GLRT (3.37)	MNF-MC-1S-GLRT
Medium Near-Field and Mutual Coupling 2S-GLRT (3.44)	MNF-MC-2S-GLRT

**Table 3.1:** Detection rules and corresponding acronyms.

As to the near-field effects we suppose that the actual distance  $R$  between the array center and the target position is uniformly distributed between  $\bar{R} - R_s/2$  and  $\bar{R} + R_s/2$ . The parameter  $\bar{r}$  assumes several values corresponding to different situations, namely  $\bar{R} = 700$  m (near-field situation),  $\bar{R} = 1100$  m (limiting situation between near- and far-field regions), and  $\bar{R} = 4000$  m (far-field situation).

Finally the simulated disturbance scenario includes three far field jammers with directions of arrival  $\theta_1 = 10$  deg,  $\theta_2 = 15$  deg,  $\theta_3 = 20$  deg, and Jammer to Noise Ratios (JNR's) equal to  $\text{JNR}_1 = 20$  dB,  $\text{JNR}_2 = 20$  dB, and  $\text{JNR}_3 = 30$  dB respectively.

In Figure 3.5,  $P_D$  is plotted versus the Signal to Interference plus Noise Ratio (SINR), i.e.

$$\text{SINR} = |\alpha|^2 \mathbf{s}^\dagger \mathbf{M}^{-1} \mathbf{s},$$

for the near-field situation  $\bar{R} = 700$  m. The plots show that the NF-MC-1S-GLRT, the MNF-MC-1S-GLRT, the NF-MC-2S-GLRT and the MNF-MC-2S-GLRT achieve almost the same performance level and outperform the other receivers. Otherwise stated calculating the decision statistics over the grid or in the middle point is practically equivalent. Moreover the performance gain over the MC-1S-GLRT and MC-2S-GLRT, which only compensate the mutual coupling, is more than 2 dB for  $P_D = 0.9$ . The gain over the classic Kelly's receiver and AMF is very significant (11 dB with reference to the AMF and more than 24 dB with reference to Kelly's receiver for  $P_D = 0.9$ ). The worst performance of the Kelly's receiver was expected since the quoted processor

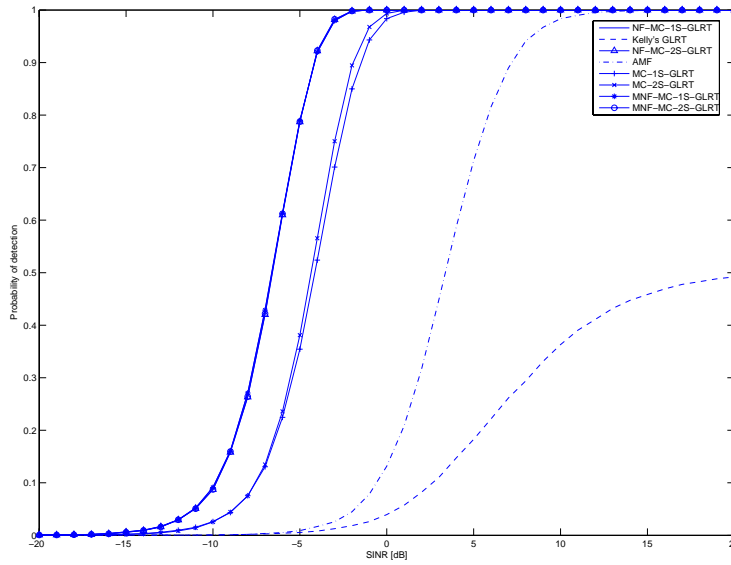


**Figure 3.5:**  $P_D$  versus SINR for  $P_{FA} = 10^{-4}$ ,  $N = 84$ ,  $K = 170$ ,  $P = 15$ , and  $\bar{R} = 700$  m.

is more selective than the AMF to possible mismatches between the nominal and the actual steering vector. The behaviour of the curves also highlight that, among the near-field and the mutual coupling, the dominant effect, which strongly affects the performance, is the mutual coupling.

In Figure 3.6 the performance obtained when  $\bar{R}$  is equal to 1100 m, i.e. at the limit of near-field region, is plotted. The curves exhibit a trend comparable to that of the previous figure. However the performance gap between the new receivers and those which compensate the mutual coupling only reduces to 1 dB for  $P_D = 0.9$ . This reduction can be explained observing that the near-field effect has become less significant. Finally the performance loss experienced by the Kelly's receiver and the AMF is always severe. Also in this case there are no performance differences between the NF-MC-1S-GLRT and the MNF-MC-1S-GLRT and between the NF-MC-2S-GLRT and the MNF-MC-2S-GLRT.

Figure 3.7 refers to a far-field scenario (namely  $\bar{R} = 4000$  m). The plots show that the performance of the NF-MC-1S-GLRT and NF-MC-2S-GLRT

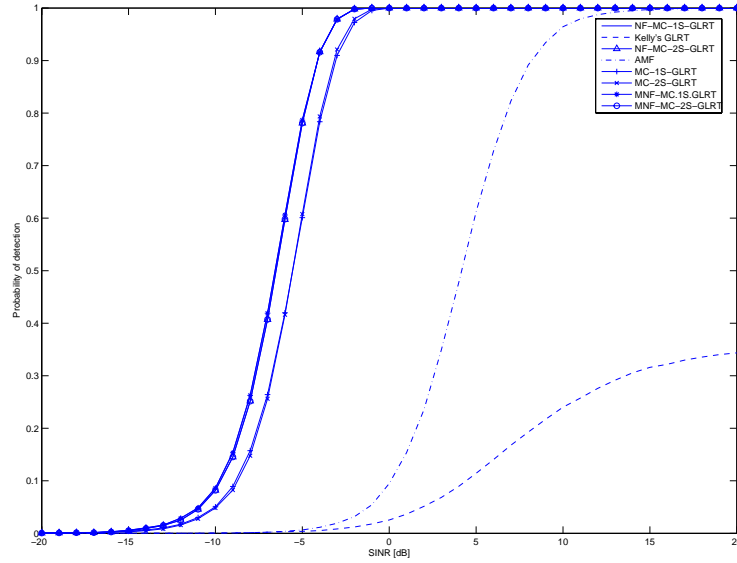


**Figure 3.6:**  $P_D$  versus SINR for  $P_{FA} = 10^{-4}$ ,  $N = 84$ ,  $K = 170$ ,  $P = 15$ , and  $\bar{R} = 1100$  m.

coincides with that of the MC-1S-GLRT and MC-2S-GLRT. This behaviour agrees with the fact that the near-field effects are absent and all the quoted receivers are capable of compensating the mutual coupling. Finally, in this case too, the performance loss of the classic receivers is very severe. As in the previous cases, there is no difference in maximizing over the grid or using the middle of the interval [70].

## 3.2 Partially-Homogeneous Environment

Adaptive detection of signals in the presence of disturbance with unknown covariance matrix has received a vibrant attention from the radar community in the recent past. Several receivers are nowadays available which exploit secondary (training) data [8], namely data vectors sharing the same spectral properties, in order to form an estimate of the disturbance covariance. Unfortunately, in several applications such as radar Space Time Adaptive Processing (STAP),

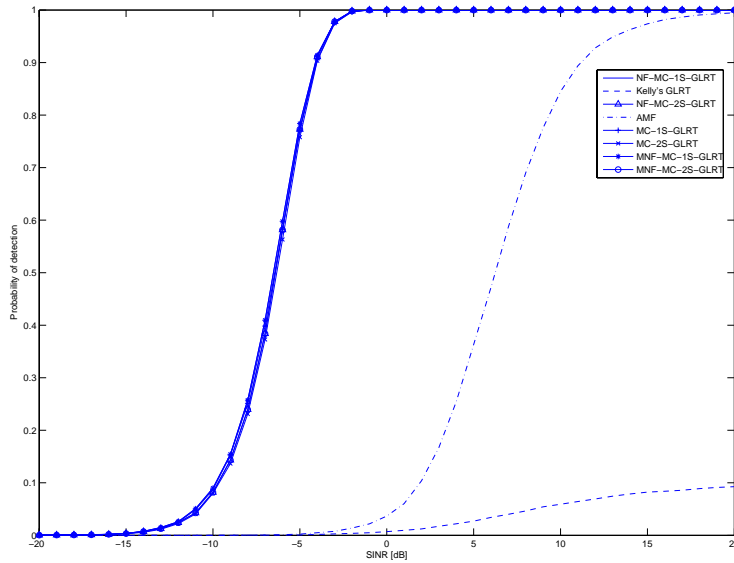


**Figure 3.7:**  $P_D$  versus SINR for  $P_{FA} = 10^{-4}$ ,  $N = 84$ ,  $K = 170$ ,  $P = 15$ , and  $\bar{R} = 4000$  m.

the number of homogeneous secondary data is often limited [62]. It is thus of primary concern to exploit the structural information about the disturbance covariance in order to decrease the sample support required to achieve satisfactory performances and to reduce the uncertainty in learning. Several results concerning this subject can be found in open literature. In [63], the author highlights that if the  $N$  elements of a linear array are symmetrically spaced with respect to the phase center, the covariance matrix of the impinging disturbance is persymmetric. Specifically it has a doubly symmetric form, namely it is hermitian about its principal diagonal and persymmetric about its cross diagonal (the toeplitz structure which results for the case of a uniformly spaced array or pulse train is a special case of the persymmetry). In the same paper the author also derives the Maximum Likelihood (ML) estimator of the disturbance covariance under the constraint of persymmetry. Moreover, in [64], the aforementioned property is exploited to devise an adaptive detector for multi-band signals in the presence of homogeneous Gaussian disturbance.

We deal with adaptive detection of a signal known up to a scaling factor in the presence of partially homogeneous disturbance [65, 66] with persymmetric covariance matrix. We evaluate the Generalized Likelihood Ratio Test (GLRT) and compare its performance with the unstructured GLRT which does not exploit the persymmetry property. This last detector is the Adaptive Coherence Estimator (ACE) [65], also known as the Adaptive Normalized Matched Filter (ANMF) [67].

### 3.2.1 Problem Formulation and Design issues

Assume that data are collected by  $N$  sensors and let  $\mathbf{y}$  be the complex vector of the samples where the presence of the useful signal is sought (primary data). As in [8], we suppose that a secondary data set  $\mathbf{y}_t$ ,  $t = 1, \dots, K$  ( $K \geq N$ ), is available, that each of such snapshots does not contain any useful signal, and exhibits the same covariance structure as the primary data.

The detection problem to be solved can be formulated in terms of the following binary hypotheses test

$$\begin{cases} H_0 : \begin{cases} \mathbf{y} = \mathbf{n} \\ \mathbf{y}_k = \mathbf{n}_k, \quad k = 1, \dots, K \end{cases} \\ H_1 : \begin{cases} \mathbf{y} = \alpha \mathbf{s}_t + \mathbf{n} \\ \mathbf{y}_k = \mathbf{n}_k, \quad k = 1, \dots, K \end{cases} \end{cases} \quad (3.50)$$

where  $\alpha$  is an unknown deterministic parameter.

As to the disturbance components, we assume that  $\mathbf{n}$  and  $\mathbf{n}_k$ 's,  $k = 1, \dots, K$ , are independent complex circular zero-mean Gaussian vectors with covariance matrix given by

$$\begin{cases} \mathbb{E}[\mathbf{n}\mathbf{n}^\dagger] = \mathbf{M}, \\ \mathbb{E}[\mathbf{n}_k\mathbf{n}_k^\dagger] = \gamma\mathbf{M}, \quad k = 1, \dots, K \end{cases} \quad (3.51)$$

where  $\gamma > 0$ . Moreover, we suppose that  $\mathbf{M}$  is a positive definite hermitian and persymmetric matrix, namely, it belongs to the set  $\mathcal{P}$  defined as

$$\mathbf{M} \in \mathcal{P} \text{ if } \mathbf{M} = \mathbf{J}\mathbf{M}^*\mathbf{J},$$

where  $\mathbf{J}$  is the permutation matrix, i.e.

$$\mathbf{J} = \begin{bmatrix} 0 & 0 & \cdots & 0 & 1 \\ 0 & 0 & \cdots & 1 & 0 \\ \vdots & \vdots & \vdots & \vdots & \vdots \\ 1 & 0 & \cdots & 0 & 0 \end{bmatrix}.$$

Finally we suppose that the steering vector  $\mathbf{s}_t$  exhibits a persymmetric structure, namely it complies with the equation  $\mathbf{s}_t = \mathbf{J}\mathbf{s}_t^*$ .

According to the Neyman-Pearson criterion, the optimum solution to the hypotheses testing problem (3.50), is the Likelihood Ratio Test; but, for the case at hand, it cannot be implemented since total ignorance of the parameters  $\alpha$ ,  $\mathbf{M}$ , and  $\gamma$  is assumed. We resort, instead, to the GLRT decision scheme which is tantamount to replace the unknown parameters with their maximum likelihood estimates under each hypothesis, based upon the entirety of data [68].

Subsequent developments require specifying the complex multivariate probability density function (pdf) of the  $K + 1$  vectors  $\mathbf{y}, \mathbf{y}_1, \dots, \mathbf{y}_K$  under both hypotheses. Previous assumptions imply that the joint pdf can be written as

$$f(\mathbf{y}, \mathbf{y}_1, \dots, \mathbf{y}_K | \mathbf{M}, \gamma, H_0) = \frac{1}{\gamma^{NK} [\pi^N \det(\mathbf{M})]^{K+1}} e^{-\text{tr}(\mathbf{M}^{-1} \mathbf{T}_0)} \quad (3.52)$$

under  $H_0$  and

$$f(\mathbf{y}, \mathbf{y}_1, \dots, \mathbf{y}_K | \mathbf{M}, \alpha, \gamma, H_1) = \frac{1}{\gamma^{NK} [\pi^N \det(\mathbf{M})]^{K+1}} e^{-\text{tr}(\mathbf{M}^{-1} \mathbf{T}_1)} \quad (3.53)$$

under  $H_1$ , where  $\mathbf{T}_0$  and  $\mathbf{T}_1$  are given by

$$\begin{cases} \mathbf{T}_0 = \mathbf{y}\mathbf{y}^\dagger + \frac{1}{\gamma} \mathbf{S} \\ \mathbf{T}_1 = (\mathbf{y} - \alpha \mathbf{s}_t)(\mathbf{y} - \alpha \mathbf{s}_t)^\dagger + \frac{1}{\gamma} \mathbf{S} \end{cases}$$

where

$$\mathbf{S} = \sum_{t=1}^K \mathbf{y}_t \mathbf{y}_t^\dagger$$

. Exploiting the persymmetry of  $\mathbf{M}$  we can write the exponent in (3.52) as

$$\begin{aligned} \text{tr}(\mathbf{M}^{-1} \mathbf{T}_0) &= \text{tr} \left[ \mathbf{M}^{-1} \frac{1}{2} (\mathbf{T}_0 + \mathbf{J} \mathbf{T}_0^* \mathbf{J}) \right] = \\ &= \text{tr} \left[ \mathbf{M}^{-1} \left( \mathbf{R}_p \mathbf{R}_p^\dagger + \frac{1}{\gamma} \mathbf{S}_p \right) \right], \end{aligned} \quad (3.54)$$

where  $\mathbf{R}_p = [\mathbf{r}_e, \mathbf{r}_o]$ ,  $\mathbf{r}_e = \frac{1}{2}(\mathbf{y} + \mathbf{J}\mathbf{y}^*)$ ,  $\mathbf{r}_o = \frac{1}{2}(\mathbf{y} - \mathbf{J}\mathbf{y}^*)$ , and  $\mathbf{S}_p = \frac{1}{2}(\mathbf{S} +$

$\mathbf{J}\mathbf{S}^*\mathbf{J}$ ). Analogously, the exponent of (3.53) can be recast as

$$\begin{aligned}\mathrm{tr}(\mathbf{M}^{-1}\mathbf{T}_1) &= \mathrm{tr}\left[\mathbf{M}^{-1}\frac{1}{2}(\mathbf{T}_1 + \mathbf{J}\mathbf{T}_1^*\mathbf{J})\right] = \\ &= \mathrm{tr}\left\{\mathbf{M}^{-1}\left[(\mathbf{R}_p - \mathbf{s}_t\alpha_p)(\mathbf{R}_p - \mathbf{s}_t\alpha_p)^\dagger + \frac{1}{\gamma}\mathbf{S}_p\right]\right\}\end{aligned}\quad (3.55)$$

with  $\alpha_p = [\alpha_e, \alpha_o]$ ,  $\alpha_e = \frac{1}{2}(\alpha + \alpha^*)$ , and  $\alpha_o = \frac{1}{2}(\alpha - \alpha^*)$ .

The GLRT is the following decision rule

$$\frac{\max_{\gamma} \max_{\alpha} \max_{\mathbf{M} \in \mathcal{P}} f(\mathbf{y}, \mathbf{y}_1, \dots, \mathbf{y}_K | \mathbf{M}, \alpha, \gamma, H_1)}{\max_{\gamma} \max_{\mathbf{M} \in \mathcal{P}} f(\mathbf{y}, \mathbf{y}_1, \dots, \mathbf{y}_K | \mathbf{M}, \gamma, H_0)} \underset{H_0}{\overset{H_1}{>}} G_0, \quad (3.56)$$

which, substituting the multivariate Gaussian density functions (3.52) and (3.53), and maximizing the numerator and the denominator over  $\mathbf{M}$  (under the constraint  $\mathbf{M} \in \mathcal{P}$ ), after some algebra, yields [63]

$$\frac{\min_{\gamma} \left[ \gamma^{\frac{NK}{K+1}} \det\left(\mathbf{R}_p \mathbf{R}_p^\dagger + \frac{1}{\gamma} \mathbf{S}_p\right) \right]}{\min_{\gamma} \min_{\alpha_p} \left\{ \gamma^{\frac{NK}{K+1}} \det\left[(\mathbf{R}_p - \mathbf{s}_t\alpha_p)(\mathbf{R}_p - \mathbf{s}_t\alpha_p)^\dagger + \frac{1}{\gamma} \mathbf{S}_p\right] \right\}} \underset{H_0}{\overset{H_1}{>}} G, \quad (3.57)$$

where  $G$  is a suitable modification of the original threshold. The minimization of the denominator over  $\alpha_p$  can be performed exploiting the results of [69] [formula (2-34)]. Precisely the minimum is achieved when

$$\alpha_p = \frac{\mathbf{s}_t^\dagger \mathbf{S}_p^{-1} \mathbf{R}_p}{\mathbf{s}_t^\dagger \mathbf{S}_p^{-1} \mathbf{s}_t}. \quad (3.58)$$

It follows that the GLRT can be recast as

$$\frac{\min_{\gamma} \left[ \gamma^{-\frac{N}{K+1}} \det\left(\mathbf{I} + \gamma \mathbf{R}_p^\dagger \mathbf{S}_p^{-1} \mathbf{R}_p\right) \right]}{\min_{\gamma} \left\{ \gamma^{-\frac{N}{K+1}} \det\left[\mathbf{I} + \gamma \mathbf{R}_p^\dagger \mathbf{S}_p^{-1} \mathbf{R}_p - \gamma \frac{\mathbf{R}_p^\dagger \mathbf{S}_p^{-1} \mathbf{s} \mathbf{s}^\dagger \mathbf{S}_p^{-1} \mathbf{R}_p}{\mathbf{s}^\dagger \mathbf{S}_p^{-1} \mathbf{s}}\right] \right\}} \underset{H_0}{\overset{H_1}{>}} G, \quad (3.59)$$

where  $\mathbf{I}$  is the  $2 \times 2$  identity matrix. Moreover, letting

$$\Psi_0 = \mathbf{R}_p^\dagger \mathbf{S}_p^{-1} \mathbf{R}_p \quad (3.60)$$

and

$$\Psi_1 = \mathbf{R}_p^\dagger \mathbf{S}_p^{-1} \mathbf{R}_p - \frac{\mathbf{R}_p^\dagger \mathbf{S}_p^{-1} \mathbf{s}_t \mathbf{s}_t^\dagger \mathbf{S}_p^{-1} \mathbf{R}_p}{\mathbf{s}_t^\dagger \mathbf{S}_p^{-1} \mathbf{s}_t}, \quad (3.61)$$

(3.59) can be compactly written as

$$\frac{\min_{\gamma} \left[ \gamma^{-\frac{N}{K+1}} \det(\mathbf{I} + \gamma \Psi_0) \right]}{\min_{\gamma} \left[ \gamma^{-\frac{N}{K+1}} \det(\mathbf{I} + \gamma \Psi_1) \right]} \begin{matrix} H_1 \\ > \\ < \\ H_0 \end{matrix} G. \quad (3.62)$$

In order to minimize the numerator and the denominator of the left hand side of (3.62) we prove the following proposition:

**Proposition 1.** Denote by  $\Psi$  a full rank positive definite  $2 \times 2$  matrix. The solution to the problem

$$\hat{\gamma} = \arg \min_{\gamma} \left[ \gamma^{-\frac{N}{K+1}} \det(\mathbf{I} + \gamma \Psi) \right], \quad (3.63)$$

where  $\arg \min_{\gamma}(\cdot)$  denotes the value of  $\gamma$  which minimizes the argument, is given by

$$\hat{\gamma} = \frac{\sqrt{\Gamma^2 \text{tr}^2(\Psi) + 4N(2K - 2 - N) \det(\Psi)} - \Gamma \text{tr}(\Psi)}{2(2K + 2 - N) \det(\Psi)} \quad (3.64)$$

where  $\Gamma = K + 1 - N$ .

**Proof.** Notice that

$$\left[ \gamma^{-\frac{N}{K+1}} \det(\mathbf{I} + \gamma \Psi) \right] = \left[ \gamma^{-\frac{N}{K+1}} (\det(\Psi) \gamma^2 + \text{tr}(\Psi) \gamma + 1) \right]. \quad (3.65)$$

Evaluating the derivative of the right hand side of the above expression and equating it to zero yields the following equation

$$(2K + 2 - N) \det(\Psi) \gamma^2 + \Gamma \text{tr}(\Psi) \gamma - N = 0 \quad (3.66)$$

The positive solution of (3.66) provides the minimizer  $\hat{\gamma}$ .

Exploiting the result of Proposition 1, we come up with the following expression for the GLRT

$$\frac{\hat{\gamma}_0^{-\frac{N}{K+1}} \det(\mathbf{I} + \hat{\gamma}_0 \Psi_0)}{\hat{\gamma}_1^{-\frac{N}{K+1}} \det(\mathbf{I} + \hat{\gamma}_1 \Psi_1)} \begin{matrix} H_1 \\ > \\ < \\ H_0 \end{matrix} G, \quad (3.67)$$

where

$$\hat{\gamma}_0 = \frac{\sqrt{\Gamma^2 \text{tr}^2(\Psi_0) + 4N(2K - 2 - N) \det(\Psi_0)} - \Gamma \text{tr}(\Psi_0)}{2(2K + 2 - N) \det(\Psi_0)}$$

$$\hat{\gamma}_1 = \frac{\sqrt{\Gamma^2 \text{tr}^2(\Psi_1) + 4N(2K - 2 - N) \det(\Psi_1)} - \Gamma \text{tr}(\Psi_1)}{2(2K + 2 - N) \det(\Psi_1)}$$

Remarkably the GLRT (3.67), referred to in the sequel as the Persymmetric GLRT (P-GLRT), ensures the Constant False Alarm Rate (CFAR) property with respect to both the parameters  $\mathbf{M}$  and  $\gamma^1$ .

### 3.2.2 Performance Analysis

This section is devoted to the performance analysis of the P-GLRT both in terms of false alarm probability ( $P_{FA}$ ) and detection probability ( $P_D$ ). We also compare the performance of the P-GLRT with the ACE, namely the GLRT designed without the assumption of covariance persymmetry. Since closed form expressions for the  $P_{fa}$  and the  $P_d$  are not available for the P-GLRT we evaluate them resorting to standard Monte Carlo techniques based on  $\frac{100}{P_{FA}}$  and  $\frac{100}{P_d}$  independent trials, respectively. Moreover, in order to limit the computational burden, we set  $P_{fa} = 10^{-4}$ . In the simulations we consider an exponentially-shaped disturbance covariance, namely the  $(i, j)^{th}$  entry of the matrix  $\mathbf{M}$  is equal to

$$\mathbf{M}_{i,j} = 2\sigma^2 \rho^{|i-j|},$$

where  $\rho = 0.9$  is the one-lag correlation coefficient and  $\sigma^2$  is the common variance of the disturbance quadrature components. Finally we assume  $\mathbf{s}_t = [1, \dots, 1]^T$ .

In Figure 3.2.2 we show the detection performance of the P-GLRT versus the Signal to Noise Ratio (SNR), i.e.

$$\text{SNR} = |\alpha|^2 \mathbf{s}_t^\dagger \mathbf{M}^{-1} \mathbf{s}_t, \quad (3.68)$$

for  $N = 8$  and several values of  $K$ . The performance of the ACE is plotted too. The curves highlight that for a small number of training data the P-GLRT outperforms the ACE (for instance if  $K = 16$  and  $P_D = 0.9$  the performance

<sup>1</sup>The proof of the CFAR behavior parallels the derivations [64, Appendix B]. The only difference is that the new receiver, under the  $H_0$  hypothesis, exhibits a further scale invariance with respect to a multiplication of the secondary data by a common factor.

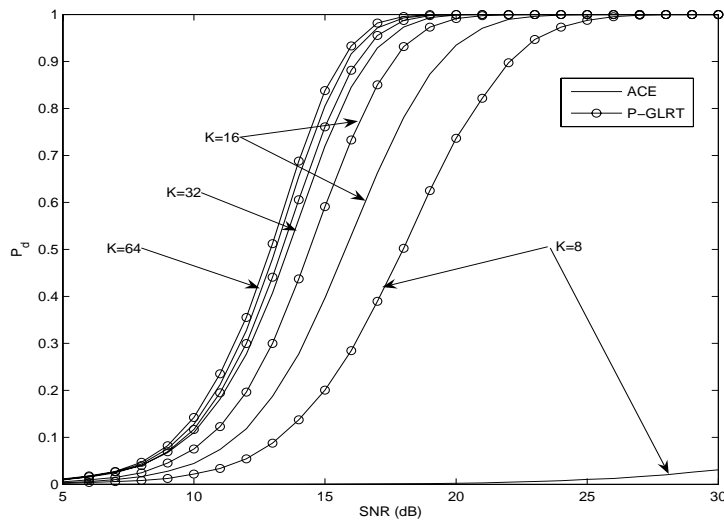


**Figure 2.2.2.**  $P_D$  versus SNR of the P-GLRT (dotted-marked curves) and ACE (solid curves) for  $N = 8$ ,  $P_{FA} = 10^{-4}$ , and  $K$  as a parameter.

gain is about 2.5 dB). However the gain reduces as  $K$  increases and, for  $K = 64$ , the performances of the two receivers are practically coincident. In other words, when there is a sufficient number of training data, it is not necessary to exploit the structural information about the disturbance covariance to obtain a reliable estimate of this parameter [71].



## Chapter 4

# Distributed Aperture Radars

Recent works have shown the benefit of the joint use of distributed aperture radars and waveform diversity [72, 73]. The large baseline of the distributed aperture radar results in improved angular resolution compared to the resolution of a monolithic system, at cost of grating lobes or high side-lobes. The system under consideration is a very sparse array of sub-apertures placed thousands of wavelengths apart. Each sub-aperture of the array transmits a unique waveform, orthogonal to the signals transmitted by the others; to achieve time orthogonality we use pulses that do not overlap in the time domain. Each aperture receives all the transmitted signals, but, due to the orthogonality assumption, each signal can be treated independent of the others. Waveform diversity is achieved using multiple signals characterized by different pulse durations.

A very important issue arising from the work in [72] and [73] is that, due to the very long baseline, both signals and interference sources are not in the far field of the antenna array. For this configuration, the spatial steering vector depends not only on signal *angle* of arrival but also on the *distance* between receiver and target. To take in account this range dependency, some works model the steering vector as a function of the curvature radius of the wave [57], modifying the phase shift contributed to each antenna element. However, as outlined in [72], to take in account the waveform diversity for the interesting case of distributed aperture radars, instead of using phase shifts to model the delay of wave propagation through the array, the processing scheme requires true time delay between the widely distributed antennas. Previous work such as described above has focused on *frequency diversity* to enable orthogonal transmissions from each element in the distributed array. However, frequency

diversity raises the difficult issue of coherent processing across a wide frequency range. In this chapter a system, using an alternative approach based on time orthogonal waveforms with differing pulse durations to achieve diversity, is proposed. Waveform diversity using varying FM rates was proposed in [74] in the context of target tracking. In addition, the distributed radar problem is inherently multistatic with multiple radars illuminating the area of interest, and also receiving and potentially processing all these transmissions. A true development of STAP for distributed apertures will therefore include both monostatic [7] and bistatic configurations [75, 76].

The interference is modeled as a sum of noise and clutter; the clutter contribution is modeled as the sum of several low power interference sources [7], each with a range dependent contribution. A well known problem in bistatic radar [77] is that clutter Doppler center is range dependent due to the relative motion between antennas and interference source. This dependency significantly degrades the achievable performance of the receiver and must be taken in account for effective clutter suppression.

The first goal of this chapter is to develop a new model for waveform diversity for distributed aperture radars with time-orthogonal waveforms. In this regard, this work represents a continuation in the research about waveform diversity for distributed aperture radars and also an effort on the bistatic and multistatic STAP applied to distributed aperture. The time orthogonal waveforms, just like with frequency diversity, allows for independent processing of each transmit-receive combination. A companion paper focuses on the case of time-overlapping transmissions with differing pulse widths [78]. Based on previous results, in this work, we introduce a new waveform diversity model that involves the pulse duration instead of the frequency diversity proposed in [72]. The second goal of this part of the work is to characterize the impact of clutter non-stationarity due to the bistatic problem in the context of waveform diversity. We analyze the effect of the clutter Doppler frequency non-stationarity and the performance improvement achievable applying specific techniques to counteract it. In particular, we use the *Joint Domain Localised* (JDL) algorithm. The JDL algorithm was first introduced by Wang and Cai [79] to transform the data from the space-time domain to the angle-Doppler domain. Adaptive processing is restricted to a localised domain, significantly reducing the degrees of freedom while retaining maximal gain against thermal noise. In developing the JDL algorithm the authors assumed an array of ideal, isotropic point sensors. In such a case, space-time data are transformed to angle-Doppler data using a two dimensional discrete Fourier transform (DFT).

When applying the JDL to measured data a crucial assumption in [79] is invalid: the elements of a real array cannot be point sensors. A more general formulation is in [80] and we resort to that one. This model resorts to a transformation matrix; the formulation made by Cai and Wang coincides with this one in the ideal condition. The transformation matrix is a Kronecker product involving the spatial and temporal steering vectors. The data are converted from the space-time domain to the angle-Doppler domain by the multiplication between this matrix and the data vectors.

The chapter is organized as follows. In Section 4.1 we introduce the system and interference models without taking in account the range dependency of the clutter. In Section 4.2 we introduce the problem of the non-stationarity of the environment and we describe the JDL algorithm applied to our model. In Section 4.3 a brief proof of the CFAR behavior of the developed receiver is provided. Section 4.4 presents numerical simulations of the system of interest.

## 4.1 System Model

The system under consideration is a ground based distributed aperture radar attempting to detect low flying targets. The elements of the array are widely separated from each others and are placed thousand of wavelengths apart. Due to the big distances between elements, both target and interference sources are in the near-field of the antenna array. In fact, given an antenna array of aperture  $D$  operating at wavelength  $\lambda$ , the distance  $R$  to the far-field must satisfy the conditions (3.14) which, using typical values for distributed radars,  $D=200\text{m}$  and  $\lambda=0.03\text{m}$ , imply that the far field distance begins at a distance of approximately 2700km. It is evident that for many practical applications both signals and interference source might not be in the far field. In this case the steering vector depends on both angle and range, while in the far-field model it depends only on the angle of arrival.

The system is composed of  $N$  sub-aperture that are both receiver and transmitter. Each sub-aperture transmits a unique waveform, orthogonal to the others and differentiated on the shape, and receives all the transmitted signals. To achieve orthogonality and waveform diversity, the signals don't overlap in the time domain and the pulse durations are different. Fig. 4.1 presents an example with 3 transmitting elements and 2 pulses per element;  $n$  denotes the transmitting element. The sensors are located in the  $x - y$  plane at the points  $(x_n, y_n)$ ,  $n = 1, \dots, N$  and transmit a coherent stream of  $M$  linear FM pulses, with common frequency  $f_0$ , common pulse repetition interval (PRI)

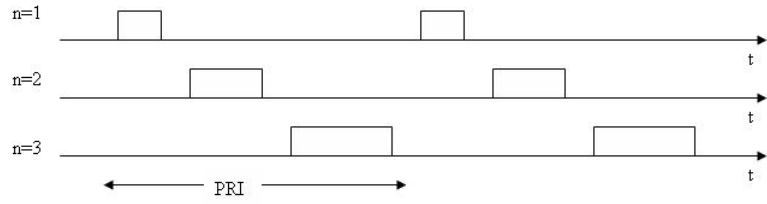


**Figure 4.1:** Time orthogonal signals with different pulse duration and common PRI.

$T_r$ , common bandwidth  $B$  but different pulse durations, that is, the slope of instantaneous frequency varies among the  $N$  transmitted signals. All  $N$  elements receive and process all  $N$  incoming signals, that is, if  $M$  pulses are used in a coherent pulse interval (CPI), the overall return signal over time, space, and waveform can be written as a  $N^2 M$ -length vector.

Due to the orthogonality of the signals, the receiver processes each incoming signal independently from the others and uses true time delay to focus on a look-point  $(X_t, Y_t, Z_t)$ . Denote as  $D_n = \sqrt{(X_t - x_n)^2 + (Y_t - y_n)^2 + (Z_t - z_n)^2}$  the distance between the look point  $(X_t, Y_t, Z_t)$  and the  $n^{\text{th}}$  element. The true time delay used by the receiver  $i$  is [72]

$$\Delta T_i = \frac{\max_p \{D_p\} - D_i}{c}, \quad (4.1)$$

where  $p = 1, \dots, N$  and  $c$  is the speed of light. Delaying the signals using this amount means aligning them in the space domain to the most far element of the array respect of the look-point; in fact, in this way the propagation delay over the array is nullified.

Let us denote by  $\mathbf{y}$  the complex vector of the samples from the range cell where the presence of the useful target is sought (primary data). As in [8] we suppose that a secondary data set  $\mathbf{y}_k$ ,  $k = 1, \dots, K$  is available ( $K \geq N + 1$ ), that each of such snapshots does not contain any useful target echo and exhibits the same covariance matrix as the primary data. The interference is composed by thermal noise and clutter.

The detection problem to be solved can be formulated in terms of the fol-

lowing binary hypotheses test

$$\begin{cases} H_0 : \begin{cases} \mathbf{y} &= \mathbf{c} + \mathbf{n} \\ \mathbf{y}_k &= \mathbf{c}_k + \mathbf{n}_k \quad k = 1, \dots, K \end{cases} \\ H_1 : \begin{cases} \mathbf{y} &= \mathbf{s} + \mathbf{c} + \mathbf{n} \\ \mathbf{y}_k &= \mathbf{c}_k + \mathbf{n}_k \quad k = 1, \dots, K \end{cases} \end{cases} \quad (4.2)$$

where  $\mathbf{s}$  is the useful signal,  $\mathbf{c}$  is the clutter contribution,  $\mathbf{n}$  the noise contribution for the primary data,  $H_0$  is the null hypothesis and  $H_1$  is the useful hypothesis; we use the same notation for the secondary data. Let us explore the signal and the interference models.

#### 4.1.1 Signal model

The signal sent by the  $n^{\text{th}}$  element of the array is

$$x_n(t) = u_n(t)e^{j2\pi f_0 t + j\psi} \quad (4.3)$$

where  $\psi$  is a random phase and  $u_n(t)$  is the complex envelope of the FM pulse given by

$$u_n(t) = \sum_{m=0}^{M-1} u_{pn}(t - mT_r) \quad (4.4)$$

where  $u_{pn}(t)$  is the envelope of the single pulse. The signal sent is reflected by the target and it is received by all the sub-apertures. The signal received at the  $i^{\text{th}}$  receiver is

$$r_{in}(t) = \alpha_t u(t - \tau_{Lin}) e^{j2\pi(f_0 + f_{dn})(t - \tau_{Lin})} \quad (4.5)$$

where  $\alpha_t$  is the amplitude (the phase  $\psi$  is also included),  $f_{dn}$  is the Doppler frequency relative to the  $n^{\text{th}}$  transmission and  $\tau_{Lin}$  is the total trip delay, due to the delay from the  $n^{\text{th}}$  transmitter to the look point  $(X_L, Y_L, Z_L)$  plus the delay from the last one to the  $i^{\text{th}}$  receiver

$$\begin{aligned} \tau_{Lin} = & \frac{\sqrt{(x_n - X_L)^2 + (y_n - Y_L)^2 + Z_L^2}}{c} \\ & + \frac{\sqrt{(x_i - X_L)^2 + (y_i - Y_L)^2 + Z_L^2}}{c}. \end{aligned} \quad (4.6)$$

The received signal (4.5) can be delayed by the amount  $\Delta T_i$ , so that the same range gate is used at all elements. After delaying, the signal is down converted and it becomes

$$\tilde{r}_{in}(t) = \alpha_t u(t - \tau_{Lin} - \Delta T_i) e^{-j2\pi f_0 \tau_{Lin}} e^{j2\pi f_{dn}(t - \tau_{Lin} - \Delta T_i)}. \quad (4.7)$$

Applying matched filter the signal becomes

$$\begin{aligned} s_{in}(t) &= \int_{-\infty}^{+\infty} \tilde{r}_{in}(\tau) u_{pn}^*(\tau - t) d\tau \\ &= \int_{-\infty}^{+\infty} \alpha_t u(\tau - \tau_{Lin} - \Delta T_i) e^{-j2\pi f_0 \tau_{Lin}} e^{j2\pi f_{dn}(\tau - \tau_{Lin} - \Delta T_i)} u_{pn}^*(\tau - t) d\tau \\ &= \alpha_t e^{-j2\pi f_0 \tau_{Lin}} \int_{-\infty}^{+\infty} e^{j2\pi f_{dn}(\tau - \tau_{Lin} - \Delta T_i)} \sum_{m=0}^{M-1} u_{pn}(\tau - \tau_t) u_{pn}^*(\tau - t) d\tau \\ &= \alpha_t e^{-j2\pi f_0 \tau_{Lin}} \sum_{m=0}^{M-1} e^{j2\pi f_{dn} m T_r} \int_{-\infty}^{+\infty} u_{pn}(\beta) u_{pn}^*[\beta - (t - \tau_t)] e^{j2\pi f_{dn} \beta} d\beta \\ &= \alpha_t e^{-j2\pi f_0 \tau_{Lin}} \sum_{m=0}^{M-1} e^{j2\pi f_{dn} m T_r} \chi_n(t - \tau_t, f_{dn}) \end{aligned} \quad (4.8)$$

where  $\tau_t = m T_r + \tau_{Lin} + \Delta T_i$  and  $\chi_n(\tau, f)$  is the ambiguity function relative to the  $n^{th}$  transmission evaluated for the delay  $t - m T_r - \tau_{Lin} - \Delta T_i$ . Note that the total delay  $\tau_{Lin} + \Delta T_i$  is constant with respect to  $i$  and is equal to

$$\begin{aligned} \tau_{Lin} + \Delta T_i &= \frac{D_i}{c} + \frac{D_n}{c} + \frac{\max_p D_p}{c} - \frac{D_i}{c} \\ &= \frac{\max_p D_p + D_n}{c}. \end{aligned} \quad (4.10)$$

The signal determined in this way has to be evaluated for  $t = t_s = m T_r + \tau_{Lin} + \Delta T_i$  and this yields to

$$\begin{aligned} s_{in}(t_s) &= \alpha_t e^{-j2\pi f_0 \tau_{Lin}} \sum_{m=0}^{M-1} e^{j2\pi f_{dn} m T_r} \chi_n(t_s - \tau_t, f_{dn}) \\ &= \alpha_t e^{-j2\pi f_0 \tau_{Lin}} \sum_{m=0}^{M-1} e^{j2\pi f_{dn} m T_r} \chi_n(0, f_{dn}). \end{aligned} \quad (4.11)$$

The generic sample can be written as

$$s_{inm}(t_s) = \alpha_t e^{-j2\pi f_0 \tau_{Lin}} e^{j2\pi f_{dn} m T_r} \chi_n(0, f_{dn}). \quad (4.12)$$

The  $NM \times 1$  steering vector relative to the  $n^{\text{th}}$  transmission is composed by all the samples over the indices  $i$  and  $m$

$$\mathbf{s}_n = \begin{bmatrix} s_{0n0} \\ \vdots \\ s_{(N-1)n0} \\ s_{0n1} \\ \vdots \\ s_{(N-1)n1} \\ s_{0n2} \\ \vdots \\ s_{(N-1)n(M-1)} \end{bmatrix}. \quad (4.13)$$

We can introduce the temporal steering vector  $\mathbf{b}_n(\varpi_n)$  and the spatial steering vector  $\mathbf{a}_n(\vartheta_n)$

$$\mathbf{b}_n(\varpi_n) = \left[ 1, e^{j2\pi\varpi_n}, e^{j2\pi 2\varpi_n}, \dots, e^{j2\pi(M-1)\varpi_n} \right]^T \quad (4.14)$$

$$\mathbf{a}_n(\vartheta_n) = \chi_n(0, f_{dn}) \left[ e^{-j2\pi f_0 \tau_{L0n}}, \dots, e^{-j2\pi f_0 \tau_{L(N-1)n}} \right]^T \quad (4.15)$$

where and

$$\varpi_n = f_{dn} T_r = f_{dn} / f_r \quad (4.16)$$

is the normalised Doppler frequency relative to the  $n^{\text{th}}$  transmission and

$$\vartheta_n = \left[ f_0 \tau_{L0n}, \dots, f_0 \tau_{L(N-1)n} \right]^T \quad (4.17)$$

is the vector of the spatial frequencies relative to the  $n^{\text{th}}$  transmission. Finally, we can express the steering vector as

$$\mathbf{s}_n = \alpha_t \mathbf{b}_n(\varpi_n) \otimes \mathbf{a}_n(\vartheta_n). \quad (4.18)$$

### 4.1.2 Interference model

The interference is due to thermal noise and clutter. Clutter and noise are independent each other.

We assume that the noise components  $\mathbf{n}$  and  $\mathbf{n}_k$ ,  $k = 1, \dots, K$  are independent complex circular Gaussian vectors with zero mean and covariance matrix given by

$$\mathbf{M}_{no} = \mathbb{E}\{\mathbf{nn}^H\} = \mathbb{E}\{\mathbf{n}_k \mathbf{n}_k^H\}. \quad (4.19)$$

As in [7] the clutter is modeled as a sum of many low power sources. An artifact placed in  $(x^l, y^l, z^l)$  reflects the incoming wave given by (4.3). The received signal at the  $i^{th}$  element due to the  $n^{th}$  transmission reflected by the  $l^{th}$  artifact is

$$r_{inl}(t) = A_{nl}u(t - \tau_{inl})e^{j2\pi(f_0 + f_{dnl})(t - \tau_{inl})} \quad (4.20)$$

where  $A_{nl}$  is a random amplitude that includes also the random phase,  $f_{dnl}$  is the Doppler frequency relative to the  $l^{th}$  artifact and the  $n^{th}$  transmission and  $\tau_{inl}$  is the total delay from the  $n^{th}$  transmitter to the  $l^{th}$  artifact plus the delay from the last one to the  $i^{th}$  receiver

$$\tau_{inl} = \frac{\sqrt{(x_n - x^l)^2 + (y_n - y^l)^2 + (z^l)^2}}{c} + \frac{\sqrt{(x_i - x^l)^2 + (y_i - y^l)^2 + (z^l)^2}}{c}. \quad (4.21)$$

The artifact is not necessary located at the look point. Note that the return due to the target not from the look point is included in the clutter sources. The figure 4.2 shows the total trip delay involving the look-point and the one involving the artifact position. The received signal due to the artifact is treated at the same way of the signal due to the target. Making the same analysis of the previous subsection, we can write the final signal due to the artifact, after delaying, down conversion and matched filtering, as

$$c_{inl}(t) = A_{nl}e^{-j2\pi f_0 \tau_{inl}} \sum_{m=0}^{M-1} e^{j2\pi f_{dnl} m T_r} \chi_n(t - m T_r - \tau_{inl} - \Delta T_i, f_{dnl}) \quad (4.22)$$

like the Eq. (4.8); note that the only differences are in the total trip delay  $\tau_{nl}$  used instead of  $\tau_{Lin}$ , in the Doppler frequency  $f_{dnl}$  instead of  $f_{dn}$  and in the

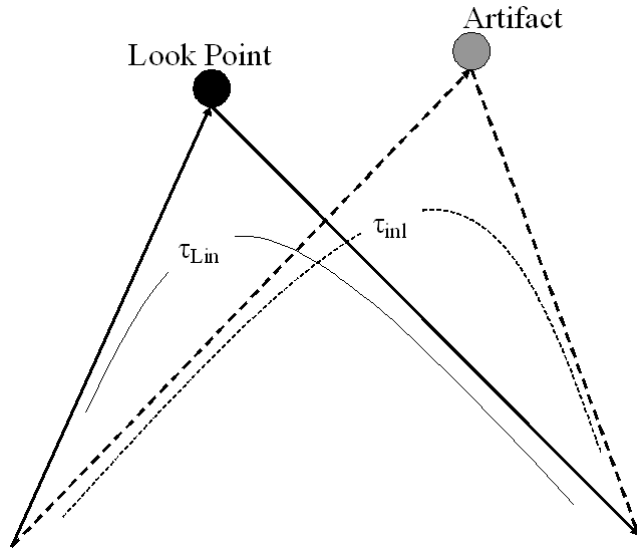


**Figure 4.2:** Total trip delays involving the target (solid line) and the artifact (dashed line).

amplitude  $A_{nl}$  instead of  $\alpha_t$ . The generic element at the  $i^{th}$  receiver, due to the  $n^{th}$  transmission and to  $l^{th}$  artifact and at the  $m^{th}$  pulse can be written as

$$c_{inml}(t) = A_{nl} e^{-j2\pi f_0 \tau_{inl}} e^{j2\pi f_{dnl} m T_r} \chi_n(t - m T_r - \tau_{inl} - \Delta T_i, f_{dnl}) \quad (4.23)$$

We need the covariance matrix of the interference that is unknown. So we estimate it from the environment using the secondary data. Estimating the covariance matrix involves sampling  $c_{inml}$  at the range gates straddling the look point's range gate. The time of the samples is given by

$$t_k = m T_r + \tau_{Lin} + \Delta T_i + k T_s \quad (4.24)$$

where the integer  $k \in [-\lceil K/2 \rceil, \lfloor K/2 \rfloor]$ , where  $\lceil \cdot \rceil$  denotes the rounding off to the lower integer and  $\lfloor \cdot \rfloor$  denotes the rounding off to the higher integer. Sampling the received signal in Eq. (4.22) every  $t_k$  yields to

$$\hat{c}_{inmlk} = A_{nl} e^{-j2\pi f_0 \tau_{inl}} e^{j2\pi f_{dnl} m T_r} \chi_n(\tau_{Lin} - \tau_{inl} + k T_s, f_{dnl}). \quad (4.25)$$

Summing over all the  $N_c$  unambiguous interference sources we can write the sample relative to the  $n^{th}$  transmission, the  $i^{th}$  receiver, the  $m^{th}$  pulse and the

$k^{th}$  secondary range gate

$$\hat{c}_{inmk} = \sum_{l=0}^{N_e-1} A_{nl} e^{-j2\pi f_0 \tau_{inl}} e^{j2\pi f_{dnl} m T_r} \chi_n(\tau_{Lin} - \tau_{inl} + kT_s, f_{dnl}). \quad (4.26)$$

In the same way of the previous subsection we can assemble these samples to obtain the  $NM$ -length steering vector of the clutter  $\mathbf{c}_{nk}$  relative to the  $n^{th}$  transmission and the  $k^{th}$  range cell

$$\mathbf{c}_{nk} = \begin{bmatrix} c_{0n0k} \\ \vdots \\ c_{(N-1)n0k} \\ c_{0n1k} \\ \vdots \\ c_{(N-1)n1k} \\ c_{0n2k} \\ \vdots \\ c_{(N-1)n(M-1)k} \end{bmatrix}. \quad (4.27)$$

### 4.1.3 STAP implementation

We can now implement a space-time-adaptive-processing (STAP) involving the modified sample matrix inversion (MSMI) [11] statistic for target detection. As usual, we estimate the interference covariance matrix from secondary data. Due to the orthogonality the covariance matrix is block-diagonal

$$\hat{\mathbf{M}} = \begin{bmatrix} \hat{\mathbf{M}}_0 & 0 & \dots & 0 \\ 0 & \hat{\mathbf{M}}_1 & \dots & 0 \\ \vdots & \vdots & \ddots & \vdots \\ 0 & 0 & \dots & \hat{\mathbf{M}}_{(N-1)} \end{bmatrix} \quad (4.28)$$

where

$$\hat{\mathbf{M}}_n = \frac{1}{K} \sum_{k=K_i}^{K_s} \mathbf{y}_{nk} \mathbf{y}_{nk}^H$$

is the  $n^{th}$  block of the matrix in (4.28) and is relative to the  $n^{th}$  transmission. The vectors  $\mathbf{y}_{nk}$  are the secondary data collected from the environment for the

$n^{\text{th}}$  transmission; they include the additive Gaussian noise beyond the clutter. The extreme points are  $K_i = -\lceil K/2 \rceil$  and  $K_s = \lfloor K/2 \rfloor$ . Due to the independence of noise and clutter contributions, the matrix is

$$\hat{\mathbf{M}}_n = \hat{\mathbf{M}}_{no} + \hat{\mathbf{M}}_{cn} \quad (4.29)$$

where  $\hat{\mathbf{M}}_{cn}$  is the clutter covariance matrix relative to the  $n^{\text{th}}$  transmission. Note that the noise contribution is independent from the transmission index. Using the matrices defined in (4.28) we can calculate the weight vectors for each bistatic problem

$$\mathbf{w}_n = \hat{\mathbf{M}}_n^{-1} \mathbf{s}_n \quad (4.30)$$

involving the space-time steering vector  $\mathbf{s}_n$ ; these are the space-time steering vector of each transmission, related to the  $N^2M$ -length steering vector of all the transmissions by

$$\mathbf{s} = \begin{bmatrix} \mathbf{s}_0 \\ \mathbf{s}_1 \\ \vdots \\ \mathbf{s}_{(N-1)} \end{bmatrix}. \quad (4.31)$$

Finally, the coherent output statistic is

$$\text{MSMI} = \frac{\left| \sum_{n=0}^{N-1} \mathbf{w}_n^H \mathbf{y}_n \right|^2}{\left| \sum_{n=0}^{N-1} \mathbf{w}_n^H \mathbf{s}_n \right|}. \quad (4.32)$$

where  $\mathbf{y}_n$  is the received signal for the  $n^{\text{th}}$  transmission. Note that the statistic assumes coherence across all the transmissions. This is possible because, unlike the frequency diversity case of [72], all transmissions share a common center frequency.

## 4.2 Clutter non-stationarity

One of the advantages of the orthogonal signaling is the independent treatment of each signal at the receiver. The orthogonality implies that the initial multi-static problem divides into individual bistatic problems and we can use results from the bistatic theory for our treatment. In particular, the non-stationary nature of ground-based clutter in bistatic airborne radar is well known [77]; in this configuration the motion of either transmitter and receiver causes the range dependency of the clutter. In our system the motion is due to the artifact, while

both transmitter and receiver are ground-based and we have to reconsider the bistatic problem in the context of the waveform diversity. As demonstrated in [72] this non-stationarity affects the output of the STAP processor. The basic hypothesis of the space-time adaptive processing is the stationarity of the environment. In fact, the secondary data are collected from range gates close to the one under test and are used to estimate the covariance matrix of the interference; the good quality of this estimation depends on the stationarity of the environment. Due to the range dependency of the clutter Doppler frequency, this hypothesis is no longer valid. So, it is important to study this phenomenon. Fig. 4.3 shows the geometry of the system, where Ar is the artifact,  $\mathbf{v}$  is the artifact velocity,  $\theta_T$ ,  $\theta_R$  and  $\theta_v$  are, respectively, the elevation angles of the transmitter-artifact path, the receiver-artifact path and the artifact velocity,  $\varphi_T$ ,  $\varphi_R$  and  $\varphi_v$  are, respectively, the azimuth angles of the transmitter-artifact path, the receiver-artifact path and the artifact velocity. The coordinate system chosen is a locale coordinate system, with the  $x$  axis coinciding with the baseline and the origin centered in the receiving site; it is not converted into the North-referenced coordinate system introduced in chapter 2. This choice is reasonable while transmitter and receiver are ground-based antennas and thus the locale coordinate system does not change due to position change of the antennas. Note that each clutter source of the ball has the same velocity vector  $\mathbf{v}$ . The direction of the interference sources is fixed and determined by the angles  $\theta_v$  and  $\varphi_v$ . The clutter Doppler frequency due to the motion is

$$f_D = f_{Dx} + f_{Dy} + f_{Dz} \quad (4.33)$$

where

$$f_{Dx} = \frac{\mathbf{v} \cos \theta_v \cos \varphi_v [\cos \theta_t \cos \varphi_t + \cos \theta_r \cos \varphi_r]}{\lambda} \quad (4.34)$$

$$f_{Dy} = \frac{\mathbf{v} \cos \theta_v \sin \varphi_v [\cos \theta_t \sin \varphi_t + \cos \theta_r \sin \varphi_r]}{\lambda} \quad (4.35)$$

$$f_{Dz} = \frac{\mathbf{v} \sin \theta_v [\sin \theta_t + \sin \varphi_r]}{\lambda}. \quad (4.36)$$

The threesome transmitter/receiver/scatterer Ar identifies the bistatic plane; so, for each couple transmitter/receiver there is a different plane. It is detected by the couple of axes  $x - y_b$  and is characterized by the elevation angle  $\theta_b$  respect of the reference  $x - y$ . The isorange contour, which lies in this plane, is shown in the Fig. 4.4; it is an ellipse with foci the transmitter and the receiver, major axis  $a$  and minor axis  $b = \sqrt{a^2 - L^2/4}$  where  $L$  is the distance between the transmitter and the receiver. We can use the points of this ellipse to evaluate the



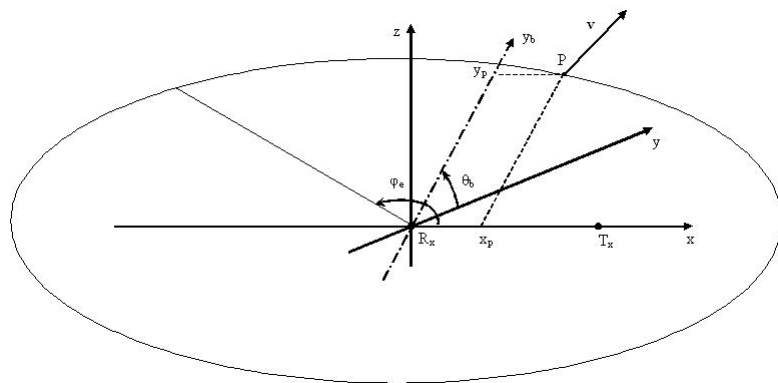


**Figure 4.4:** Bistatic plane with bistatic ellipse.

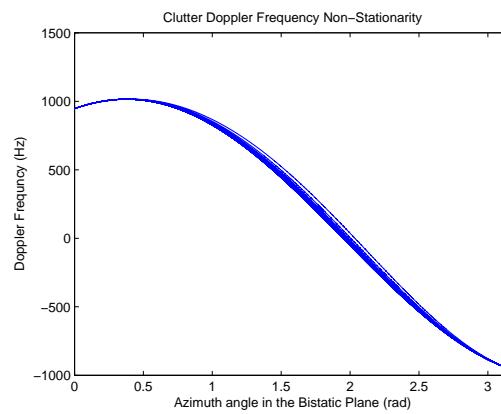


**Figure 4.5:** Clutter Doppler frequency plotted for different range cells. It is evident the non-stationarity of this feature of the clutter.

improvement achievable using it in non-stationary environments [79, 83, 84]. References [83, 84] are the first which studied the need of the limited training-data size of the localized adaptive processing in non-homogeneous and non-stationary environments; they also have shown that it outperforms the fully adaptive processing in these particular cases. Their authors use a two dimensional DFT to convert the data from the space-time domain to the angle-Doppler one. This formulation is possible assuming that the receiving antenna is an equi-spaced linear array of isotropic, ideal, point sensors. When applying the JDL algorithm to real systems, this crucial assumption is no longer valid; the elements of a real array cannot be point sensors. Furthermore, the assumption of linear equi-spaced array is restrictive [80]. Both the two hypotheses can not be applied to the case under consideration of distributed aperture radars. We need to resort to a more general formulation [80].

The JDL algorithm has also a practical implication; a system with  $N$  elements and  $M$  pulses per coherent processing interval (CPI) needs all the  $NM$  degrees of freedom to estimate the interference covariance matrix with the aim of minimizing the expected squared error with respect to the desired signal [85]. In practice, an accurate estimate requires about  $2NM$  to  $3NM$  independent, identically distributed (i.i.d.) secondary data samples [86]. Obtaining such a large number of i.i.d. samples is difficult, if not impossible in some situations. Furthermore, even if the required samples are available, the computation expense is very high. So, reducing the domain dimensionality makes practicable the processor in some situations.

Using the JDL algorithm the number of adaptive unknowns is reduced from  $NM$  in the original domain to  $\eta_a \eta_d$  in the angle-Doppler domain, where  $\eta_a$  and  $\eta_d$  are, respectively, the number of angle bins and Doppler bins chosen; Fig. 4.6 presents a pictorial view of the processing scheme, where the bin marked as ‘‘Signal’’ indicates the target location in angle-Doppler domain. As in [80] we can convert the samples using a transformation matrix  $\mathbf{T}_n$  for each transmission. In general the transformation from the space-time domain to the angle-Doppler domain is an inner product with a space-time steering vector. The transformation matrix for the  $n^{\text{th}}$  transmission is defined as

$$\mathbf{T}_n = \mathbf{b}_n(\boldsymbol{\Omega}_n) \otimes \mathbf{a}_n(\boldsymbol{\Theta}_n) \quad (4.38)$$

where the vector  $\boldsymbol{\Omega}_n$  is the vector of Doppler frequencies normalized by the PRF, centered at the Doppler of the target and spaced by  $1/M$  and  $\boldsymbol{\Theta}_n$  is the vector of the spatial frequencies for the different angles of arrivals; here we

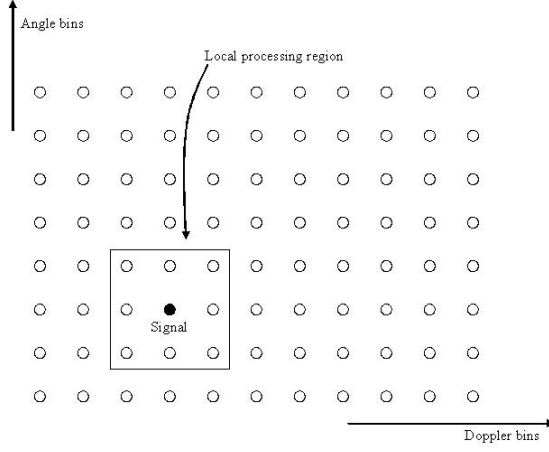


**Figure 4.6:** Localized processing region in angle-Doppler domain for  $\eta_a = \eta_d = 3$ .

assume an angle variation in azimuth equal to

$$\Delta(\varphi) = \pi/N$$

and we need to evaluate the relative propagation delays from point defined by the new angle. Each element of the  $N$ -length vector  $\Theta_n$  has to be evaluated considering the round trip delay from the  $n^{\text{th}}$  transmitter to the  $i^{\text{th}}$  receiver through the new look point defined from  $(X_L, Y_L, Z_L)$  changing only the azimuth angle by the amount  $\pi/N$ ; the point is detected in the space by the same elevation angle  $\theta_t$  of the target and the same distance from the origin of coordinates system to the target. The transformation matrix is so defined

$$\mathbf{T}_n = [\mathbf{b}_n(\varpi_{n(-ai)}), \dots, \mathbf{b}_n(\varpi_{n(0)}), \dots, \mathbf{b}_n(\varpi_{n(ai)})] \otimes [\mathbf{a}_n(\vartheta_{n(-Di)}), \dots, \mathbf{a}_n(\vartheta_{n(0)}), \dots, \mathbf{a}_n(\vartheta_{n(Di)})] \quad (4.39)$$

where

$$ai = \left\lceil \frac{\eta_a}{2} \right\rceil \quad Di = \left\lceil \frac{\eta_d}{2} \right\rceil \quad (4.40)$$

and

$$\varpi_{n(h)} = \frac{f_{dn}}{f_r} + \frac{h}{M} \quad \vartheta_{n(h)} = [f_0 \tau_{L0n(h)}, \dots, f_0 \tau_{L(N-1)n(h)}]^T \quad (4.41)$$

where  $\tau_{Lin(h)}$  is the delay for the path from the  $n^{th}$  transmitter to the  $i^{th}$  receiver through the point which azimuth angle is  $\varphi_i + (h\pi)/N$  and which elevation angle is the same as the target. For example, if  $\eta_h=3$  and  $\eta_d=3$  this matrix is

$$\begin{aligned} \mathbf{T}_n &= [\mathbf{b}_n(\varpi_{n(-1)}), \mathbf{b}_n(\varpi_{n(0)}), \mathbf{b}_n(\varpi_{n(1)})] \otimes \\ &\otimes [\mathbf{a}_n(\vartheta_{n(-1)}), \mathbf{a}_n(\vartheta_{n(0)}), \mathbf{a}_n(\vartheta_{n(1)})] \end{aligned} \quad (4.42)$$

where

$$\begin{aligned} \varpi_{n(-1)} &= \frac{f_{dn}}{f_r} - \frac{1}{M} \\ \varpi_{n(1)} &= \frac{f_{dn}}{f_r} + \frac{1}{M} \\ \vartheta_{n(-1)} &= [f_0 \tau_{L0n(-1)}, \dots, f_0 \tau_{L(N-1)n(-1)}]^T \\ \vartheta_{n(+1)} &= [f_0 \tau_{L0n(+1)}, \dots, f_0 \tau_{L(N-1)n(+1)}]^T \end{aligned}$$

We can now define the vectors in the angle-Doppler domain using the matrix  $\mathbf{T}$  defined above. The relevant transformation is a pre-multiplication with  $(NM \times \eta_a \eta_d)$  transformation matrix  $\mathbf{T}_n$ . The steering vector and the received signal for the  $n^{th}$  transmission in the angle-Doppler domain are respectively

$$\mathbf{s}_{naD} = \mathbf{T}_n \mathbf{s}_n \quad (4.43)$$

$$\mathbf{y}_{naD} = \mathbf{T}_n \mathbf{y}_n \quad (4.44)$$

where the subscript  $aD$  denotes the vector in the angle-Doppler domain. At the same way we can convert the secondary data in the angle-Doppler domain

$$\mathbf{y}_{nkaD} = \mathbf{T}_n \mathbf{y}_{nk} \quad (4.45)$$

needed to evaluate the covariance matrix of the interference in the angle-Doppler domain

$$\hat{\mathbf{M}}_{naD} = \frac{1}{K} \sum_{k=K_i}^{K_s} \mathbf{y}_{nkaD} \mathbf{y}_{nkaD}^H \quad (4.46)$$

and the weight vector

$$\mathbf{w}_{naD} = \hat{\mathbf{M}}_{naD}^{-1} \mathbf{s}_{naD}. \quad (4.47)$$

We can now evaluate the decision statistic in the angle-Doppler domain as like as in (4.32) for the space-time domain

$$\text{MSMI}_{aD} = \frac{\left| \sum_{n=0}^{N-1} \mathbf{w}_{naD}^H \mathbf{y}_{naD} \right|^2}{\left| \sum_{n=0}^{N-1} \mathbf{w}_{naD}^H \mathbf{s}_{naD} \right|^2}. \quad (4.48)$$

In Fig. 4.7 the block diagram of the JDL transformation for the  $n^{\text{th}}$  is shown.

### 4.3 CFAR behavior

We now show that the MSMI test statistic developed in Sec. 4.1 is independent of the true interference covariance matrix under hypotheses  $H_0$  and this gives it a constant false alarm rate.

The interference is composed by two contributions, clutter and noise. As reported previously, the noise is Gaussian colored noise with zero mean and covariance matrix  $\mathbf{M}_{no}$  and this holds for each transmission. The clutter term is characterized by a Gaussian distribution with zero mean and covariance matrix  $\mathbf{M}_{cn}$  for each transmission [87]. The two contributions are uncorrelated, as reported in Eq. (4.29), for each transmission. We can conclude that the interference contribution  $\mathbf{h}_n = \mathbf{c}_n + \mathbf{n}_n$  is a Gaussian random vector with zero mean and covariance matrix  $\mathbf{M}_n$ . Let now be  $\mathbf{z}_n = \mathbf{M}_n^{-1/2} \mathbf{y}_n$  the whitened data vector and  $\mathbf{r}_n = \mathbf{M}_n^{-1/2} \mathbf{s}_n$  the “whitened” steering vector; the test statistic (4.32) can be written as

$$\frac{\left| \sum_{n=0}^{N-1} \mathbf{r}_n^\dagger \mathbf{M}_n^{1/2} \hat{\mathbf{M}}_n^{-1} \mathbf{M}_n^{1/2} \mathbf{z}_n \right|^2}{\left| \sum_{n=0}^{N-1} \mathbf{r}_n^\dagger \mathbf{M}_n^{1/2} \hat{\mathbf{M}}_n^{-1} \mathbf{M}_n^{1/2} \mathbf{r}_n \right|^2} = \frac{\left| \sum_{n=0}^{N-1} \mathbf{r}_n^\dagger \tilde{\mathbf{M}}_n^{-1} \mathbf{z}_n \right|^2}{\left| \sum_{n=0}^{N-1} \mathbf{r}_n^\dagger \tilde{\mathbf{M}}_n^{-1} \mathbf{r}_n \right|^2}, \quad (4.49)$$

where the matrix  $\tilde{\mathbf{M}}_n = \mathbf{M}_n^{-1/2} \hat{\mathbf{M}}_n \mathbf{M}_n^{-1/2}$  is subject to the complex Wishart distribution with parameter  $K$ ,  $NM$  and  $\mathbf{I}$ , which is denoted as  $CW(K, NM; \mathbf{I})$  [88].

Now we define a unitary transform that rotates the whitened signal vector into the first elementary vector

$$b\mathbf{e}_n = \mathbf{U}_n^\dagger \mathbf{r}_n, \quad \mathbf{e}_n = [1, 0, \dots, 0]^\dagger. \quad (4.50)$$

The first column of  $\mathbf{U}_n$  is the vector  $\mathbf{r}_n$  and the others  $(NM - 1)$  ones form an arbitrary orthonormal basis of the orthogonal complement of the subspace

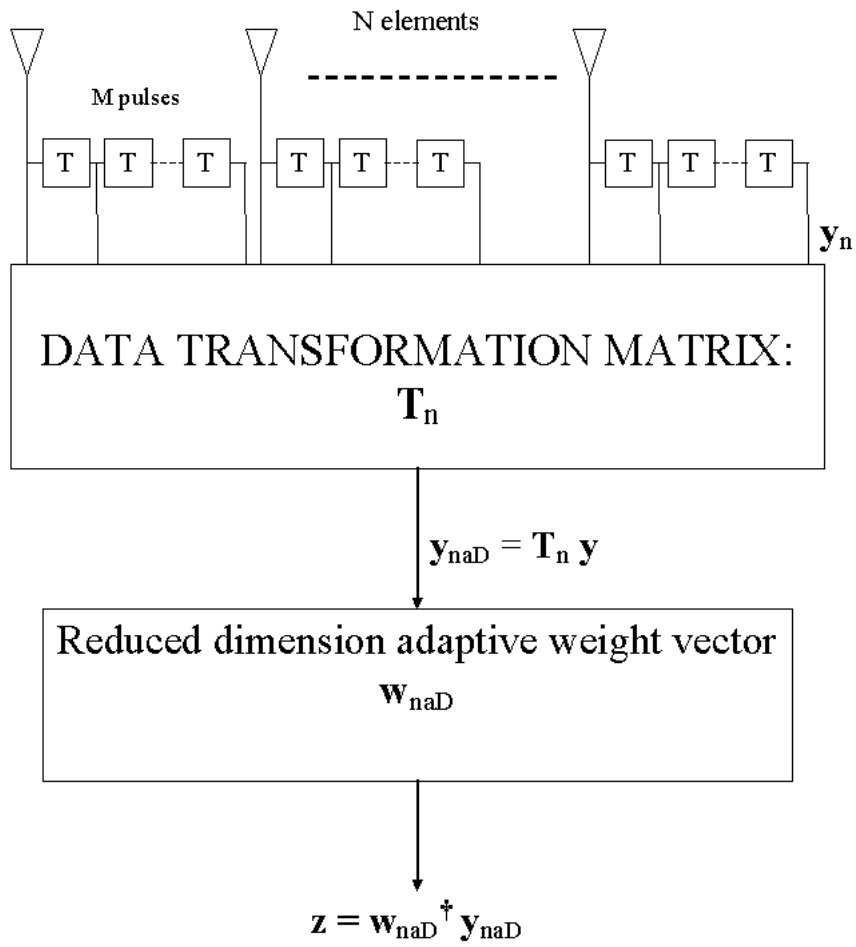


**Figure 4.7:** Block diagram of the JDL transformation for the  $n^{\text{th}}$  transmission. Only the primary data are considered.

spanned by the vector  $\mathbf{r}_n$ . Then the test (4.49) becomes

$$\frac{\left| \sum_{n=0}^{N-1} b \mathbf{e}_n^\dagger \mathbf{U}_n^\dagger \tilde{\mathbf{M}}_n^{-1} \mathbf{U}_n \mathbf{g}_n \right|^2}{\left| \sum_{n=0}^{N-1} b^2 \mathbf{e}_n^\dagger \mathbf{U}_n^\dagger \tilde{\mathbf{M}}_n^{-1} \mathbf{U}_n \mathbf{e}_n \right|} = \frac{\left| \sum_{n=0}^{N-1} b \mathbf{e}_n^\dagger \mathbf{B}_n^{-1} \mathbf{g}_n \right|^2}{\left| \sum_{n=0}^{N-1} b^2 \mathbf{e}_n^\dagger \mathbf{B}_n^{-1} \mathbf{e}_n \right|} \quad (4.51)$$

where  $\mathbf{g}_n = \mathbf{U}_n^\dagger \mathbf{z}_n$  and  $\mathbf{B}_n = \mathbf{U}_n^\dagger \tilde{\mathbf{M}}_n \mathbf{U}_n$ . The vector  $\mathbf{g}_n$  is Gaussian distributed with zero mean and covariance matrix  $\mathbf{I}$  under  $H_0$  hypotheses and the matrix  $\mathbf{B}_n$  is distributed  $CW(K, NM; \mathbf{I})$ .

The actual covariance matrix does not appear in the test statistic or in the underlying density functions; the test statistic is so independent of both the structure and the level of the true covariance and so it is a CFAR test.

We can repeat the analysis made above for the test statistic defined in (4.32) for the one defined in (4.48) applying the JDL algorithm to the classic MSML. The only difference is that the vectors are now defined by a linear transformation of the initial vectors, as reported in Eq. (4.43), (4.44), (4.45). This transformation does not change the statistical distribution of the vectors; therefore we can repeat the previous analysis substituting the vectors  $\mathbf{y}_n$  and  $\mathbf{s}_n$  and the matrix  $\hat{\mathbf{M}}_n$  respectively with  $\mathbf{y}_{naD}$ ,  $\mathbf{s}_{naD}$  and  $\hat{\mathbf{M}}_{naD}$ . So the CFAR behavior holds also for this test statistic.

## 4.4 Numerical simulations

In this section we present the results of numerical simulations using the models developed in Sec. 4.1 and in Sec. 4.2. Results reported in [72] had demonstrated the importance of the use of waveform diversity for distributed aperture radars in order to deal with the problem of the grating lobes. Since the steering vectors are range dependent, the beampattern is a plot of the signal strength versus the transverse coordinate. The range dependency implies a small decay in the grating lobes level further away from the target location  $X_t$ . However, this decay is inadequate for target detection. Using frequency diversity proposed in [72] it is possible to eliminate the grating lobes. We expect that using waveform diversity model the grating lobes are smaller than that achievable with frequency diversity model and a clear target identification is preserved. We expect also that the application of the JDL algorithm, which takes in account for the non-stationarity of the environment, improves the achievable performances in terms of an improved detection probability.

The experiments use the common parameters shown in the Table 4.1. In

Parameter	Value	Parameter	Value
N	9	M	3
$T_{MIN}$	$10\mu s$	$T_{MAX}$	$100\mu s$
B	10MHz	$f_0$	10GHz
PRI	$T_r$	INR	50dB
Target Velocity	50m/s	Target SNR	10dB
$X_t$	476.9158m	$Y_t$	-59.9566m
$Z_t$	200km	$N_c$	200

**Table 4.1:** Common parameters for the simulations.

the table  $T_{MIN}$  and  $T_{MAX}$  represent the minimum and the maximum pulse duration respectively; the pulse repetition time (PRI) is

$$T_r = 5 \sum_{n=0}^{N-1} T(n), \quad (4.52)$$

where  $T(n)$  is the  $n^{th}$  pulse duration equal to

$$T(n) = T_{MIN} + n \frac{T_{MAX} - T_{MIN}}{N - 1}. \quad (4.53)$$

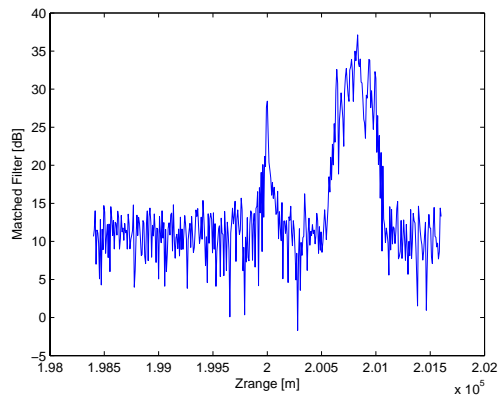
The array elements are uniformly distributed in the  $x - y$  plane on a square  $200m \times 200m$  grid. INR is the Interference-to-Noise Ratio.

#### 4.4.1 Need for waveform diversity

In this subsection we report an analysis obtained using the model without the application of the JDL algorithm; the decision statistic used is reported in (4.32). These first results allow us to analyze the impact of the proposed waveform diversity model on the system performances without the improvement achievable with the JDL algorithm. In this way it is possible to understand how the proposed model counters the grating lobes and which is the corresponding detection capability.

Fig. 4.8 plots the output of the matched filter along the radial  $z$ -direction. The target is at a range of 200km in the radial  $z$ -direction. The output shows low grating lobes for many values of the range, but it is very asymmetric due to the range dependency of the clutter that affects the estimation of the covariance matrix. Fig. 4.9 plots similar results along the transverse  $x$ -direction. The target is at a range of 476.9158m in the transverse  $x$ -direction. The output of

the matched filter is more regular and symmetric than the one in the radial direction.



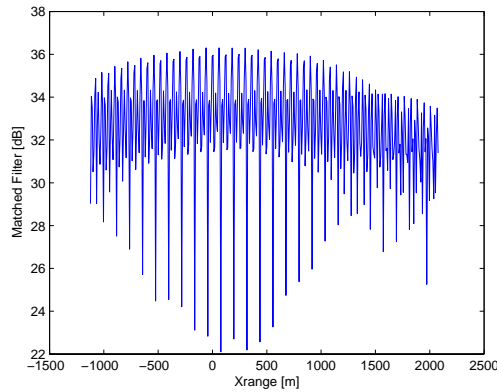
**Figure 4.8:** Matched filter processing along the radial Z-direction. Includes interference.

Fig. 4.10 plots the modified sample matrix inversion (MSMI) statistic over the radial  $z$ -direction. All interference range cells are used to estimate the interference covariance matrix. The target is very clearly identified, even using only 3 pulses and 9 antenna elements, due to the narrow lobe centered at 200km in range, that is, at the target range. Fig. 4.11 plots similar results along the transverse  $x$ -direction. In this case the target is not clearly identifiable and the system shows a performance decay.

These plots show that the waveform diversity model used allows a good target detection in the radial  $z$ -direction and a good response to the grating lobes [89].

#### 4.4.2 Need for JDL algorithm

In this subsection we analyze the performance improvements achievable introducing the JDL algorithm in the model. For this purpose a comparison between the decision statistic obtained using the waveform diversity (4.32) and the one obtained applying the JDL algorithm (4.48) is conducted. In this way it is possible to study the benefits due to the use of the reduced dimension domain. At the same time we also compare these performances with that ones achievable using the frequency diversity model in [73] to analyze the achievable improve-



**Figure 4.9:** Matched filter processing along the transverse X-direction. Includes interference.

ments with respect to this signal model. In the following, we indicate the decision statistic in [73] as **F-MSMI** (Frequency MSMI), the one obtained using the waveform diversity model in (4.32) as **W-MSMI** (Waveform MSMI) and the last one obtained introducing the JDL algorithm in (4.48) as **JW-MSMI** (JDL Waveform MSMI).

Fig. 4.12 shows the probabilities of detection versus the Signal to Interference plus Noise ratio SINR

$$\text{SINR} = \sum_{n=0}^{N-1} |\alpha_n|^2 \mathbf{s}_n \mathbf{M}_n^{-1} \mathbf{s}_n \quad (4.54)$$

achievable with the three decision statistics. The solid line represents the probability of detection of F-MSMI, the star-marked the probability of detection of W-MSMI and the dashed line the probability of detection of JW-MSMI. It is evident the improvement achievable. The JW-MSMI outperforms the others and the W-MSMI is better than the F-MSMI. In particular, for probability of detection equal to 0.9 the performance gain between JW-MSMI and W-MSMI is around 4 dBs and around 8 dBs between JW-MSMI and F-MSMI. The behaviour of the curves highlights that the range dependency of the covariance matrix limits the achievable performance. It is remarkable that the gain between JW-MSMI and W-MSMI is achieved with a low dimension reduction; in fact, the dimension of the steering vectors is 27 in the space-time domain and 9 in the angle-Doppler domain. It is evident that all the statistics need

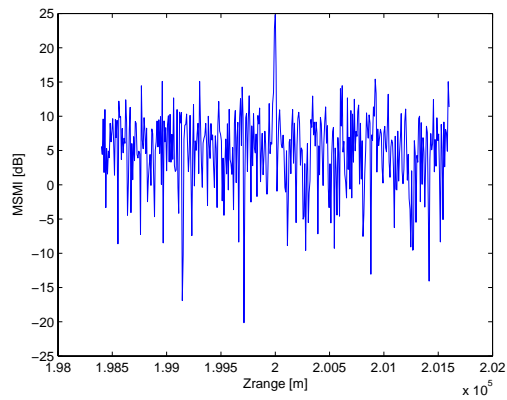


**Figure 4.10:** MSMI statistic along the radial Z-direction. Includes interference.

a low SINR to achieve a good probability of detection; the distributed aperture radars use all the incoming signals and for this reason the needed SINR is lower than the one in a monostatic or bistatic radar [90].

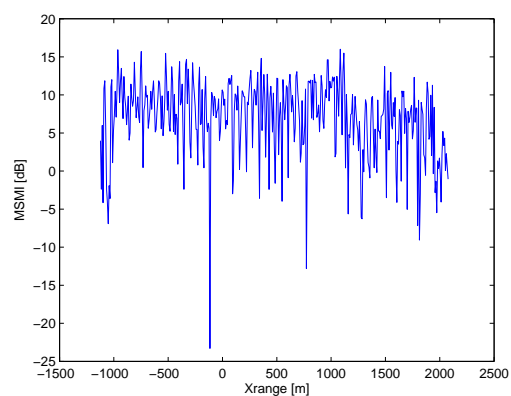


**Figure 4.11:** MSMI statistic along the transverse X-direction. Includes interference.

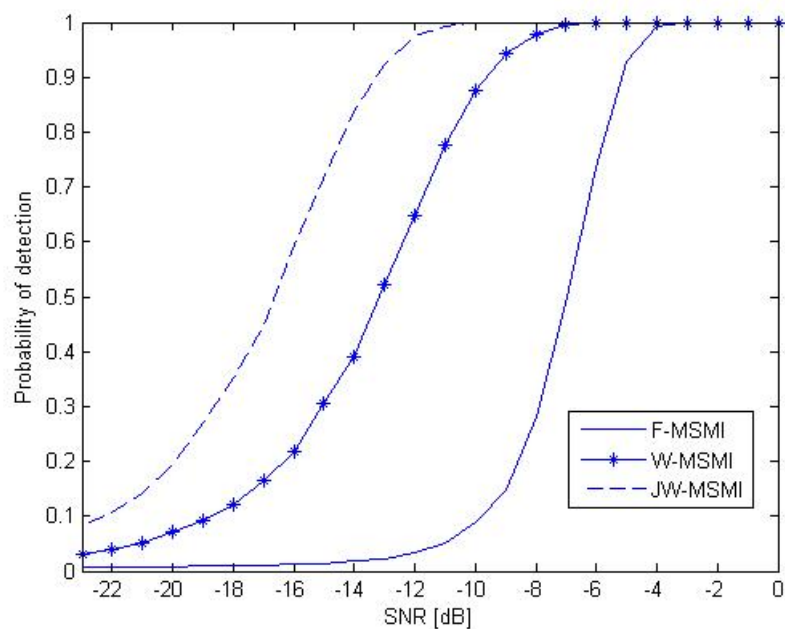


**Figure 4.12:** Probability of detection versus the SNR. The solid line represents the F-MSMI; the star-marked the W-MSMI; the dashed one the JW-MSMI.



# Conclusions

In this thesis, the space-time adaptive processing in presence of mismatches has been analyzed. It is based on multiple receiving elements and multiple pulses, used to detect a target in presence of disturbance; the disturbance is always composed by thermal noise and may contain clutter and/or jamming. The mismatches considered are mutual coupling, near-field effects, insufficient size of the sample support and non-stationarity of the environment. The mutual coupling, due to the physical dimension of the antenna elements, consists of the reflection and re-irradiation of part of the impinging energy from an antenna to the others; all the elements of the array receive the contribution from the neighbors together to the wave scattered from the target. It is absent only in ideal condition of point antenna. The near-field effects are not always present, while they are caused by the dimension of the array; if the array has high dimension, the distance for the application of the far-field model is very high and in many practical situations both target and interference sources can not be considered in the far-field if the array. The space-time adaptive processing uses data, called secondary data, from range gates near to the one under test to estimate the unknown interference covariance matrix. The sample support has to be enough big to ensure a good estimation; the number of range gates used for the estimate has to be very bigger than the number of antenna elements in the array. The estimate operation is possible until the environment is stationary, i.e. the interference samples from range gates different from the one under test share the same statistical characteristics. This hypothesis is no more valid in some scenarios, like the bistatic or multistatic radars due to the relative motion between interference sources and antenna elements.

Starting from two receivers present in the open literature, the Generalized Likelihood Ratio Test and the Adaptive Matched Filter, both derived under ideal conditions of absence of mutual coupling, applicability of far-field model and stationarity of the environment, new adaptive radar detectors are designed and analyzed. In particular, new GLRT-based detectors, both one-step and

two-step, are developed in conditions of mutual coupling and near-field effects for uniform linear array; a one-step GLRT is developed for uniform linear array also exploiting the characteristic of the environment to improve the radar performance in presence of a small number of secondary data. Finally, a time-orthogonal signaling scheme in presence of non-stationarity of the environment and near-field effects is developed for distributed aperture radars. This two kinds of arrays differ basically on their dimensions; the uniform linear array is a one-dimension array with uniform interelement spacing, while the distributed aperture radars are spatial arrays with interelement spacing equal to thousands of the operating wavelength.

All the quoted detectors are analyzed in terms of probability of detection versus the Signal-to-Interference-plus-Noise Ratio and are compared with the conventional receivers. The performance analysis is conducted through Monte Carlo simulations. It is useful to discuss shortly the different receivers developed, before conclude the work taking in account for all the quoted problems.

First, the one-step and two-step GLRT detectors for uniform linear arrays in presence of mutual coupling and near-field effects are developed and analyzed; they outperform the classic Kelly's receiver and the AMF in some situations of practical interest. Even if the two-step GLRT-based detectors are less time consuming than the one-step GLRT-based receivers, they achieve the same performance level for the chosen values of the parameters. Moreover the importance of compensating both the mutual coupling and the near-field effects has been analyzed showing that, for the considered scenarios, the mutual coupling is the predominant source of performance degradation.

Second, it has been considered the synthesis and the analysis of an adaptive detector for signals, known up to a scaling factor, embedded in partially-homogeneous disturbance with persymmetric covariance matrix. At the design stage it has been devised the P-GLRT, which ensures the CFAR property with respect to the disturbance parameters. At the analysis stage the performance of the new receiver, also in comparison with the unstructured GLRT which does not exploit the covariance persymmetry, are analyzed. The results have shown that the new receiver outperforms the unstructured GLRT in the presence of a small number of secondary data, and achieves the same performance level when the cardinality of the training set is sufficiently large. In conclusion, as shown by [64] with reference to an homogeneous environment, persymmetry turns out to be a suitable means to operate in the presence of a small number of training data even when a scale mismatch between primary and secondary data is present.

---

Finally, the design and the analysis of a time-orthogonal waveform diversity model for distributed aperture radars has been considered. The signal model uses waveform diversity applied to distributed aperture radars; the chosen signals have different pulse durations and they do not overlap in time to achieve respectively waveform diversity and time-orthogonality. The orthogonality allows to independent treatment of the signals at each receiver making simple the decision statistic. Based on the realization that both target and interference sources are in the near-field of the antenna array, this paper uses a data model based on true time delays. Furthermore, due to the relative motion between clutter and antennas, the clutter is not stationary. We took in account for this range dependency of the interference sources converting the data from space-time domain to angle-Doppler domain with the application of the Joint Domain Localized (JDL) algorithm to the case of interest. The detection capability of the new receiver is very good in the radial direction, where the MSMI statistic shows a narrow and high lobe centered at the target range, while in the transverse direction the system shows a performance decay due to a test statistic without high lobes. The signaling scheme counteracts the grating lobes for many values of the range, but it is very asymmetric due to the range dependency of the interference. The probabilities of detection, analyzed through Monte Carlo techniques, show that the new processor outperforms the a detector, present in the open literature, based on a frequency diversity model; furthermore, they show also the influence of the range dependency of the interference covariance matrix; the performances may be even improved taking in account for this non-stationarity.

All the reported results show that the space-time adaptive processing are sensitive to the quoted problems. It is thus of primary importance to take in account for the non ideality conditions of many situations of practical interest. The developed detectors are capable to detect a target in environment affected by interference with good achievable performance, outperforming in all the considered scenarios the conventional receivers.

Some considerations may be made for possible future research tracks. One idea lies in developing detectors more general than those presented in this work. First, the extension to the case of unknown (or partially known) mutual coupling matrix as well as the generalization of the near-field model to array geometries more complicated than the uniform linear array are interesting points of view that enlarges the condition of applicability of the developed detectors. Second, the time-orthogonal signaling scheme developed in chapter 3 is based on the orthogonality of the waves. It is interesting to analyze the ef-

fect of the loss of the orthogonality. It is evident that the estimated covariance matrix is no more block-diagonal and that some terms are different from zero outside of the principal diagonal. Another idea is the development of a new signaling scheme, differentiating the waveforms on more than one parameter, using for example the pulse duration and the PRI. Finally a further analysis, based on real data, is necessary for the final validation of the approaches.

# Bibliography

- [1] M. I. Skolnik: *Radar Handbook*, New York: McGraw-Hill, 1-st ed., 1970.
- [2] A. Farina and G. Galati: *Surveillance Radars: State of the Art, Research and Perspectives*, *Alta Frequentia*, vol. LIV, no. 4, pp. 261-277, 1985.
- [3] V. S. Chernyak: *Fundamentals of Multisite Radar Systems: Multistatic Radars and Multiradar Systems*, Gordon and Braech Science Publishers, 1998.
- [4] N. J. Willis: *Bistatic Radar*, Technology Service Corporation, 2-nd ed., 1995.
- [5] A. Prentice: *A Digitally Beamformed Phased Array Receiver for Tactical Bistatic Radar*, Proceedings of IEE Colloquim on 'Active & Passive Components for phased Array system', 1992, London (UK), pp. 11/1-4, April 24 1992.
- [6] N. A. Goodman and D. Bruyere: *Optimum and Decentralized Detection for Multistatic Airborne Radar*, *IEEE Transactions on Aerospace and Electronic Systems*, vol. 43, no. 2, pp. 806-813, April 2007.
- [7] J. Ward: *Space-time adaptive processing for airborne radar*, Tech. Rep. F19628-95-C-00002, MIT Lincoln Laboratory, December 1994.
- [8] E. J. Kelly: *An Adaptive Detection Algorithm*, *IEEE Transactions on Aerospace and Electronic Systems*, vol. AES-22, no. 1, pp. 115-127, March 1986.
- [9] S. Bose and A. O. Steinhardt: *A Maximal Invariant Framework for Adaptive Detection with Structured and Unstructured Covariance Matrices*,

- 
- IEEE Trans. on Signal Processing, Vol. 43, no. 3, pp. 2164-2175, September 1995.
- [10] S. Bose and A. O. Steinhardt: *Optimum array detector for a weak signal in unknown noise*, IEEE Transactions on Aerospace and Electronic Systems, vol. 32, no. 3, pp. 911 - 922, July 1996.
- [11] F. C. Robey, D. R. Fuhrmann, E. J. Kelly, and R. Nitzberg: *A CFAR Adaptive Matched Filter Detector*, IEEE Transactions on Aerospace and Electronic Systems, vol. 28, no. 1, pp. 208-216, January 1992.
- [12] F. E. Nathanson: *Radar Design Principles, Second Edition*, McGraw-Hill, Inc., 1991.
- [13] J. V. Di Franco and W. L. Rubin: *Radar Detection*, Dedham, MA: Artech House, 1980.
- [14] L. Nicolaescu and T. Oroian. *Radar Cross Section*, 5-th International Conference on Telecommunications in Modern Satellite, Cable and Broadcasting Service 2001, TELSIS 2001, vol. 1, pp. 65-68, 2001.
- [15] C. E. Muehe, L. Cartledge, W. H. Drury, E. M. Hofstetter, M. Labitt, P. B. McCorison, V. J. Sferrino: *New Techniques Applied to Air-traffic Control Radars*, Proceedings of the IEEE, vol. 62, no. 6, pp. 716-723, June 1974.
- [16] P. E. Lawrance, A. P. Szabo: *Clutter Simulation in Maritime Environments*, Proceedings of the 2003 International Radar Conference, pp. 619-624, September 2003.
- [17] D. C. Scheleher: *Periscope Detection Radar*, Record of the 1995 IEEE Radar Conference, pp. 704-707, May 1995.
- [18] E. Conte, M. Lops: *Clutter-map CFAR Detection for Range-spread Targets in Non-Gaussian Clutter. Part I: System Design*, IEEE Transactions on Aerospace and Electronic Systems, vol. 33, no. 2, pp. 432-443, April 1997.
- [19] L. V. Blake. *Radar range-Performance Analysis*, D. C. Heath and Company, Lexington, MA, 1980.
- [20] W. Rihaczek: *Principles of High-Resolution Radar*, New York: McGraw-Hill Book Company, 1969.

- 
- [21] D. C. Lush: *Airborne Radar Analysis using the Ambiguity Function*, Record of the 1990 IEEE International Radar Conference, pp. 600-605, 1990.
- [22] P. M. Woodward: *Probability and Information Theory, with Application Radar*, Artech House, Norwood, MA, 1980.
- [23] D. C. Lush and D. A. Hudson: *Ambiguity Function Analysis of Wideband Radars*, Proceedings of the 1991 IEEE National Radar Conference, pp. 16-20, 1991.
- [24] W. L. Melvin: *A STAP Overview*, IEEE Magazine on Aerospace and Electronic Systems, vol. 19, no. 2, pp. 19-35, Jan. 2004.
- [25] I. S. Reed, J. D. Mallett and L.E. Brennan: *Rapid Convergence Rate in Adaptive Arrays*, IEEE Transactions on Aerospace and Electronic Systems, AES-10, no. 6, November 1974.
- [26] S. Z. Kalson: *An Adaptive Array Detector with Mismatched Signal Rejection*, IEEE Transactions on Aerospace and Electronic Systems, vol. 28, no. 1, pp. 195-207, January 1992.
- [27] A. Steinhardt: *Foundations of Adaptive Detection*, Proceedings of the Adaptive Sensor Array Processing Workshop, Lincoln Laboratories, Massachusetts Institute of Technology, pp. 807-831, March 1993.
- [28] L. E. Brennan, J. D. Mallett and I. S. Reed: *Adaptive Arrays in Airborne MTI Radar*, IEEE Transactions on Antennas and Propagation, vol. AEP-24, pp. 607-615, September 1976.
- [29] R. A. Monzingo and T. W. Miller: *Introduction to Adaptive Arrays*, New York, NY: John Wiley and Sons, 1980.
- [30] R. T. Compton, Jr.: *Adaptive Antennas-Concepts and Performance*, Englewood Cliffs, NJ: Prentice Hall, 1980.
- [31] L. W. Brooks and I. S. Reed: *Equivalence of the Likelihood Ratio Processor, the Maximum Signal-to-Noise Filter, and the Wiener Filter*, IEEE Transactions on Aerospace and Electronic Systems, pp. 690-692, September 1972.

- 
- [32] E. J. Kelly: *Performance of an Adaptive Detection Algorithm: Rejection of Unwanted Signals*, IEEE Transactions on Aerospace and Electronic Systems, AES-25, no. 2, pp. 122-133, March 1989.
- [33] D. M. Boroson: *Sample Size Considerations in Adaptive Arrays*, IEEE Transactions on Aerospace and Electronic Systems, AES-16, no. 4, pp. 446-451, July 1980.
- [34] R. C. Heimiller, J. E. Belyea, P. G. Thomlinson: *Distributed Array Radar*, IEEE Transactions on Aerospace and Electronic Systems, AES-19, pp. 831-839, 1983.
- [35] M. I. Skolnik: *An Analysis of Bistatic Radar*, IRE Transactions on Aerospace and Navigational Electronics, pp. 19-27, March 1961.
- [36] M. I. Skolnik: *Introduction to Radar Systems*, McGraw-Hill, New York, 1980.
- [37] R. A. Dana, and D. L. Knepp: *The Impact of Strong Scintillation on Space Based Radar Design, I: Coherent Detection*, IEEE Transactions on Aerospace and Electronic Systems, AES-19, no. 4, July 1983.
- [38] V. P. Pyati: *The Role of Circular Polarization in Bistatic Radars for Mitigation of Interference Due to Rain*, IEEE Transactions on Antennas and Propagation, AP-32, no. 3, pp. 295-296, March 1984.
- [39] R. J. Lefevre: *Bistatic Radar: New Application for an Old Technique*, WESCON Conference Record, pp. 1-20, San Francisco, 1979.
- [40] James and James: *Mathematics Dictionary*, Van Nostrand, New York, 1949.
- [41] J. G. Schoenenberger, and J. R. Forrest: *Principles of Independent Receivers for Use with Cooperative Radar Transmitters*, The Radio and Electronic Engineer, vol. 52, no. 2, pp. 93-101, February 1982.
- [42] E. F. Ewing, and L. W. Dicken: *Some Applications of Bistatic and Multi-Bistatic Radars*, Proceedings of the International Radar Conference, pp. 222-231, 1978.
- [43] A. Farina: *Tracking Function in Bistatic and Multistatic Radar Systems*, IEE Proceedings, vol. 133, no. 7, Pt. F., pp. 630-637, December 1986.

- 
- [44] R. B. Patton: *Orbit Determination from Single Pass Doppler Observations*, IRE Transactions Military Electronics, pp. 336-344, April-July 1960.
- [45] I. Stein: *Bistatic Radar Applications in Passive Systems*, Journal of Electronic Defense, vol. 13, no. 3, pp. 55-61, March 1990.
- [46] C. H. Dawson: *Inactive Doppler Acquisition Systems*, Transactions AIEE, vol. 81, pp. 568-571, January 1963.
- [47] I. J. Gupta and A. A. Ksienski: *Effect of Mutual Coupling on the Performance of Adaptive Arrays*, IEEE Transactions on Antennas and Propagation, vol. AP-31, no. 5, pp. 785-791, September 1983.
- [48] A. Farina, G. Capraro, H. Griffiths, and M. Wicks: *Knowledge-Based Radar Signal & Data Processing*, Research and Technology Organisation (RTO) Lecture Series 233, NATO, Rome, Italy, November 2003.
- [49] C. Yeh, Y. J. Hong, and D. R. Ucci: *The Effect of Finite Distance Source on an Applebaum Array*, IEEE Transactions on Antennas and Propagation, vol. AP-33, no. 9, September 1985.
- [50] B. Friedlander and A. J. Weiss: *Direction Finding in the Presence of Mutual Coupling*, IEEE Transactions on Antennas and Propagation, vol. 3, no. 3, pp. 273-284, March 1991.
- [51] A. J. Weiss and B. Friedlander: *Mutual Coupling Effects on Phase-Only Direction Finding*, IEEE Transactions on Antennas and Propagation, vol. 40, no. 5, pp. 535-541, May 1992.
- [52] T. Svantesson: *Direction Finding in the Presence of Mutual Coupling*, Thesis for the degree of Licentiate of Engineering, Tech. Rep. no. 307L, Chalmers University of Technology, Sweden, 1999
- [53] B. D. Steinberg: *Principles of Aperture and Array System Design*, New York, Wiley, 1976.
- [54] R. S. Elliott: *Antennas Theory and Design*, Englewood Cliffs, NJ: Prentice Hall, 1981.
- [55] R. C. Hansen: *Microwave Scanning Antennas*, New York: Academic, 1966.

- 
- [56] R. S. Adve, R. A. Schneible, G. Genello, and P. Antonik: *Waveform-Space-Time Adaptive Processing for Distributed Aperture Radars*, Proceedings of the IEEE International Radar Conference 2005, pp. , Washington DC, USA, May 2005.
- [57] D. Madurasinghe and L. Teng: *Adaptive Array Processing - Near Field Experiment*, Defence Science and Technology Organization, Australia, DSTO-TR-0361, 1996.
- [58] E. M. Friel and K. M. Pasala: *Effects of Mutual Coupling on the Performance of STAP Antenna Arrays*, IEEE Transactions on Aerospace and Electronic Systems, vol. 36, no. 2, April 2000.
- [59] K. Kim, T. K. Sarkar, and M. S. Palma: *Adaptive Processing Using a Single Snapshot for a Nonuniformly Spaced Array in the Presence of Mutual Coupling and Near-Field Scatters*, IEEE Transactions on Antennas and Propagation, vol. 50, no. 5, May 2002.
- [60] H. L. Van Trees: *Optimum Array Processing, Part IV of Detection, Estimation, and Modulation Theory*, Wiley-Interscience, 2002, John Wiley & Sons, Inc., New York.
- [61] T. W. Anderson: *An Introduction to Multivariate Statistical Analysis*, Second Edition, John Wiley & Sons, 1984.
- [62] B. Himed and W. L. Melvin: *Analyzing Space-Time Adaptive Processors Using Measured Data*, Proc. of the Thirty-First Asilomar Conference on Signals, Systems & Computers, pp. 930-935, 1998.
- [63] R. Nitzberg: *Application of Maximum Likelihood Estimation of Persymmetric Covariance Matrices to Adaptive Processing*, IEEE Trans. on Aerospace and Electronic Systems, Vol. 16, No. 1, pp. 124-127, January 1980.
- [64] L. Cai and H. Wang: *A Persymmetric Multiband GLR Algorithm*, IEEE Trans. on Aerospace and Electronic Systems, Vol. 28, No. 3, pp. 806-816, July 1992.
- [65] S. Kraut and L. L. Scharf: *The CFAR Adaptive Subspace is a Scale-Invariant GLRT*, IEEE Trans. on Signal Processing, Vol. 47, No. 9, pp. 2538-2541, September 1999.

- 
- [66] E. Conte, A. De Maio, and G. Ricci: *GLRT-Based Adaptive Detection Algorithms for Range-Spread Targets*, IEEE Trans. on Signal Processing, Vol. 49, No. 7, pp. 1336 -1348, July 2001.
- [67] E. Conte, M. Lops, and G. Ricci: *Asymptotically Optimum Radar Detection in Compound-Gaussian Clutter*, IEEE Trans. on Aerospace and Electronic Systems, Vol. 31, No. 2, pp. 617-625, April 1995.
- [68] H. L. Van Trees: *Detection, Estimation and Modulation Theory*, Pt. 1, John Wiley & Sons, 1968.
- [69] E. J. Kelly and K. Forsythe: *Adaptive Detection and Parameter Estimation for Multidimensional Signal Models*, Tech. Report No. 848, Lincoln Laboratories, April 19, 1989.
- [70] A. De Maio, L. Landi, and A. Farina: *Adaptive Radar Detection in the Presence of Mutual Coupling and Near-Field Effects*, to be printed on IET Radar, Sonar and Navigation.
- [71] M. Casillo, A. De Maio, S. Iommelli, L. Landi: *A Persymmetric GLRT for Adaptive Detection in Partially-Homogeneous Environment*, IEEE Signal Processing Letters, vol. 14, no. 12, pp. 1016-1019, December 2007.
- [72] L. Applebaum and R.S. Adve: *Adaptive Processing with frequency diverse distributed apertures*, Proceedings of the 2nd International Waveform Diversity and Design Conference, Hawaii, Jan. 2006.
- [73] R. S. Adve, R. A. Schneible, and R. McMillan: *Adaptive Space/Frequency Processing for Distributed Aperture Radars*, Proceedings of the 2003 IEEE Radar Conference, pp. 160 - 164, May 2003.
- [74] S. Sira, D. Morell, and A. Papandreu-Suppappola: *Waveform design and scheduling for agile sensors for target tracking*, Proceedings of the 2004 Asilomar Conference on Signals, Systems and Computers, vol. 1, November 2004.
- [75] B. Himed, J. H. Michels, and Y. Zhang: *Bistatic STAP performance analysis in radar applications*, Proceedings of the 2001 IEEE Radar Conference, 2001. Atlanta, GA.
- [76] P. K. Sanyal, R. D. Brown. M. O. Little, R. A. Schneible, and M. C. Wicks: *Space-time adaptive processing bistatic airborne radar*, Proceedings of the 1999 IEEE Radar Conference, 1999. Waltham, MA.

- 
- [77] W. L. Melvin, M. J. Callahan, and M. C. Wicks: '*Adaptive Clutter Cancellation in Bistatic Radar*, Conference Record of the Thirty-Four Asilomar Conference on Signals, Systems and Computers, 2000, vol. 2, pp. 1125-1130.
- [78] E. Lock and R. S. Adve: '*Varying fm rates in adaptive processing for distributed radar apertures*, Proceedings of the 3rd International Waveform Diversity and Design Conference, June 2007. Pisa, Italy
- [79] H. Wang, and L. Cai: '*On adaptive spatial-temporal processing for airborne surveillance radar systems*, IEEE Transactions on Aerospace and Electronic Systems, vol. 30, pp. 660-699, July 1994.
- [80] R. S. Adve, T. B. Hale, and M. C. Wicks: '*Practical joint domain localised adaptive processing in homogeneous and nonhomogeneous environments. Part I: Homogeneous environments*, IEE Proceedings on Radar, Sonar and Navigation, vol. 47, no. 2, April 2000.
- [81] M. C. Jackson: '*The Geometry of Bistatic Radar Systems*, IEE Proceedings, vol. 133, no. 7, pp. 604-612, December 1986.
- [82] D. E. N. Davies: '*Use of Bistatic Radar Techniques to Improve Resolution in the Vertical Plane*, IEE Electronics Letters, vol. 4, no. 9, pp. 170-171, May 1968.
- [83] H. Wang, and L. Cai: '*On adaptive implementation of optimum MTI in severely nonhomogenous environments*, Proceedings of the IEEE International Radar Conference, Arlington, VA, May 7-10, 1990, pp. 351-355.
- [84] H. Wang, and L. Cai: '*A localized adaptive MTD processor*, IEEE Transactions on Aerospace and Electronic Systems, Vol. 27, no. 3, May 1991, pp. 532-539.
- [85] L. Brennan, and I. Reed: '*Theory of Adaptive Radar*, IEEE Transactions on Aerospace and Electronic Systems, vol. AES-9, pp. 237-252, March 1973.
- [86] F. Harris: '*On the use of windows for harmonic analysis with the discrete Fourier Transform*, Proceedings IEEE, vol. 66, no. 1, pp. 51-83, 1978.
- [87] M. Greco, F. Gini, M. Diani: '*Robust CFAR detection of random signals in compound-Gaussian clutter plus thermal noise*, IEE Proceedings on Radar, Sonar and Navigation, vol. 148, no. 4, pp. 227-232, 2001.

- 
- [88] N. R. Goodman: *Statistical Analysis Based on a Certain Multivariate Complex Gaussian Distribution*, Annals of Mathematical Statistics, vol. 34, pp. 152-177, 1963.
- [89] L. Landi, and R. S. Adve: *Time-Orthogonal-Waveform-Space-Time Adaptive Processing for Distributed Aperture Radars*, Proceedings of the 2007 IEEE International Waveform Diversity and Design Conference, pp. 13-17, 2007.
- [90] L. Landi, and R. S. Adve: *Range Doppler Correlation for Time-Orthogonal Distributed Aperture Radars*, Proceedings of the 2007 IET International Radar Conference, 2007.

